Study of τ Final States in Gauge Mediated Supersymmetry Breaking Models at ATLAS

Diplomarbeit
vorgelegt von Dörthe Ludwig
Oktober 2008

Gutachter
Prof. Dr. Johannes Haller
Prof. Dr. Peter Schleper

Institut für Experimentalphysik
MIN - Fakultät
Universität Hamburg

Zusammenfassung

In dieser Diplomarbeit werden Supersymmetrie Modelle, in denen die Brechung durch eine Eichwechselwirkung (GMSB) übertragen wird, mit dem ATLAS Experiment untersucht. Die studierten Endzustände beinhalten mehrere τ Leptonen. Die schnittbasierte Selektion wird mit einem typischen GMSB Signal optimiert, um eine maximale Unterdrückung des Standard Modell Untergrunds gegenüber dem Signal zu erreichen. Zum ersten Mal wird eine Bestimmung des Entdeckungspotentials mit τ Leptonen im GMSB Parameterraum durchgeführt. Zusätzlich wird die Verteilung der invarianten Masse zweier τ Leptonen benutzt, um Rückschlüsse auf die Massen supersymmetrischer Teilchen zu ziehen.

Abstract

In this thesis Supersymmetry models with Gauge Mediated Supersymmetry Breaking containing τ leptons in the final states are investigated using the ATLAS detector. A cut based selection is optimized with a typical GMSB signal to maximize the reduction of the Standard Model background with respect to the signal. For the first time an estimation of the discovery potential in the GMSB parameter space using τ leptons is done. In addition, the invariant mass distribution of two τ leptons is used to study the masses of the supersymmetric particles.

Contents

List of Figures

List of Tables

Chapter 1

Introduction

The Large Hadron Collider (LHC) is a proton-proton-collider located at CERN[1]. The main focus lies on the study of elementary particles and their interactions. Of high interest is the measurement of properties of the Standard Model (SM) and their comparison with predictions from theory. The primary goal of studies at the LHC is the discovery of the Higgs boson, the last missing SM particle. Since the shortcomings of the SM, such as the hierarchy problem and the unification of the coupling constants, suggest that the SM is a low energy limit of a more fundamental theory the search for physics beyond the SM is of similar importance. Among the many extensions proposed, describing physics beyond the SM, Supersymmetry (SUSY) is considered a key candidate, as it is able to solve several of the shortcomings of the SM in a very elegant way.

In an exact symmetry, supersymmetric particles have the same mass as their SM partners. Since supersymmetric particle have not yet been observed, SUSY is assumed to be broken. In this thesis for the first time studies of the discovery potential of Gauge Mediated Supersymmetry Breaking (GMSB) models with the ATLAS detector, one of the two multi-purpose detectors at the LHC, are presented. The analysis focuses on multi τ final states occuring in a large fraction of the parameter space. Since several SUSY models are conceivable the determination of characteristic parameters such as the masses of the SUSY particles is a major task. As an example the invariant mass of two τ leptons is used to extract information on the underlying SUSY model.

This thesis is organized as follows. After a short introduction to the main concepts of the SM and its shortcomings, it is described how SUSY is able to solve these problems. In addition Gauge Mediated Supersymmetry Breaking models are briefly explained in chapter 2. Chapter 3 and chapter 4 describe the ATLAS detector and its main components as well as the generation and simulation of Monte Carlo events used for this study. Chapter 5 is devoted to the reconstruction of τ leptons and missing transverse energy, their expected performance and an efficiency study of τ reconstruction in GMSB models. A short comparison be-

---

[1] European Organization for Nuclear Research

tween full and fast simulation is presented. The selection of events is presented in chapter 6. Additionally, the study of the discovery potential in the GMSB parameter space is discussed. The SUSY mass measurement from the invariant mass distribution of two τ leptons is described in chapter 7.

Chapter 2

The Standard Model and Beyond

This chapter gives an overview of the Standard Model (SM) describing the elementary particles and their fundamental interactions. By looking at the shortcomings of the SM the need for an extension of the SM is motivated. The most studied extension of the SM is the so-called *Supersymmetry* (SUSY). The Minimal Supersymmetric Standard Model (MSSM) and finally a particular kind of supersymmetric models, those with Gauge Mediated Supersymmetry Breaking (GMSB), are introduced.

2.1 The Standard Model

The Standard Model [1] describes the elementary particles and their fundamental interactions. It includes three fundamental forces: the strong, the weak and the electromagnetic interaction. Gravitation is not included in the SM. The three SM interactions can be described by a local symmetry group

$$\mathrm{SU(3)_C} \times \mathrm{SU(2)_L} \times \mathrm{U(1)_Y}, \tag{2.1}$$

where C is the color charge of the strong interaction, L stands for the left-handedness of the weak current and Y denotes the weak hypercharge, which establishes a correlation between the electric charge Q and the third component of the weak isospin T_3

$$Q = T_3 + \frac{Y}{2}. \tag{2.2}$$

Every interaction is mediated by gauge bosons, eight massless gluons for the strong interaction [2], the photon for the electromagnetic and the W and Z bosons for the weak interaction (cf. Table 2.1). The gluons and the photon are massless whereas the W and Z boson are very heavy limiting the range of the weak interaction to a few 10^{-3} fm.

The couplings of the gauge bosons to the SM fermions depends on the charge the particle possesses. For every interaction a different charge is defined. For the strong interaction the charge is the color. For symmetry reasons three colors are

	mass	el. charge	interaction
g	0	0	strong
γ	0	0	electromagnetic
$W^{\pm}$, Z^0	80.4 GeV, 91.2 GeV	± 1, 0	weak

Table 2.1: The gauge bosons which mediate the forces described by the SM.

defined resulting in eight colored gluons which couple to the six quarks and one color neutral singlet which cannot mediate a force. Since the gluons carry color they will also couple to themselves.

The fields of the $\mathrm{W}^{\pm}$ bosons are a mixing

$$W^{(\pm)\mu} = \frac{1}{\sqrt{2}} \left(W_1^\mu \pm i W_2^\mu \right) \tag{2.3}$$

of two fields $W_{1,2}^\mu$ with a weak isospin $\mathrm{T} = 1$ and $\mathrm{T}_3 = \pm 1$ resulting from the SU(2) gauge invariance. The corresponding third field of the triplet W_3^μ with a weak isospin of $\mathrm{T} = 1$ and $\mathrm{T}_3 = 0$ mixes with the weak isospin singlet B^μ ($\mathrm{T} = \mathrm{T}_3 = 0$) and determines the field Z^μ of the Z^0 boson and the electromagnetic field A^μ of the photon

$$\begin{pmatrix} A^\mu \\ Z^\mu \end{pmatrix} = \begin{pmatrix} \cos\theta_W & \sin\theta_W \\ -\sin\theta_W & \cos\theta_W \end{pmatrix} \begin{pmatrix} B^\mu \\ W_3^\mu \end{pmatrix}, \tag{2.4}$$

where θ_W is the weak mixing angle that links the masses of the weak gauge bosons. It is defined through the couplings g' and g of $\mathrm{SU(2)_L} \times \mathrm{U(1)_Y}$ as

$$\cos\theta_W = \frac{g}{\sqrt{g^2 + g'^2}}, \qquad \sin\theta_W = \frac{g'}{\sqrt{g^2 + g'^2}}, \qquad M_\mathrm{Z} = \frac{M_\mathrm{W}}{\cos\theta_W}. \tag{2.5}$$

The weak isospin emblematizes the charge of the weak interaction. The fields W^μ of SU(2), therefore the gauge bosons $\mathrm{W}^{\pm}$, couple to the left-handed states of all particles. As the field B^μ couples to left- as well as right-handed fermions the photon and the Z^0 boson do as well. In general, the photon couples to all particles that are electrically charged. The uncharged neutrinos are only affected by the weak interaction.

Table 2.2 shows the fermions of the SM consisting of the six quarks and six leptons. The listed quark states are the mass eigenstates which are not identical with those of the weak interaction. Three of the weak eigenstates are a mixing of the strong ones. By convention the up type quarks do not mix and the down type quarks do as follows:

$$\begin{pmatrix} \mathrm{d}' \\ \mathrm{s}' \\ \mathrm{b}' \end{pmatrix} = \begin{pmatrix} V_\mathrm{ud} & V_\mathrm{us} & V_\mathrm{ub} \\ V_\mathrm{cd} & V_\mathrm{cs} & V_\mathrm{cb} \\ V_\mathrm{td} & V_\mathrm{ts} & V_\mathrm{tb} \end{pmatrix} \begin{pmatrix} \mathrm{d} \\ \mathrm{s} \\ \mathrm{b} \end{pmatrix} \tag{2.6}$$

			charge	T	T_3	strong	el.-magn.	weak
u	c	t	$2/3$	$1/2$	$1/2$	✓	✓	✓
d	s	b	$-1/3$	$1/2$	$-1/2$	✓	✓	✓
ν_e	ν_μ	ν_τ	0	$1/2$	$1/2$			✓
e^-	μ^-	τ^-	-1	$1/2$	$-1/2$		✓	✓

Table 2.2: The left-handed mass eigenstates of the six quarks and the left-handed leptons of the SM and three of their quantum numbers. The right-handed states have the same charge but do not have a weak isospin $T = T_3 = 0$. The neutrinos are only left-handed. The interactions in which the particles participate are also listed.

The matrix is the so-called *Cabibbo-Kobayashi-Maskawa-Matrix* (CKM-Matrix) [3, 4]. The diagonal elements are highly dominant. The other elements are considerably smaller resulting in a strongly suppressed mixing of the first and third quark family. The CKM-Matrix is unitary and determined by four parameters, three mixing angles and one CP-violating phase. In addition, the quarks occur in left- and right-handed states arranged in isospin doublets and singlets respectively.

The strong interaction affects only quarks and gluons. Due to the self-coupling of the gluons the strong field behaves differently than the electromagnetic field. An electromagnetic field diminishes with rising distance. The field between a quark and an antiquark can be imagined tube like and reinforces with distance at this scale. This phenomenon leads to the so-called *confinement* of the quarks which does not allow the quarks to occur in free colored states but only in color neutral quark compositions, called *hadrons*. Those can be either a quark-antiquark-pair forming mesons or three quarks building baryons, e.g. the proton.

Table 2.2 also shows the leptons [5] of the SM and some of their quantum numbers. In the SM the neutrinos are massless and therefore they only have a left-handed state. However the observation of neutrino oscillation has shown that the weak eigenstates are a mixing of the mass eigenstates which is similar to the quark mixing but involves the Maki-Nakagawa-Sakata-Matrix [6, 7].

The mathematical formulation of the symmetry groups mentioned in Eq. (2.1) is based on the gauge principle ensuring the invariance of the Dirac equation under a local phase transformation. The Dirac equation is the wave equation for leptons and quarks

$$(i\gamma^\mu \partial_\mu - m)\psi(x) = 0. \tag{2.7}$$

The invariance of this equation is only guaranteed with the presence of a field coupling to charged particles. The quanta of this field have to be massless gauge bosons. An exact symmetry does not allow mass terms in the Langrangian because they are not invariant under a gauge transformation. Since the gauge bosons of the weak interaction are not massless this symmetry is exact but broken. This symmetry breaking also gives mass to the fermions of the SM. To parametrize this symmetry breaking a doublet of scalar complex fields is introduced, the so-called

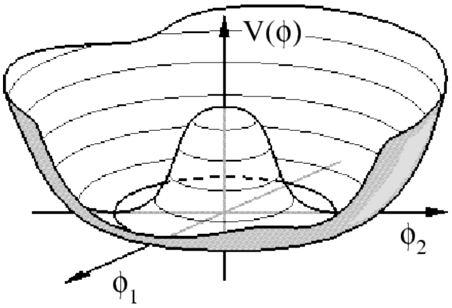

Figure 2.1: The Higgs potential.

Higgs field [8]:

$$\phi = \begin{pmatrix} \phi^{+} \\ \phi^{0} \end{pmatrix}, \tag{2.8}$$

where '+' and '0' indicate electric charge. Its potential is

$$V(\phi) = \mu^2 \left|\phi\right|^2 + \lambda \left|\phi\right|^4 . \tag{2.9}$$

If $\mu^2 < 0$ and $\lambda > 0$ this leads to a non zero vacuum expectation value. The shape of the potential is shown in Fig. 2.1. As the field is described by a complex doublet it possesses four degrees of freedom. Three yield the mass of the weak gauge bosons. Since the fourth degree of freedom is not absorbed by the massless photon it results in a neutral so-called *Higgs boson* whose couplings to the fermions are proportional to their masses.

The Higgs boson is the only particle of the SM which has not yet been observed. However, indirect searches of the LEP experiments achieved a mass constraint of $\mathrm{M_H} \geq 114\,\mathrm{GeV}$ [10] (Fig. 2.2).

2.2 The Shortcomings of the Standard Model

The SM describes the known particle spectrum and their interactions. It has predicted some of the elementary particles before they were observed and it has made very precise predictions for branching ratios which could be confirmed. Nonetheless the SM raises some problems to which it cannot provide any answers. This section points out some of these issues and states briefly how SUSY might be able to answer these questions.

It is dissatisfying that gravitation is not included in the SM. In the energy range described by the SM the gravitational strength is so small that it can be ignored. However if one goes up to the Planck Scale at approximately 10^{19} GeV where gravitational effects can no longer be neglected, the SM fails to make any predictions. The SM might therefore be a low energy limit to a more fundamental theory. This theory could be SUSY because defining SUSY as a local symmetry includes gravitation automatically.

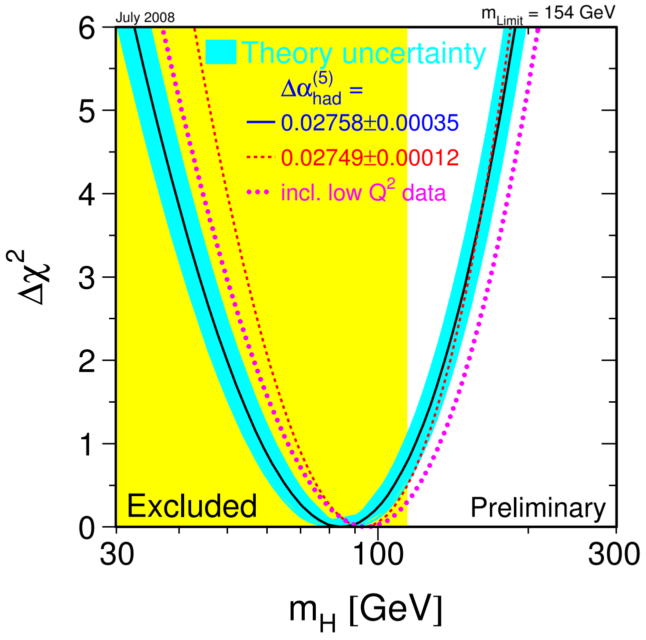

Figure 2.2: The SM Higgs is favoured to have a mass of 84^{+34}_{-26} GeV at 68% confidence level. The yellow region could be excluded by the LEP collaborations through direct Higgs searches [9].

From cosmological observations we know that the known matter described by the SM is only around 4% of the universe [11]. Around 73% is assumed to be *Dark Energy* about which very little is known. The rest (23%) of our universe is supposed to consist of *Dark Matter*. Dark matter is not charged and only weakly interacting. Only through gravitational effects the amount could be approximated. Up to now it is unknown of what kind of particles dark matter could consist because there is no candidate within the known particle spectrum. The only uncharged and massive particles the SM offers are neutrinos. But their masses are too small in order to be reasonable candidates.

In addition, SUSY could provide the unification of the coupling constants at the GUT[1] scale at $\approx 10^{16}$ GeV. In GUT-like theories it is assumed that in the Big Bang all the forces have been unified and therefore their couplings were identical. If the coupling constants are extrapolated from the electroweak scale to the GUT scale they should meet at some point. However, in the SM this is not the case. A supersymmetric model leads to the unification of the coupling constants illustrated in Fig. 2.3.

In the SM the Higgs mass underlies corrections from loops of e.g. SM fermions (cf. Fig. 2.4) such that the Higgs mass is the sum of the bare Higgs mass and

---

[1] Grand Unification Theory

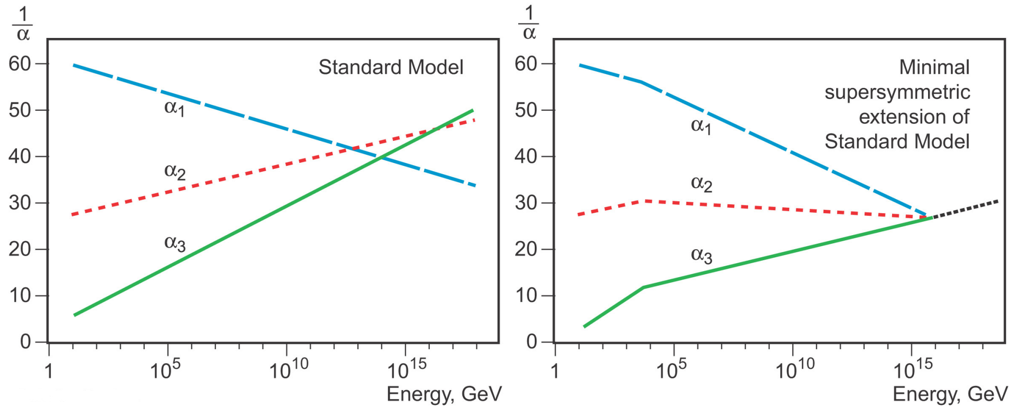

Figure 2.3: The running of the coupling constants (α_1 - electromagnetic, α_2 - weak, α_3 - strong) in the SM and in the Minimal Supersymmetric Standard Model [12].

Figure 2.4: The Higgs mass is subject to corrections from fermions loops (left). In supersymmetric models the same number of boson loops is added (right) [13].

those corrections

$$m_H^2 = m_{H\text{bare}}^2 + \Delta m_H^2, \tag{2.10}$$

which can be written for a fermion of mass m_f as

$$\Delta m_H^2 = -\frac{|\lambda_f|^2}{8\pi^2}\Lambda_{UV}^2, \tag{2.11}$$

where the coupling of the Higgs field to the fermion is $-\lambda_f H\bar{f}f$ in the Langrangian. Λ_{UV}^2 indicates a cut-off which can be interpreted as the scale where new physics enters. The Higgs mass is quadratically divergent whereas all SM particle masses diverge only logarithmically. In order to yield a Higgs mass of $\mathscr{O}(100\,\text{GeV})$, predicted by the SM, the bare Higgs mass has to be of the same order of magnitude as the corrections. These two values have to be very fine-tuned such that their values have to be identical in many decimal places. This is known as the *fine-tuning* or *hierarchy* problem.

2.3 Supersymmetry

As indicated in Sect. 2.2 SUSY [13] might be able to solve some of the shortcomings of the SM. SUSY introduces a whole new particle spectrum by establishing a symmetry between fermions and bosons. To every fermion there is a boson and vice versa (cf. Table 2.3). Those new particles have identical quantum numbers as their superpartners except for their spin which is decreased (increased for Higgs bosons) by half a unit. This is described by the following transformation

$$Q\,|\text{fermion}\rangle = |\text{boson}\rangle \qquad \text{and} \qquad Q\,|\text{boson}\rangle = |\text{fermion}\rangle\,, \tag{2.12}$$

where the operator Q is an anticommutating spinor. If a theory is invariant under this transformation, it is called supersymmetric. The irreducible representation of the SUSY algebra are so-called *supermultiplets*. They contain both fermion and boson states, explicitly SM particles and their superpartners in such a way that the number of degrees of freedom for fermions is the same as for bosons.

The superpartners of the leptons are called sleptons which is indicated by a tilde: $\widetilde{\ell}$. Squarks $\widetilde{q}$ constitute the superpartners of the quarks. The name of the partners of the gauge bosons, the gauginos, are formed by expanding their name with -ino.

Fermions have different superpartners for their left- and right-handed states. These left- and right-handed supersymmetric states do not refer to their own helicity but to that of their SM partner. Those states also have the same mass and identical quantum numbers as their partner including charge and couplings.

In contrast to the SM instead of one Higgs doublet in SUSY two doublets are needed. One of the doublets can only give mass to up type quarks because of the Yukawa coupling it possesses, and the other doublet gives mass to the down type quarks and to the charged leptons. These two doublets have eight degrees of freedom three of which are absorbed by the gauge bosons of the weak interaction just as in the SM resulting in five physical higgs bosons. The fraction of the non-zero vacuum expectation values is a free parameter of the theory

$$\tan\beta = \frac{v_u}{v_d}. \tag{2.13}$$

The neutral superpartners of the gauge boson fields, Bino $\widetilde{\mathrm{B}}$ and Wino $\widetilde{\mathrm{W}}^0$, mix with the neutral Higgsinos $\widetilde{\mathrm{H}}^0$ to form the four mass eigenstates of the so-called *neutralinos* $\widetilde{\chi}^0$. The charged gauginos and Higgsinos mix forming the two mass eigenstates of the *charginos* $\widetilde{\chi}^{\pm}$ which have either positive or negative charge. The SM particles and their superpartners are summarized in Table 2.3.

The introduction of new particles leads to additional corrections to the Higgs mass. For every SM fermion there is a correction from a supersymmetric boson and vice versa. Those corrections would cancel each other because the loop diagrams have opposite signs and the fine-tuning problem would be solved.

Since to this date no supersymmetric particles were found it is assumed that SUSY is not an exact symmetry but broken which causes the masses of the superpartners to be higher than those of their SM partners. The scale at which the breaking occurs must be sufficiently low in order to solve the hierarchy problem.

Spin: 0	1/2	1
$\widetilde{\ell}^{\pm}$, $\widetilde{\nu}$ $\widetilde{q}$	$\ell^{\pm}$, ν q	
	$\widetilde{\mathrm{g}}$	g
h^0, A^0, H^0	$\widetilde{\mathrm{h}}^0$, $\widetilde{\mathrm{H}}^0$ $\widetilde{\gamma}$, $\widetilde{\mathrm{Z}}$ Mix to form neutralinos $\widetilde{\chi}^0$	γ, Z
$\mathrm{H}^{\pm}$	$\widetilde{\mathrm{H}}^{\pm}$ $\widetilde{\mathrm{W}}^{\pm}$ Mix to form charginos $\widetilde{\chi}^{\pm}$	$\mathrm{W}^{\pm}$

Table 2.3: SUSY establishes a symmetry between fermions and bosons. The extended particle spectrum offers a boson to every known fermion and vice versa. Additionally a two Higgs doublet model is necessary leading to five physical Higgs bosons.

If it is at too high energies the loop corrections to the Higgs will not cancel each other.

In the SM the baryon number B and the lepton number L are conserved since no possible renormalizable Langrangian terms can introduce such violation. In contrast for the superpotential in SUSY an additional multiplicative quantum number is introduced to ensure the conservation of B and L, the so-called *R-parity*

$$\mathrm{R} = (-1)^{2\mathrm{S}+3(\mathrm{B}-\mathrm{L})}, \tag{2.14}$$

where S is the spin. With this definition SM (SUSY) particles have R-Parity $\mathrm{R} = 1$ ($\mathrm{R} = -1$). In the MSSM R-parity is supposed to be exactly conserved. This fact has some significant consequences:

- At particle colliders SUSY particles can only be produced in pairs.
- Every supersymmetric particle will eventually decay into the lightest supersymmetric particle (LSP) or an odd number of LSPs.
- The LSP is stable. If the LSP is uncharged, has no color, and is only weakly interacting it could be considered as a dark matter candidate. The LSP will behave similar to neutrinos inside the detetor which brings forth a signature of a noteworthy amount of missing transverse energy.

In this thesis R-parity conservation is assumed. The phenomenolgy of R-parity violating models is quite different because the LSP decays into SM particles. These models are not discussed in detail in this thesis.

In the general MSSM 105 free parameters are added to the 19 of the SM. Reduction to less parameters is possible by assuming a specific breaking mechanism. The most important ones are:

mSUGRA (minimal SUperGRAvity): It is assumed that SUSY is a local symmetry. The breaking is communicated through gravitation. At the GUT

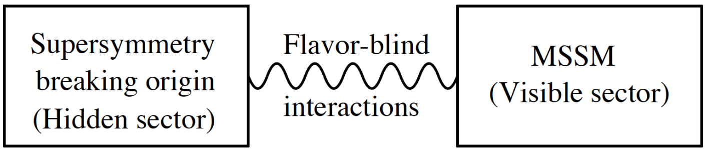

Figure 2.5: The communication of the SUSY breaking from the hidden to the visible sector [13].

scale all scalar particles are assumed to have the same mass m_0.For all gauginos and higgsinos this mass is $m_{\frac{1}{2}}$. Other free parameters are the Higgs-sfermion-sfermion-coupling A, $\tan\beta$ and the sign of the Higgsino mass term μ.

GMSB: The minimal model will be discussed in detail in the next section.

AMSB (Anomaly Mediated Supersymmetry Breaking): The breaking is transmitted through an anomaly in supergravity. The lightest neutralino, which is the LSP, as well as the lightest chargino are almost pure Winos leading to almost degenerate masses. Therefore the chargino possesses a long lifetime which enables its detection inside the detector.

These models have very few free parameters determining the masses of all particles and their mixing. All the branching ratios are calculable and the resulting phenomenoloy is fixed.

2.3.1 Gauge Mediated Supersymmetry Breaking

The SUSY breaking parameters arise from spontaneous SUSY breaking in a hidden sector. The breaking is communicated to the MSSM at a scale $M \gg M_Z$. Assumptions on exact flavor and CP conservation reduce the number of free paramters. The parameters at this scale, at which the breaking occurs, are related to those at the weak scale by the renormalization group equations (RGE).

The free parameters in GMSB models are the following:

- $\Lambda = \frac{\mathrm{F_m}}{\mathrm{M_m}}$: The scale of the SUSY breaking. It adopts typically values of $10-100\,\mathrm{TeV}$. It sets the overall mass scale for all MSSM superpartners which depend linearly on Λ. $\mathrm{F_m}$ is the effective SUSY breaking order parameter.
- $\mathrm{M_m}$: The Messenger mass scale. $\mathrm{M_m}$ has to be larger than Λ in order to prevent color and charge breaking in the messenger sector.
- $\mathrm{N_5}$: The number of equivalent messenger fields. The gaugino masses depend linearly on $\mathrm{N_5}$ whereas the sfermion masses depend on $\sqrt{\mathrm{N_5}}$.
- $\tan\beta$: As mentioned in Eq. (2.13) $\tan\beta$ is the ratio of the two Higgs vacuum expectation values at the electroweak scale.

	Λ	$\mathrm{M_m}$	$\mathrm{N_5}$	$\tan\beta$	sgnμ	$\mathrm{C_{grav}}$
GMSB6	40 TeV	250 TeV	3	30	+1	1.0

Table 2.4: The parameters of the GMSB6 scenario.

- sgn$\mu = \pm 1$: As in mSUGRA one parameter is the sign of the Higgsino mass term appearing in the neutralino and chargino mass matrices. The actual value $|\mu|$ is determined by the Z mass from radiative electroweak symmetry breaking.

- $\mathrm{C_{grav}} = \frac{\mathrm{F}}{\mathrm{F_m}} \geq 1$: The ratio of the effective SUSY breaking order parameter $\mathrm{F_m}$ to the underlying SUSY breaking order parameter F which determines the coupling strength of the gravitino. $\mathrm{C_{grav}}$ determines the lifetime of the NLSP.

In GMSB models [14, 15] the breaking is communicated through a flavor-blind SM gauge interaction (Fig. 2.5) with so-called *messenger fields* at a scale $\mathrm{M_m}$ small compared to the Planck mass. These gauge interactions are proportional to the gauge couplings times Λ. At $\mathrm{M_m}$ the masses are the same for each generation preventing the occurence of flavor changing neutral currents. In the minimal model the messenger fields need to form complete representatives of SU(5) in order to preserve the mentioned unification of coupling constants in the MSSM. The squarks, sleptons and gauginos get their masses through a gauge interaction with these massive messengers. The actual masses depend on the concrete number of messenger fields $\mathrm{N_5}$.

The ATLAS collaboration settled on seven different benchmark points (Table A.1) each featuring a different phenomenology and thus offering different final states and signatures in the detector. This thesis will concentrate on the ATLAS benchmark point GMSB6 whose parameter values are listed in Table 2.4.

The parameters of the GMSB6 scenario yield the mass spectrum shown in Fig. 2.6 and listed in Table A.1. The right-handed slepton and squark states are of lower mass. For the third slepton and squark generation the left- and right-handed state mix. In GMSB models the LSP is always the very light gravitino $\widetilde{G}(\ll 1\,\mathrm{keV})$. The next-to-lightest supersymmetric particle (NLSP) depends on $\mathrm{N_5}$ and on $\tan\beta$. If $N_5 = 1$ the NLSP is either the lightest neutralino $\widetilde{\chi}_1^0$ which decays into a photon and a gravitino or for higher $\tan\beta$ values the $\widetilde{\tau}$. On the other hand for $N_5 \geq 2$ the NLSP is a slepton in a wide range of the parameter space. In Fig. 2.7 the NLSP is shown for $N_5 = 3$. It can be seen that if $\tan\beta$ is large the $\widetilde{\tau}_1$ is the only NLSP. For smaller values of $\tan\beta$ the mixingof the left- and right-handed states of the third family becomes very small and the $\widetilde{\tau}_1$ and the right-handed selectron (smuon) are almost mass degenerate rendering them so-called *Co-NLSPs*. The NLSP determines decisively the phenomenology of a GMSB model. In the GMSB6 scenario the NLSP is the $\widetilde{\tau}_1$ due to the large $\tan\beta$ value and $N_5 > 1$.

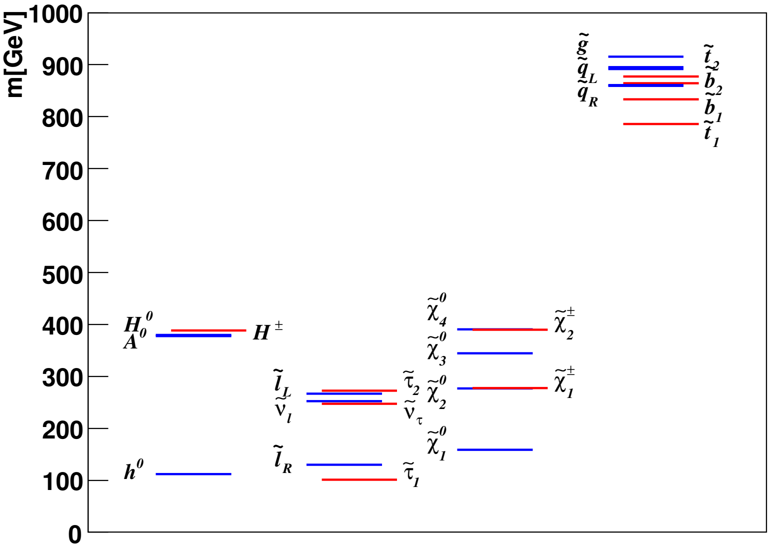

Figure 2.6: The mass spectrum for the ATLAS benchmark point GMSB6.

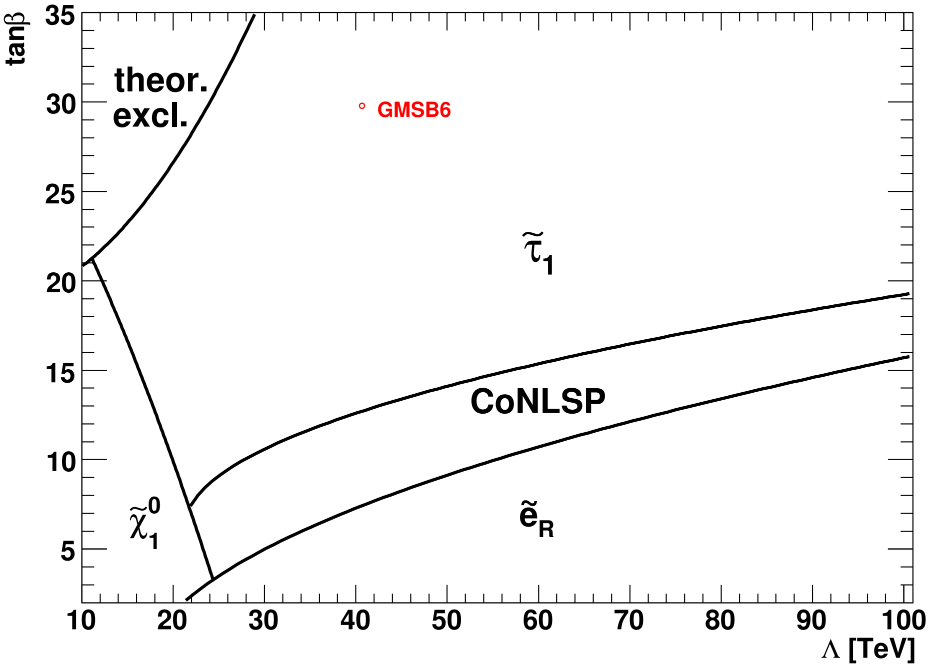

Figure 2.7: The nature of the NLSP in the Λ - $\tan\beta$ plane in GMSB. The ATLAS benchmark point GMSB6 is indicated in the region where the $\tilde{\tau}$ is the NLSP.

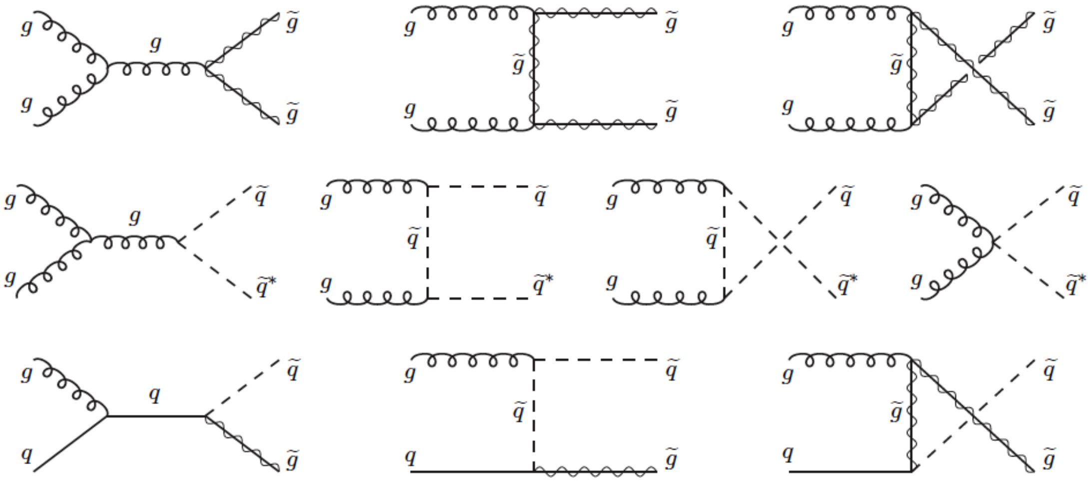

Figure 2.8: Feynman graphs of gluino and squark production at the LHC [13].

Since the gravitino mass is negligible the coupling to the SUSY particles is very small except for the $\widetilde{\tau}$ which decays exclusively into the gravitino. This leads very often to final states with two τ leptons at the end of one SUSY decay chain. The decays of the lightest neutralino and the right-handed slepton are dominant. The decay of a chargino is not as frequent and produces only one τ and a ν_τ.

$$\widetilde{\chi}^0{}_{1,2} \rightarrow \widetilde{\tau}_1\, \tau \rightarrow \tau\, \tau\, \tilde{G} \qquad 43\%, 9\% \qquad (2.15)$$

$$\widetilde{\ell}_R \rightarrow \ell\, \widetilde{\tau}_1\, \tau \rightarrow \ell\, \tau\, \tau\, \tilde{G} \qquad 28\% \qquad (2.16)$$

$$\widetilde{\chi}^\pm_1 \rightarrow \widetilde{\tau}_1\, \nu_\tau \rightarrow \tau\, \nu_\tau\, \tilde{G} \qquad 13\% \qquad (2.17)$$

The LHC will provide proton-proton collisions in which gluon-gluon-fusion is expected to be the dominant hard proton interaction leading to the production of SUSY particles shown in Fig. 2.8. The produced SUSY particles will be squarks and gluinos decaying through long decay chains into the gravitino thereby producing high-energetic jets because of the high mass of squarks and gluinos of at least 800 GeV (Fig. 2.6). In addition leptons will be produced in large amounts,iIn the studied scenario mainly τ leptons. As already mentioned the gravitino will cause a great amount of missing transverse energy. The presented analysis will therefore concentrate on the number of reconstructed τ leptons and missing transverse energy. Chapter 5 is devoted to those two variables and their expected performance.

Chapter 3

The ATLAS Detector at the LHC

In the following the LHC and the ATLAS detector are briefly introduced.

3.1 The Large Hadron Collider

The Large Hadron Collider (LHC) is a proton-proton-collider located at the site of CERN. More details can be found in [16, 17]. It started running in September this year. The LHC is located in the former LEP tunnel with a circumference of 27 km and will provide proton-proton collisions at a center-of-mass-energy of up to 14 TeV at a frequency of 40 MHz. The design luminosity is $\mathscr{L} = 10^{34}\,\mathrm{cm}^{-2}\mathrm{s}^{-1}$.

Inside the accelerator, two beam pipes host the proton bunches in an ultrahigh vacuum. 9300 superconducting magnet components operate at a temperature of 1.7 K. 1232 dipole magnets of 15 m length each provide a field of 8.3 T keeping the bunches on their tracks. The beam is focused by 392 quadrupole magnets of a length between 5 and 7 m.

In order to discover beyond the SM physics often having cross sections in the order of a few picobarn (pb)[1] very high event rates are necessary. The event rate $\frac{\mathrm{d}N}{\mathrm{d}t}$ can be calculated by multiplying the cross section σ with the luminosity $\mathscr{L}$

$$\frac{\mathrm{d}N}{\mathrm{d}t} = \sigma \cdot \mathscr{L}, \tag{3.1}$$

where the luminosity is given as

$$\mathscr{L} = f N_B \frac{N_1 N_2}{4\pi\sigma_x\sigma_y}. \tag{3.2}$$

f is the revolution frequency of 40 MHz, N_B denotes the number of the bunches and N_1, N_2 the number of the particles per bunch. The expansion of the bunches perpendicular to the beam axis is described by σ_x and σ_y.

It is intended to start running with a luminosity of $\mathscr{L} = 10^{31}\,\mathrm{cm}^{-2}\mathrm{s}^{-1}$ during the low luminoisity phase. By increasing the number of bunches and the number

---

[1] $1\,\mathrm{b} = 10^{-28}\,\mathrm{m}^2$

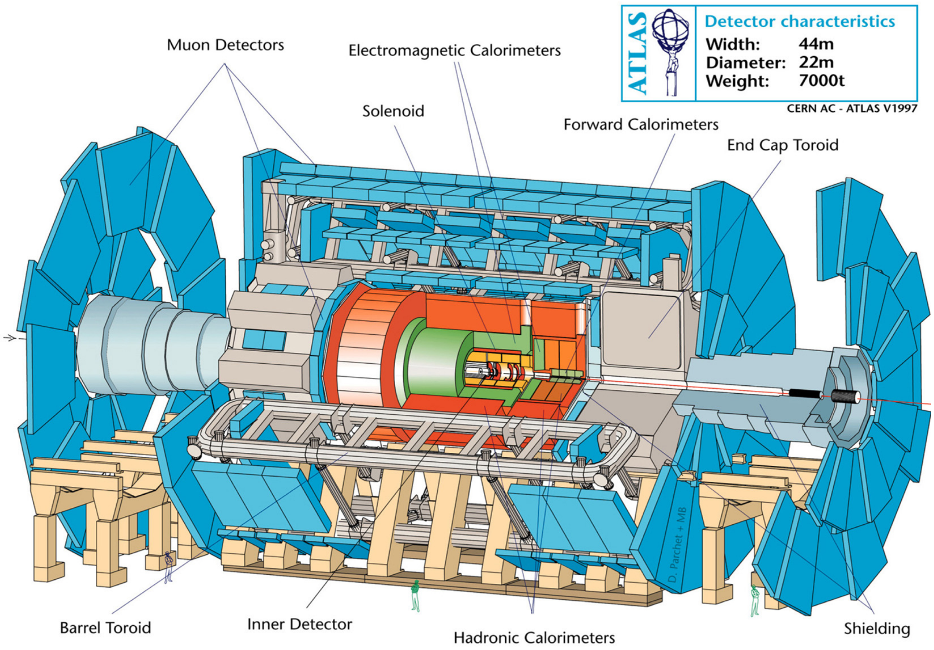

Figure 3.1: Overview over the entire ATLAS detector showing the Inner Detector (yellow), the electromagnetic (green) and hadronic calorimeter (orange), the muon (blue) and the magnet system (grey) [20].

of particles per bunch and by reducing the expansion of the bunches the LHC will reach a luminosity of $\mathscr{L} = 10^{33}\,\mathrm{cm}^{-2}\mathrm{s}^{-1}$ and deliver an integrated luminostiy of approximately $\int \mathscr{L}\mathrm{d}t = 10\,\mathrm{fb}^{-1}$ of data per year. As soon as the LHC reaches its design luminosity it will be able to deliver $100\,\mathrm{fb}^{-1}$ of data per year.

The six experiments at the LHC are first of all the two multipurpose detectors ATLAS[2] [18] and CMS[3] [19] which will concentrate on precision measurements of the SM, the search of the Higgs boson, and beyond the SM physics. On the other hand there are LHCb, ALICE[4], TOTEM[5] and LHCf[6] which are dedicated to more specific questions. LHCb will further investigate B-physics especially CP-violation in hadrons containing b quarks. ALICE will focus on the ion-ion-collisions that are also planned at the LHC for research of quark-gluon-plasma. TOTEM will measure elastic and inelastic proton-proton scatterings where either one or both protons stay intact in order to determine the size of the proton and the luminosity of the LHC. Forward particles created inside the LHC are used by LHCf as a source to simulate cosmic rays in laboratory conditions.

---

[2] A Toroidal LHC Appartus

[3] Compact Muon Solenoid

[4] A Large Ion Collider Experiment

[5] TOTal Elastic and diffractive cross section Measurement

[6] Large Hadron Collider forward

Detector component	Required resolution	η coverage	
		Measurement	Trigger
Tracking	$\sigma_{p_T}/p_T = 0.05\% p_T \oplus 1\%$	± 2.5	
EM calorimetry	$\sigma_E/E = 10\%/\sqrt{E} \oplus 0.7\%$	± 3.2	± 2.5
Had. calorimetry			
barrel and end-cap	$\sigma_E/E = 50\%/\sqrt{E} \oplus 3\%$	± 3.2	± 3.2
forward	$\sigma_E/E = 100\%/\sqrt{E} \oplus 10\%$	$3.1 < \lvert\eta\rvert < 4.9$	$3.1 < \lvert\eta\rvert < 4.9$
Muon Spectrometer	$\sigma_{p_T}/p_T = 10\%$ at $p_T = 1\,\mathrm{TeV}$	± 2.7	± 2.4

Table 3.1: General performance goals of the ATLAS detector [18].

3.2 The ATLAS Detector

ATLAS will investigate a wide range of physics, including the search for the Higgs boson, extra dimensions, and particles serving as dark matter candidates. The detector was designed in order to profit at most from the high event rates and to assure a long term operation despite the high radiation level. The inelastic proton-proton cross section of 80 mb will dominate all other processes. Therefore, every event will be accompanied by three to 23 inelastic events per bunch-crossing depending on the luminosity, so-called *pile-up*.

Therefore, the ATLAS detector is required to offer a good resolution concerning the particle momentum. It is essential that the particle identification is correct including the measurement of the charge of particles. A good reconstruction efficiency is needed as well as a precise measurement of the jet energy for a correct determination of the missing transverse energy. Besides a highly efficient trigger is indispensable in order to achieve an adequate background rejection.

Figure 3.1 shows a complete overview of the ATLAS detector displaying the main components. The innermost part is the Inner Detector (Sect. 3.3) consisting of a pixel and silicon microstrip tracker (SCT[7]) and the Transition Radiation Tracker (TRT). It is enclosed by a superconducting solenoid providing a magnetic field of 2 T. The electromagnetic and hadronic calorimeter (Sect. 3.4) surround the Inner Detector. The outermost part is the muon system (Sect. 3.5). The performance goals concerning energy and momentum resolution are listed in Table 3.2 for the individual components.

3.2.1 The Coordinate System and Kinematic Variables

The origin of the coordinate system coincides with the interaction point in the center of the detector. The direction of the anti-clockwise beam determines the z-axis. The x-axis points to the center of the LHC and the y-axis points upwards. Those two axes define the azimuthal angle ϕ in such a way that $\tan\phi = \frac{y}{x}$. The

---

[7] SCT: semiconductor tracker

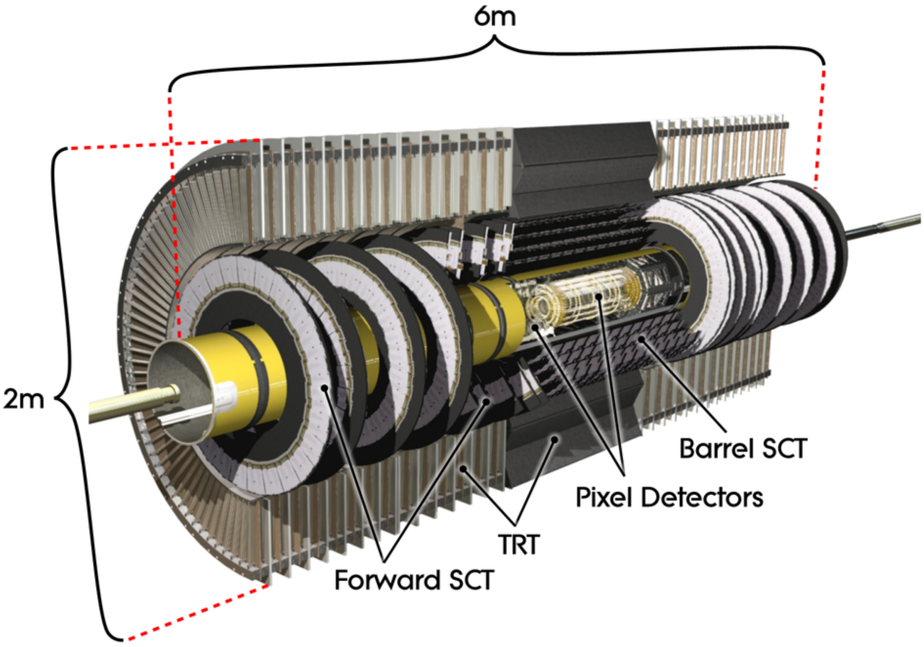

Figure 3.2: The Inner Detector consisting of the pixel and silicon microstrip tracker (SCT) and the Transition Radiation Tracker (TRT) [18].

polar angle is measured from the beam axis and is used to define the pseudorapidity

$$\eta = -\ln \tan\left(\frac{\theta}{2}\right). \tag{3.3}$$

The coverage in η for each detector component is also listed in Table 3.2. The fiducial distance of two objects is indicated in the η-ϕ plane as

$$\Delta R = \sqrt{(\Delta\eta)^2 + (\Delta\phi)^2}. \tag{3.4}$$

The transverse momentum $p_T = \sqrt{p_x^2 + p_y^2}$ and the (missing) transverse energy $E_T(\not{E}_T)$ are also defined in the plane perpendicular to the beam axis.

3.3 The Inner Detector

The Inner Detector [21] is designed to measure the particle momentum and primary and secondary vertices. A schematic illustration is given in Fig. 3.2. It is 6 m long, its diameter is 2 m and it covers a region of $|\eta| < 2.5$. The magnetic field bends the particle tracks and hence the particle momentum and their charge can be measured. The combination of this information and the energy measurement of the calorimeter allows the identification of particles. The general design of the detector components is an arrangement of concentric cylinders around the beam axis in the barrel region and disks perpendicular to the beam in the end-cap region.

3.3.1 The Pixel and the Silicon Microstrip Detector

The main task for the silicon detectors is to allow a very good track-finding and pattern recognition by providing three position measurements of charged particles in the pixel detector and eight in the silicon strip detector. It measures the impact parameter and enables the discrimination of short-lived particles such as hadrons containing b-quarks and τ leptons which is essential for the following analysis.

Since the pixel detector is closest to the interaction point it is exposed to the highest track density and radiation level. It consists of three cylindrical layers and three discs. The minimum size of the identical pixel sensors is $50 \times 400\,\mu\text{m}^2$ providing a spatial resolution in the $R - \phi$ plane of $10\,\mu$m and in R (barrel) and z (end-cap) of $115\,\mu$m. The number of readout channels amounts to 80.4 million which is about 90 % of the total number of readout channels of the ATLAS detector.

The components of the silicon microstrip detector are eight strip layers in the barrel region whereas two layers are combined in a pair glued back-to-back at an stereo angle of 40 mrad. In the end-cap region, nine silicon disks use strip layers combined to pairs with the same stereo angle of 40 mrad. Each sensor is 6 cm long and the strip pitch is $80\,\mu$m. The accuracy of the position measurement is estimated to be $17\,\mu$m in the $R - \phi$ plane and $580\,\mu$m in R as well as z.

3.3.2 The Transition Radiation Tracker

The transition radiation tracker (TRT) is a drift chamber system of roughly 370 000 straw tubes containing a gas mixture of $70\%\,\text{Xe}, 27\%\,\text{CO}_2$ and $3\%\,\text{O}_2$. The diameter of the straw tubes is 4 mm whereas their length varies between 37 cm (end-cap) and 144 cm (barrel). They are equipped with a goldcased tungsten wire as anodes and aluminium cased coats as cathodes.

The basic principle of the TRT is ionization which occurs every time a charged particle traverses gas. In addition, ultra-relativistic particles such as electrons emit transition radiation leading to a higher signal in the detector. Therefore, the transition radiation tracker is equipped with two tresholds optimized for the discrimination of pions and electrons. In addtion, the drift time in each tube is measured providing the distance of the track from the read-out wire. The TRT provides up to 36 position measurements with an overall resolution of $130\,\mu$m in $R - \phi$.

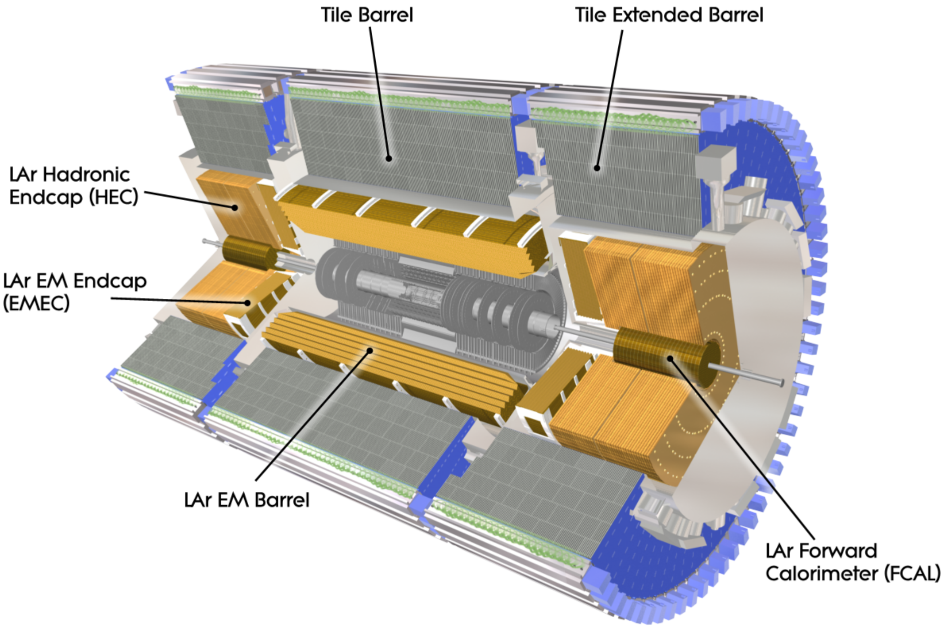

Figure 3.3: The calorimeter system includes an electromagnetic calorimeter, hadronic calorimeters in the barrel and end-cap region and a forward calorimeter [18].

3.4 The Calorimeters

The calorimetry [22] is composed of four parts namely the electromagnetic calorimeter, the hadronic tile calorimeters, the hadronic end-cap calorimeter and the forward calorimeter. A schematic overview is presented in Fig. 3.3.

The central purpose of the calorimeter system is the measurement of the particle energy. Particles will generate a shower of particles depositing their energy in the calorimeter. Electrons and photons will interact with the electromagentic field of the nuclei of the active material emitting bremsstrahlung or creating electron-positron pairs. Hadrons on the other hand interact strongly with the nuclei.

The ATLAS calorimeter system uses so-called *sampling calorimeters* that feature a non-homogeneous structure consisting of passive as well as active absorber materials. The former causes the production of secondary particles and the latter is meant for the actual measurement of the energy.

Crucial for the following analysis is an accurate measurement of $\not{E}_T$ caused by undetectable escaping gravitinos and neutrinos from τ decays. Therfore, the calorimeters must cover as much of the $\eta - \phi$ plane as possible. It is essential that the calorimeters absorb the entire energy of particles to prevent the showers to propagate through the electromagnetic or the hadronic calorimeter and contaminate either the hadronic calorimeter or the muon system respectively.

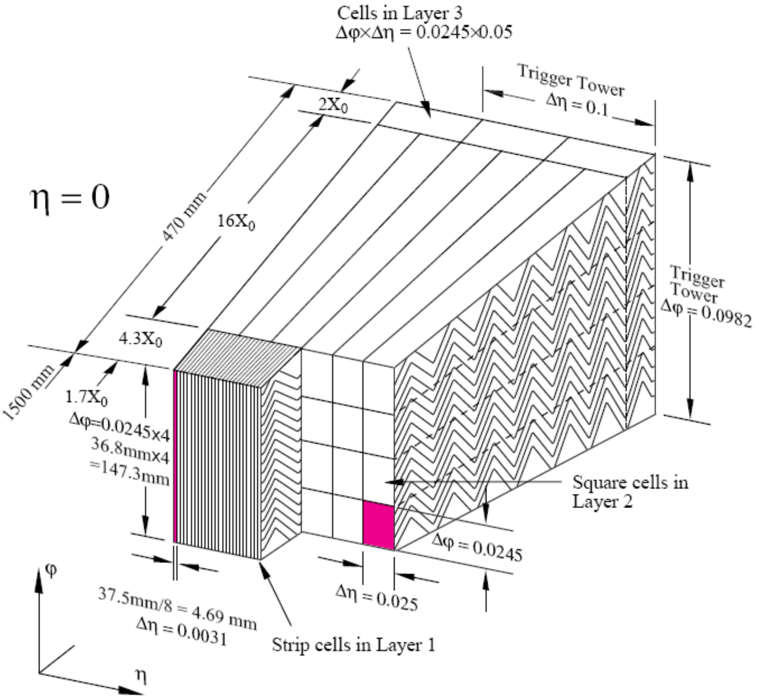

Figure 3.4: The electromagnetic calorimeter [18].

3.4.1 The Electromagnetic Calorimeter

The electromagnetic calorimeter is a lead liquid argon (LAr) detector arranged in layers of lead as absorber and liquid argon as active material for detection. The accordian shaped structure has the advantage of complete ϕ uniformity and is shown in Fig. 3.4.

The calorimeter is segmented in three samplings. The first one is equipped with very fine so-called η-strips at an interval of 4.7 mm. It allow the measurement of the η position of particles very precisely and e.g. distinction of two photons coming originating from a neutral pion decay which is of interest when reconstructing τ leptons. The second part is the longest and divided into cuboidal cells with a base area of $\Delta\eta \times \Delta\phi = 0.025 \times 0.025$ absorbing most of the energy. The third layer is twice as broad in η as the second one.

The barrel calorimeter consists of two identical half-barrels covering the region $|\eta| < 1.475$. Each end-cap calorimeter features an outer and an inner wheel covering either approximately $1.375 < |\eta| < 2.5$ or $2.5 < |\eta| < 3.2$ respectively. For correction of energy losses in the Inner Detector and the cryostats a presampler is prepended to the electromagnetic calorimeter which consists of one active layer of LAr.

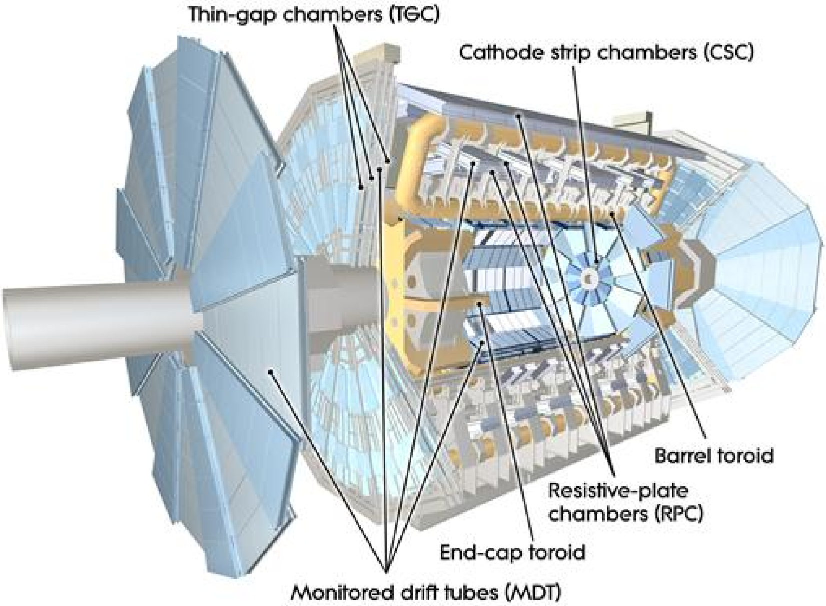

Figure 3.5: The muon system containing different chamber types and air-core toroids [18].

3.4.2 The Hadronic Calorimeter

As mentioned above the hadronic calorimter is composed of three parts and covers the range $|\eta| < 4.9$. It is directly affiliated to the electromagnetic calorimeter.

The tile calorimeter consists of a barrel part ($|\eta| < 1.0$) and two extended barrels ($0.8 < |\eta| < 1.7$). It reaches from an inner radius of 2.28 m to 4.25 m. It is a sampling calorimeter using plastic scintillator plates, so-called *tiles* enclosed in a steel absorber.

In the end-cap two wheels form the LAr hadronic end-cap calorimeter covering $1.5 < |\eta| < 3.2$. It overlaps slightly with the tile calorimeter as well as the forward calorimeter. The copper absorber is arranged in parallel plates and interleaved by LAr layers serving as the active material.

The forward calorimeter ($3.1 < |\eta| < 4.9$) is a dense LAr calorimter consisting of three modules which use two different absorbers. The first module features copper aiming at electromagnetic measurements and the other two are made out of tungsten which measure the energy of hadron showers.

3.5 The Muon System

Since muons do not interact strongly and have a higher mass than electrons they deposit hardly any energy in either of the calorimeters. Hence a dedicated subdetector is needed for further particle identification and for the measurement of their energy. The muon system of ATLAS includes monitored drift tubes (MDT) and cathode strip chambers (CSC). It is completed by thin-gap chambers (TGC) and resistive plate chambers (RPC). The TGCs are installed in the end-cap and the RPCs in the barrel region. An overview over all components is shown in Fig. 3.5. Eight barrel toroids and two end-cap toroids provide a magnetic field of up to 3.9 T to deflect the muon path over a range of $|\eta| < 2.7$. The toroids are superconducting air-core magnets.

The purpose of the MDTs and CSCs is to measure the muon tracks very precisely. They take advantage of the ionization that takes place as soon as a muon traverses the gas and measure the drift time. Most of the barrel range ($|\eta| < 2.7$) is covered by MDTs. The tubes are out of aluminium and possess a diameter of 30 mm. They are filled with 93% Ar and 7% CO_2 and tungsten-rhenium wires serve as the anodes. The spatial resolution achieves values of 80 μm.

The CSCs are used at larger η. They are multi-wire proportional chambers with cathodes segmented into strips. They offer a higher granularity than the MDTs because of the higher background expected. Therefore, a higher spatial and time resolution is needed provided by the CSCs. The used gas mixture (30% Ar, 50% CO_2, 20% CF_4) differs slightly from the one used in the MDTs.

The MDTs and CSCs are either arranged in three layers cylindrical in the barrel around the beam axis or in disks perpendicular to the beam in the end-cap. In the barrel one set of chambers is located inside the toroid. Here the sagitta instead of the deflection of the muon track is used for momentum measurement. In the end-cap this is done by measuring the different angles of the muon entering and exiting the chambers.

The TGCs and the RPCs are on one hand part of the First Level Trigger which will be described in further detail in Set. 3.6. On the other hand they identify the bunch-crossings allocating the muons to the correspondig event. In addition, the muon coordinates in the direction orthogonal to that of the precision tracking chambers are measured. The RPC are gaseous detectors with parallel Bakelite plates which serve as anodes. The TGC function similar to the CSCs but have smaller distances between anodes and cathodes and hold a different gas mixture.

The overall performance is determined by the alignment of muon chambers especially if the muons have high p_T values. In the case of high p_T muons, the performance is independent of the Inner Detector system.

3.6 The Trigger System

A trigger system is necessary because the rate of interactions (40 MHz) is so high that it is not possible to store all event data. Soft QCD interactions, so-called *minimum bias events*, are studied in a reasonable amount but will not contribute to the searches for new physics and therefore the majority of the events containing elastic proton-proton interactions have to be rejected. The main purpose of the trigger system is to select those events which are considered interesting and reject those of lower interest. Figure 3.6 shows the trigger chain the data passes.

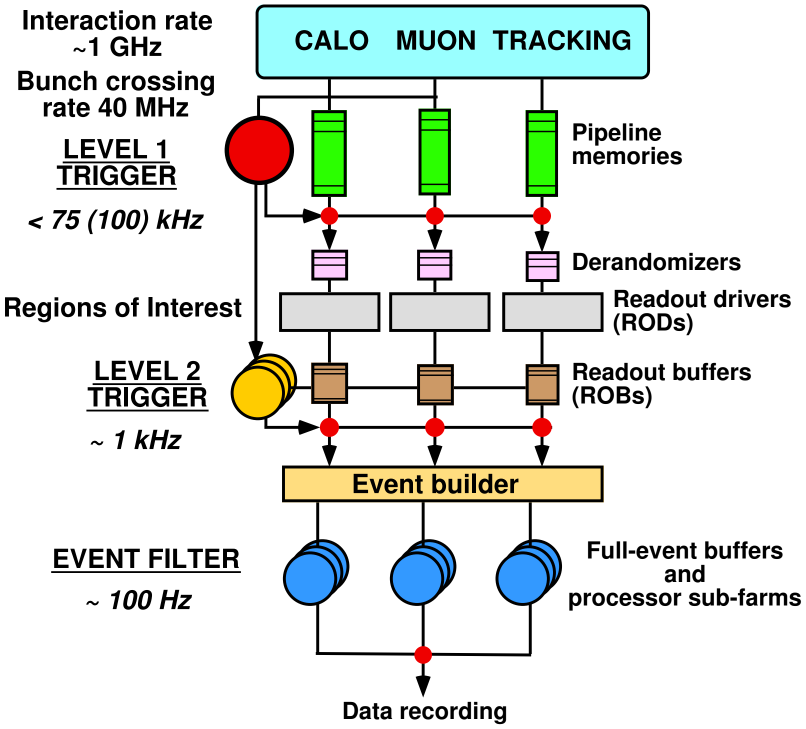

Figure 3.6: The ATLAS trigger system including the First-Level Trigger and the High Level Trigger, consisting of the Level-2 Trigger and the Event Filter [23].

The ATLAS trigger system is a three level trigger composed of the first trigger level (L1) [23], second trigger level (L2) and the Event Filter (EF). The latter two form the High-Level Trigger (HLT) [24] which is software based whereas L1 is fully hardware based.

A dedicated hardware system gets the information out of the detector electronics and passes them on to the First-Level Trigger which has a latency of 2.5 μs. The rejection of events is based on coarse information from the calorimeters and the muon system. It reduces the event rate to about 75 kHz. The main focus are particles (leptons, photons, jets) with high p_T and large total energy or $\not{E}_T$. L1 defines so-called *Region-of-Interests* (RoIs) whose full read-out data account only for about 2 % of the full detector read-out data.

The HLT accesses more information of the detector reducing the event rate to 200 Hz. Decisions are derived step by step refining the decision of the previous trigger by taking into account more information from different subdetectors and surveying additional selection criteria yielding early rejection of events that do not meet specific demands.

The time latency of L2 is about 40 ms. The L2 reduces the event rate to 3.5 kHz using the detector data inside the RoIs at full granularity and precision. The decision of the event filter can take up to a few seconds and is based on offline analysis procedures.

Chapter 4

Event Simulation

The preparation for the physics analyses of real data from the ATLAS detector is done by generating and simulating events in advance. These events can be analyzed towards signatures from SM processes and new physics. They serve as cross check as well. The whole chain of the generation and simulation of events can be seen in Fig. 4.1.

First, Monte Carlo generators such as HERWIG or ALPGEN generate events. They determine the produced particles in proton-proton collisions using probabilities derived from matrix elements fitting the SM or an assumed model of new physics. The output are HEPMC files containing particles and their four-momentums which are passed on to GEANT4.

GEANT4 simulates the interaction of the particles with the ATLAS detector and digitizes the detector response. These GEANT4 digits are equivalent to real data.

Offline software algorithms process these simulated event data and reconstruct the particles produced in the events. It is common that for every kind of particles a different algorithm is used. The physics analyses are performed on these reconstructed objects. This thesis will concentrate on the reconstruction algorithm of τ leptons whose accuracy and efficiency is discussed in Sect. 5.1.

Due to the accuracy of the described chain, producing one event can take up to 15 minutes. Since large amounts of data are required for the various analyses a fast simulation is additionally used. Instead of simulating the passage of the particles through the detector and reconstructing them the reconstructed particles are created directly from the generated event information. A comparison of results of the full simulation and the fast simulation is presented for variables crucial in this analyis in Sect. 5.3

4.1 Monte Carlo Generators

Monte Carlo generators are used for the event generation for specific collisions. For this analysis proton-proton-collisions are studied. The various generators differ in

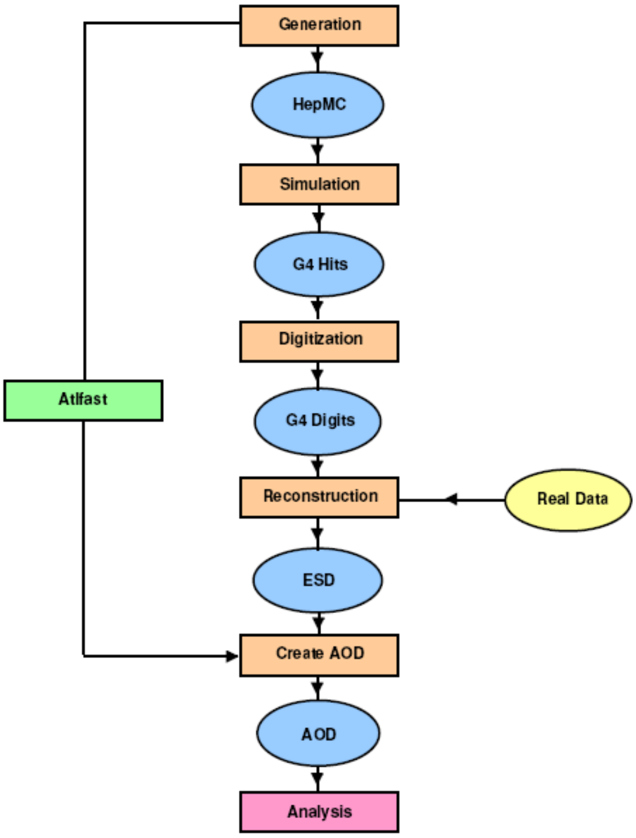

Figure 4.1: Schematic representation of the full chain of Monte Carlo production [25]. The rectangles symbolize the neccessary steps and the ellipses indicate the data formats of the corresponding output.

the specific way of the hard scattering and the hadronization. The main principal of event generation is described in the following.

- The primary **hard scattering** is determined according to QCD cross sections calculated by the use of perturbative QCD and multiplying them with the structure function of each proton. For SUSY events, gluinos and squarks are produced through gluon-gluon or gluon-quark fusion (Fig. 2.8) or through quark-quark interaction.

- Initial and final state **QCD radiative corrections** are applied by the emission of gluons from initial or final quarks. For initial state radiation the structure functions of the protons are considered. The radiation of high-energetic partons is suppressed but radiation of gluons from gluinos or squarks is followed. In the final state the radiation of photons, W or Z bosons is added.

- As a next step **partons** need to be **fragmented into hadrons**. Partons split corresponding to $q \rightarrow qg$ or g $\rightarrow q\overline{q}$ evolving into hadronic showers. The produced elemantary particles are combined to color neutral hadrons.

- **Beam jets** are added at the remaining energy.

4.1.1 ISAJET

ISAJET [26] is a Monte Carlo generator which can generate events at very high energies for three different reactions: pp, $p\bar{p}$ and e^+e^- making it suitable for the LHC, the TeVatron and ILC studies. However, in this thesis only the integrated program ISASUGRA is used for the calculation of the mass spectrum (Table A.1) and the branching fractions of the particles suiting the ATLAS benchmark point GMSB6 (Table 2.4). This mass spectrum and the branching fractions are given to HERWIG generating events.

4.1.2 HERWIG

HERWIG [27] is a showering and hadronization event generator. HERWIG can be used for the generation of SM or new physics processes especially SUSY including R-parity conservation and violation models.

Parton showers are used for initial as well as final state radiation. Initial and final state jet evolution follow an angular ordering including soft gluon interference whereas color coherence of all partons is regarded in all subprocesses. The cluster model used for jet hadronization is based on non perturbative gluon splitting and for the underlying and soft events a similar cluster model is applied.

Primarily, HERWIG deals with the hard subprocess. The incoming particles such as partons from the proton interact producing primary particles based on perturbative QCD. Thereby the momentum transfer Q sets boundaries on the possible initial state and final state parton showers.

In a second step, the primary particles radiate partons reducing their momentum. The lost momentum is smaller for every radiation leading to smaller angles at which the secondary partons are emitted for every radiation which is called *angular ordering.*

Heavy particles are decayed. Their decay time can be in the same order of magnitude as the accumulation of parton showers so that heavy particles can also initiate parton showers.

At last the hadronization is accomplished. Partons are combined into hadrons at low momentum transfer. At that scale the strong coupling constant α_s is large and QCD is non perturbative. Therefore its description is based on phenomenological models. Partons are combined to color neutral clusters which decay into hadrons. The partons of the protons not participating in the hard scattering are taken into account in the so-called *underlying event* that is modelled following soft minimum bias collisions.

4.1.3 ALPGEN

ALPGEN [28] differs from HERWIG because on one hand it is only intended for multiparton hard processes in hadronic collisions. On the other hand electroweak and leading order QCD interactions are exactly calculated. The parton shower model as described above is used in addition.

It is possible to calculate the exact matrix elements for many parton level processes whereas no contributions from feynman graphs with loops are taken into account. After the generation of events on parton-level with the full information on color and flavor these partons are then evoluted into hadronic states.

As a first step the cross section for a given hard process is calculated taking into account the jet multiplicity, the masses of heavy quarks and requirements on transverse momentum or rapidity. Then the matrix elements are calculated in leading order also including the mass of heavy quarks, the polarization, flavor and color of all partons. Electroweak couplings are calculated at tree level. There no hadronization will take place. Produced single quarks and gluons are instead forwarded to a different program that takes care of parton showers.

ALPGEN was used for the production of the SM background samples.

4.2 Detector Simulation

When using the full simulation, after the event generation the detector response is simulated by GEANT4 [29] taking the full detector geometry into account. The fast simulation dispenses with the detector simulation and creates reconstructed objects directly.

4.2.1 GEANT4

GEANT4 (GEometry ANd Tracking) is used for design studies and the optimization of the ATLAS detector as well as for the development and testing of the various reconstruction tools. In addition it will serve as cross check through comparisons with real data.

GEANT4 operates as an electronic reproduction of the ATLAS detector with special emphasis on the geometry and the different materials of the detector components described in detail in Ch. 3. It simulates the passage of the particles through the matter enclosed in the ATLAS detector considering possible electromagnetic and hadronic interactions of the particles with the detector until the particles exit the detector or until the particle energy is completely deposited inside the calorimeter. In addition the influence of the different magnetic fields is taken into account.

GEANT4 is able to treat long-lived particles correctly. Otherwise it produces secondary particles, e.g. conversions or bremsstrahlung photons. It simulates energy losses due to interactions of the particles with the material. These energy losses include the simulation of the detector response, creating so-called *hits* where the particles interacted with the detector. The hits are digitized and used for building tracks and the reconstruction of the particles and their possible decay products.

The range of the particle energy that are handled by GEANT4 covers ten orders of magnitude reaching from less than keV to several TeV.

4.2.2 ATLFAST I

ATLFAST I [30] is the fast simulation of ATLAS. Instead of simulating every interaction of each individual particle the detector is parametrized and the reconstructed particles are directly created from the generated particles. This is done by a cone algorithm scanning the calorimeters for seeds. The built calorimeter clusters are geometrical matched to true particles. In addition resolution functions on the particle energy are applied.

For stable particles the impact on the calorimeter surface is calculated. They are tracked through the magnetic field which is homogenous disregarding any possible interaction of the particles with the detector. One of the consequences is that the particles lose no energy. This is however addressed later on in the calculation of the energy resolution.

The electromagentic and hadronic calorimeter are not distinguished and their substructure is ignored. Instead they are assumed to be uniform over the entire detector range except that the granularity is four times smaller in the endcap region than in the barrel region. One single particle can only deposit its energy in one cell leaving aside the shape of a cluster the particle might induce.

There is no simulation of any tracks in the Inner Detector or the muon system. The procedure for all kinds of particles is described in the following.

Clusters: For the reconstruction of clusters a cone algorithm with a cone of $\Delta R = \sqrt{\Delta\eta^2 + \Delta\phi^2} < 0.4$ forms clusters of at least $5\,\mathrm{GeV}$. It is based on the energy deposited in the calorimeter cells whereas cells with the most energy depostion are dealt with first and then in descending order the algorithm is applied to all cells containing more than $1.5\,\mathrm{GeV}$. Every cell is associated to only one cluster though a cluster can be declared to be a specific particle later on and will no longer be a cluster.

Electrons: The first step is to associate one isolated cluster to every generated electron wherever possible. If the energy of the electron and the cluster are similar the energy of the generated electron is smeared out by a resolution function depending on η and taken as the reconstructed energy.

Photons: Photons are handled very similar to the electrons. They also have to be isolated but there is an additional smearing of η.

Muons: Muons have to be isolated as well otherwise they are associated to a jet. Each muon with a generated momentum of at least 0.5 GeV is considered. If the resontructed p_T of the muon exceeds 5 GeV after the smearing it is kept.

Jets: Every cluster left until this point with a transverse energy of $E_T > 10\,\mathrm{GeV}$ is accounted a jet. A smearing of the energy is applied. The direction of the jet is identical to the direction of the primary cluster. Since at this point the calorimeter response is taken to be ideal the energy of the jets has to be corrected later on.

Taus: Only hadronically decaying taus are of interest. Tau reconstruction includes labelling of jets as taus which fulfill two criteria and applying identification efficiencies which are taken from full simulation. The first step of the labelling is similar to electrons. For every tau a reconstructed jet in $\Delta R < 0.3$ is sought. It is required that

$$\frac{E^{\tau}}{E^{jet}} = 1 - \frac{2\sigma(p_T^{jet})}{p_T^{jet}},$$

where τ means the visible part of a true τ lepton and jet denotes the reconstructed jet considered a reconstructed τ candidate.

b- and c-jets: The specific jet reconstruction procedures work very similar to that of τ leptons. At first a labelling is carried out. If a true b- or c-quark is in a range of $\Delta R < 0.2$ of a reconstructed jet it is considered a b-jet or a c-jet. Tagging efficiencies are applied.

Missing transverse energy: The $\not{E}_T$ is calculated from all recontructed objects described above including all clusters not associated to a jet and all cells not associated to a cluster.

In the whole reconstruction procedure no reconstruction efficiencies are applied. Only some efficiency factors are taken implicity into account for the tagging of τ leptons and b jets.

4.2.3 ATLFAST II

ATLFAST II ranges between ATLFAST I and full simulation in time as well as in simulation detail. In contrast to ATLFAST I the simulation and reconstruction is not done as one step but the same reconstruction algorithms as in full simulation are used.

At the moment the Inner Detector is simlulated as in the full simulation by using Geant4. It is intended to provide a fast track simulation additionally.

The calorimeter response is implemented in a similar way as in ATLFAST I. However, the calorimeter consists of two layers, one for each the electromagentic and the hadronic calorimeter. The particle energy response and the resolution is parametrized based on the full simulation of approximately thirty million photons and charged pions. The electrons are treated like photons and all other hadrons like charged pions. In addition the longitudinal shape of the energy distribution in the calorimeter samplings as well as the lateral shape of the particle energy deposition are added. The effect of electronic noise is added as a final step.

For the muon system both the full and the fast approach can be used. If the full simulation is used all particles are run through full simulation of the Inner Detector. Every particle except the muons are discarded at the exit of the Inner Detector (Sect. 3.3). Muons are treated as in full simulation in the calorimeter as well as in the muon system. For all other particles the calorimeter simulation is done by a fast simulation. This approach was chosen for this study.

For the fast simulation of the muons no combination with an Inner Detector track is attempted. Track and calorimeter isolation variables are calculated. Since the muons are not simulated by FastCaloSim, calorimeter isolation lacks the effects of the muon energy deposition in the calorimeter and these muons are not added to missing transverse energy.

Since ATLFAST II is a combination of full and fast simulation it is ten times faster than the full simulation but up to a hundred times slower than the fast simulation.

Chapter 5

Studies on the Reconstruction of τ Leptons and Missing Transverse Energy

The analysis presented here relies heavily on the reconstruction of hadronic τ decays and $\not{E}_T$. The main reconstruction mechanisms and their expected performance are discussed in the following.

5.1 The Reconstruction of Hadronic τ Decays

The τ lepton is with a mass of $m_\tau = 1.78\,\mathrm{GeV}$[31] the heaviest lepton. It has a mean lifetime of $\tau_\tau = 2.9 \cdot 10^{-13}\,\mathrm{s}$ and several decay channels. It decays leptonically as well as hadronically, primarly into pions. Table 5.1 lists the most important decay modes and their branching fractions.

The presence of neutrinos in the final state of the τ decay prevents the complete reconstruction of the τ momentum. The reconstruction of the leptonic decay modes of the τ lepton leading to two neutrinos in the final state suffers additionally from the difficult distinction from primary electrons or muons. The hadronic decay

Decay modes	BR
$\tau \rightarrow \mathrm{e}\ \nu_\mathrm{e}\ \nu_\tau$	17.8%
$\tau \rightarrow \mu\ \nu_\mu\ \nu_\tau$	17.4%
$\tau \rightarrow \pi^\pm\ \nu_\tau + \mathrm{n}\cdot\pi^0$	46.8%
$\tau \rightarrow \pi^\pm\ \pi^\pm\ \pi^\pm\ \nu_\tau + \mathrm{n}\cdot\pi^0$	13.9%
$\tau \rightarrow \pi^\pm\ \pi^\pm\ \pi^\pm\ \pi^\pm\ \pi^\pm\ \nu_\tau + \mathrm{n}\cdot\pi^0$	0.1%
modes with K	3.8%
others	0.2%

Table 5.1: The τ decay channels and their branching ratios [32].

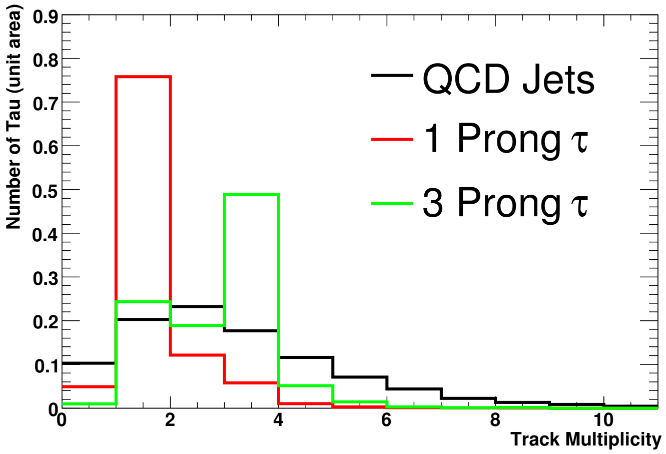

Figure 5.1: The reconstructed track multiplicity of τ candidates matched to one-prong, three-prong τ leptons, or QCD jets on generator level before requiring one to three tracks in one candidate.

modes are classified as so-called *one-prong* or *three-prong* decays indicating the number of charged particles in the τ decay.

A common property of τ decays is the low multiplicity of charged tracks (Fig. 5.1). In addition energy from charged or neutral hadrons is deposited in the calorimeter in a narrow cone around the initial τ direction leading to shower shapes different from jet or electron shower shapes. The main source for misidentified τ leptons are low-energetic jets with a low track multiplicity.

For the reconstruction of τ leptons [32] the ATLAS framework ATHENA offers two different algorithms. *TauRec* is based on calorimeter information and *Tau1p3p* relies on the information from the measurements of charged tracks. The former has been used in this analysis and will be described in the following.

5.1.1 The TauRec Algorithm

TauRec uses clusters in the calorimeter with $E_T \geq 15\,\text{GeV}$ and $|\eta| < 2.5$ as seeds for the τ reconstruction. It then associates tracks within a cone of $\Delta R < 0.3$ around the barycenter of the cluster to the τ candidate. Track information, e.g. the p_T or the charge of the tracks, is measured in the Inner Detector. Due to the unmeasured neutrinos the invariant mass of the associated tracks is required to be smaller than m_τ.

Electron-like tracks and tracks associated with a track segment in the muon spectrometer are rejected. Tracks of a τ will be well collimated in η and ϕ and are required to originate from the same secondary vertex. Clusters and their associated tracks, isolated from the rest of activity in the event are considered τ candidates.

In addition the following track selection criteria are applied to the candidates:

- $p_T > 2.0\,\text{GeV}$: The rejection of tracks falling below this threshold vetoes misidentified and conversion tracks.

- $d_0 < 1.5\,\mathrm{mm}$: d_0 is the impact parameter of the track denoting the smallest distance from the track to the beam axis. This cut assures that all associated tracks originate from the same secondary vertex.
- $\chi^2/\mathrm{ndf} < 3.5$: The quality of the track fit (χ^2) per degree of freedom (ndf) is used to select good tracks.
- Number of Si hits (pixel + SCT) ≥ 6: As described in Sect. 3.3 the Pixel detector can measure three coordinates and the silicon microstrip detector can offer eight measurements. At least six hits have to be associated to each track.
- Number of pixel + B-layer hits ≥ 1: There has to be at least one hit either in the Pixel detector or in the innermost layer, B-layer, used for the reconstruction of displaced vertices from short-lived particle such as b-quarks or the τ lepton. This requirement suppresses conversions of photons from the decay of neutral pions in the τ decays.

After this track selection only τ candidates with one to three tracks are further considered. Additional algorithms not discussed in detail here reject leptonically decaying τ which were accidently reconstructed as one-prong decays further improving the τ reconstruction. For further selection for each candidate a likelihood (LLH) is built from eight variables which are described in detail in the following. Their distributions for τ leptons and jets offering a transverse energy of $40-60$ GeV are shown in Fig. 5.2.

EM-Radius R_{em}: The EM-Radius denotes the distribution of the E_T among the cells in one cluster

$$R_{\mathrm{em}} = \frac{\sum_{i=1}^{n} E_{T_i} \sqrt{(\eta_i - \eta_{\mathrm{cluster}})^2 + (\phi_i - \phi_{\mathrm{cluster}})^2}}{\sum_{i=1}^{n} E_{T_i}} \tag{5.1}$$

where i runs over all n calorimeter cells in the cluster. It offers a good discrimination between τ leptons and jets at low E_T exploiting the narrow shower shape of the τ lepton. Higher values of E_T result in a stronger boost of τ leptons as well as jets and their shapes become more narrow and the separation power decreases. The measurement of R_{em} is influenced by the calorimeter granularity varying with η.

Isolation in calorimeter ΔE_T^{12}: The fraction of E_T in a ring of $0.1 < \Delta R < 0.2$ to all E_T in the cluster is defined as

$$\Delta E_T^{12} = \frac{\sum_{j=1}^{m} E_{T_j}}{\sum_{i=1}^{n} E_{T_i}} \tag{5.2}$$

where j runs over all m calorimeter cells in the ring and i over all n cells in the cluster. Due to the narrow cone, ΔE_T^{12} is in general smaller for τ leptons than for jets. It is dependent on E_T and less efficient for higher E_T values.

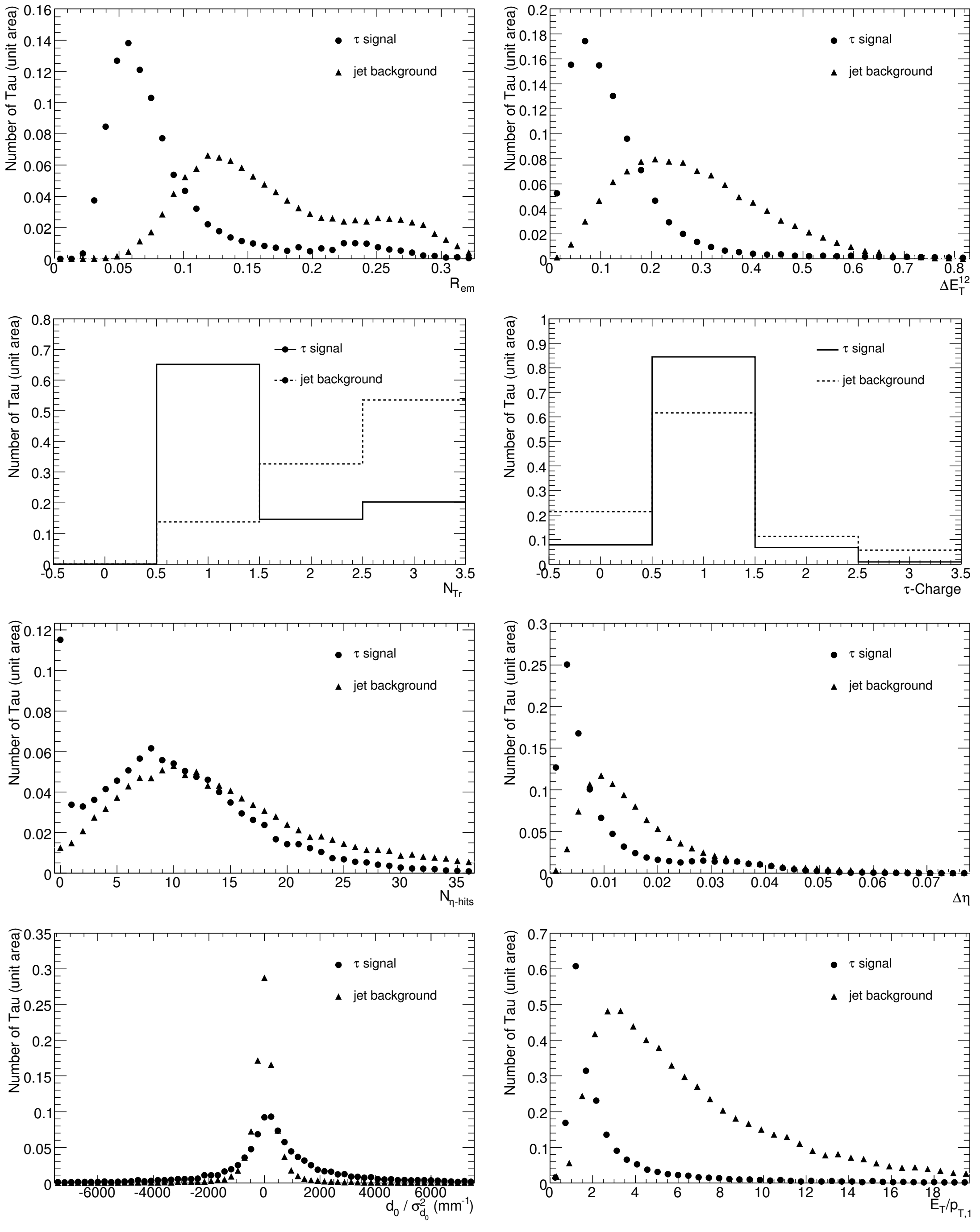

Figure 5.2: The distributions of the eight likelihood variables for τ leptons and jets [32].

Number of associated tracks N_{Tr}: The number of tracks associated with $p_T > 2\,\text{GeV}$ in a cone of $\Delta R < 0.3$ is used again because it has a good discrimination power being one or three in most cases for the τ signal.

τ-Charge: The charge of the τ candidate is defined as the sum of the measured charges of all tracks and should be ±1 for τ leptons.

Number of hits in the η strip layer $N_{\eta-\text{hits}}$: The number of hits in the first layer of the electromagnetic calorimeter which is very fine segmented in η. A cluster cell is counted as a hit if the energy deposition exceeds 200 MeV. The number of hits can be zero for low p_T τ leptons in contrast to jets tending to have more hits than τ leptons.

Transverse energy width in the η strip layer $\Delta\eta$: The dispersion of the energy in the first layer of the electromagnetic calorimeter is defined as

$$\Delta\eta = \frac{\sum_{i=1}^{n} E_{T_i}\sqrt{(\eta_i - \eta_{\text{cluster}})^2}}{\sum_{i=1}^{n} E_{T_i}}. \tag{5.3}$$

Its discrimination power between jets and τ candidates is better for low E_T due to the higher collimation of jets for higher values of E_T.

Lifetime signed pseudo impact parameter significance σ_{IP}: The two-dimensional lifetime signed impact parameter d_0 and its error σ_{d_0} are combined to

$$\sigma_{IP} = \frac{d_0}{\sigma_{d_0}} \cdot \text{sgn}(\sin(\phi_{\text{cluster}} - \phi_{\text{track}})). \tag{5.4}$$

Since the resolution for this variable increases with higher-energetic tracks the separation power for this variable increases as well.

E_T over p_T of the leading track $E_T/p_{T,1}$: The leading tracks of τ leptons are expected to carry the main fraction of the τ energy whereas the energy in a hadronic jet is rather smoothly distributed among the individual tracks. In addition jets contain more neutral objects than τ leptons offering a good separation except for very high E_T values.

For the final selection the combined likelihood constructed from the expected distribution of the individual observables shown in Fig. 5.2 has to exceed a value of two. Figure 5.3 illustrates the good separation power of the likelihood variable for τ leptons from QCD jets and the rejection of QCD jets as a function of the τ reconstruction efficiency. As expected the rejection of high-energetic jets exceeds the rejection of low-energetic jets. Since the boost increases with rising E_T the rejection reaches a saturation at $E_T \approx 100\,\text{GeV}$.

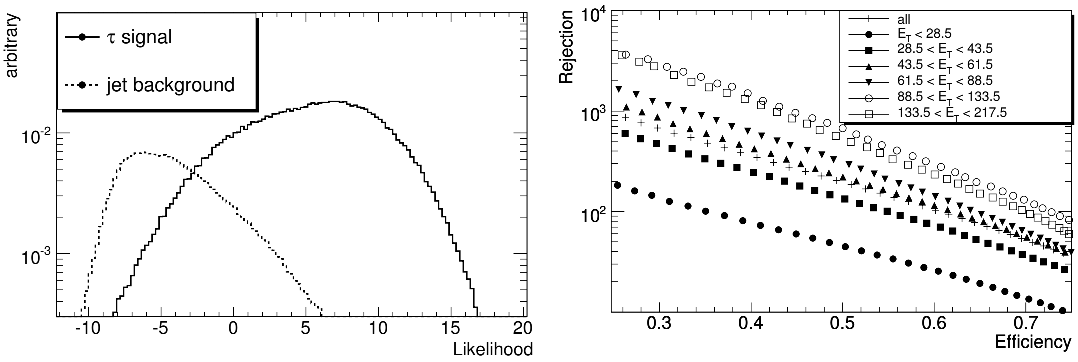

Figure 5.3: The different distribution for the combined TauRec likelihood for τ leptons and QCD jets (left). The rejection of QCD jets as a function of the τ reconstruction efficiency for different values of E_T (right) [32].

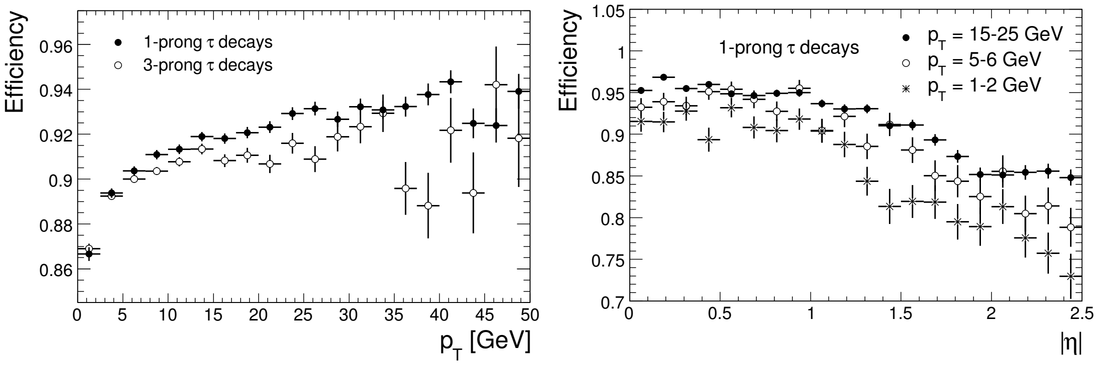

Figure 5.4: The expected reconstruction efficiency for charged pion tracks from one-prong and three-prong decays in W $\rightarrow \tau\ \nu_\tau$ and Z $\rightarrow \tau\ \tau$ events as a function p_T (left) and η of the pions for different bins of p_T (right) [18].

5.1.2 Expected Performance of TauRec

The described algorithm (TauRec) has been optimized for the reconstruction of τ leptons from heavy Higgs decays with an energy of their visible decay products of 30 GeV. Since in the supersymmetric scenario considered the mass difference of the selectron and the $\widetilde{\tau}$ is as low as 20 GeV (cf. Table A.1) this analysis will not be able to profit from the highest possible reconstruction efficiency.

Figure 5.4 shows the expected reconstruction efficiencies for charged pion tracks of hadronically decaying τ leptons in W $\rightarrow \tau\ \nu_\tau$ and Z $\rightarrow \tau\ \tau$ events achieving values of up tp 90%. In general the efficiency is higher for one-prong decays than for three-prong decays. In both cases it increases with p_T of the charged pion as the reconstruction suffers from hadronic interaction inside the Inner Detector.

In the low p_T range the limited track reconstruction efficienciency as well as the misreconstruction of one-prong decays as three-prong decays due to either additional tracks from the underlying event or from photon conversions can lead

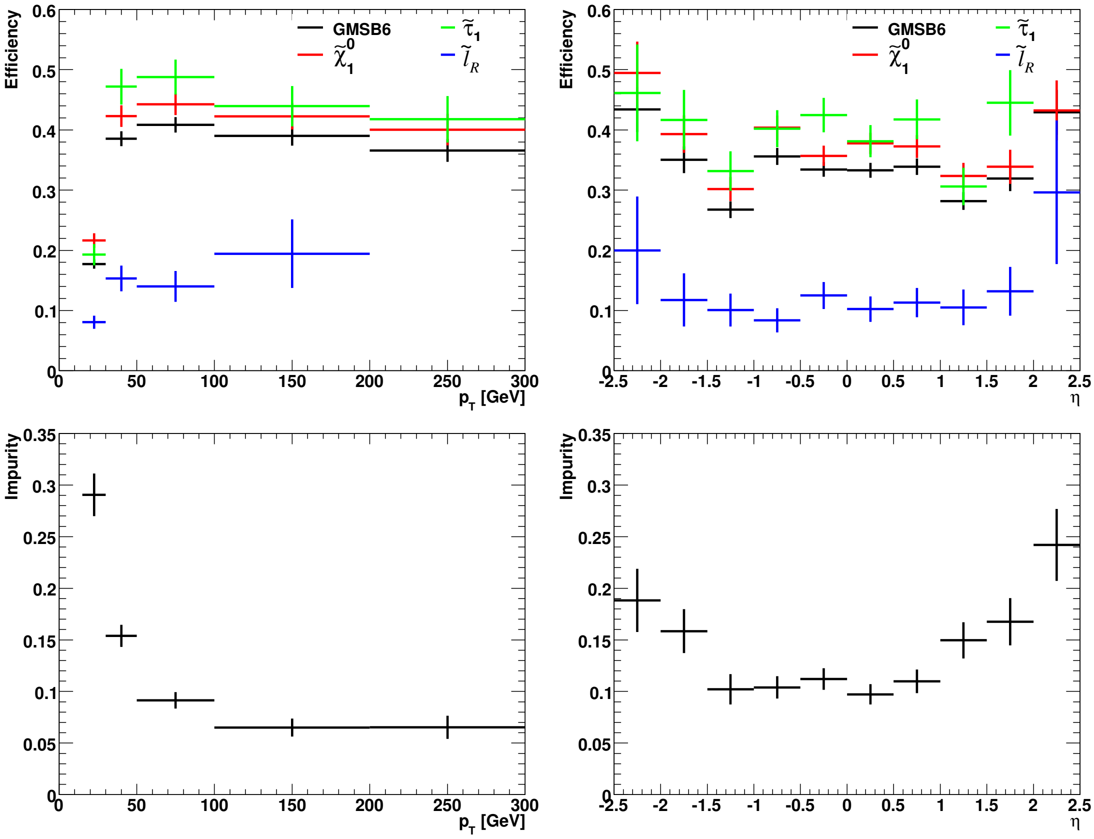

Figure 5.5: The efficiency (top) and impurity (bottom) for the reconstruction of hadronically decaying τ leptons in the GMSB6 scenario as a function of the p_T or η of the reconstructed τ lepton determined from simulated events. The efficiencies are given for τ leptons originating from different decays.

to a charge misidentification. The overall misidentification is estimated to be below 3% [18].

5.1.3 Problems of τ Reconstruction in GMSB6

In the following the efficiency of the τ reconstruction in the GMSB6 scenario is studied. The interesting decay chains can lead to final states with up to four τ leptons. Since only the hadronic decays of the τ leptons are considered here about 30% of the τ leptons, those decaying leptonically, are not reconstructed.

The efficiency is defined as the ratio of the number of reconstructed and *truth-matched* τ ($N_{\text{truthmatched}}$) over all hadronically decaying τ leptons on generator level(N_{truth}):

$$\text{efficiency} = \frac{N_{\text{truthmatched}}}{N_{\text{truth}}}. \qquad (5.5)$$

A reconstructed τ lepton is called truthmatched if a τ lepton on generator level

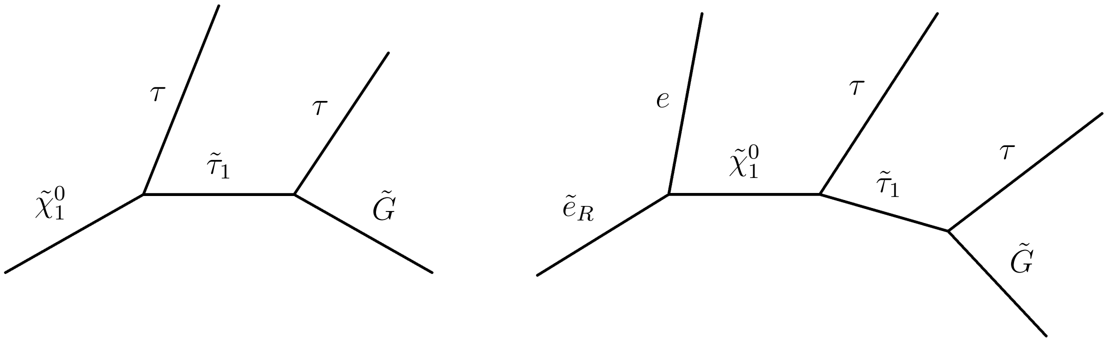

(a) $\widetilde{\chi}_1^0$-decay (b) $\widetilde{\mathrm{e}}_\mathrm{R}$-decay

Figure 5.6: The (a) neutralino and the (b) slepton decay.

is found in a cone of $\Delta R < 0.1$. Figure 5.5 (top) shows the efficiency of the reconstruction of hadronic τ decays as a function of p_T and η of the reconstructed τ leptons for the GMSB6 signal. As can be seen, the average efficiency is approximately 35%. As expected, for the low p_T range the efficiency is low and increases with p_T in a typical turn-on curve. The behavior of the efficiency in η is different. It is almost flat with minor increase for higher values of η. However most of the τ leptons are reconstructed in regions of small η.

The impurity, also shown in Fig. 5.5 (bottom) as a function of the p_T and η of the reconstructed τ, is defined as the ratio of the number of reconstructed but not truthmatched τ ($\mathrm{N}_{\mathrm{not\,truthmatched}}$) over the number of all reconstructed τ ($\mathrm{N}_{\mathrm{rec}}$):

$$\text{impurity} = \frac{\mathrm{N}_{\mathrm{not\,truthmatched}}}{\mathrm{N}_{\mathrm{rec}}}. \tag{5.6}$$

The impurity behaves complementarily to the efficiency in p_T. For low p_T where the efficiency is very low the fraction of misidentifaction is very large. The impurity as a function of η behaves in the same manner as the efficiency in η. The probability for misidentifaction is highest for particles near the beampipe.

Most striking are the large differences in the efficiency depending on the mother of the τ due to the different kinematics of these decays. The neutralino decays into a $\widetilde{\tau}$ and a τ (Fig. 5.6 (left)). Due to lepton number conservation the slepton has three decay products instead of two and along with the $\widetilde{\tau}$ and τ an additional lepton is produced .

The mass difference between the $\widetilde{\tau}$ and the neutralino is approximately 50 GeV. For sleptons it is only 20 GeV (Table A.1) often leading to a lepton lying inside the τ reconstruction cone of $\Delta R < 0.3$ illustrated in Fig. 5.7. The picture shows an event display of the ATLAS detector featuring a GMSB6 event. A τ candidate (blue) overlapping with an electron (yellow) can be seen. This electron interferes with the reconstruction of the τ lepton. The purple line indicates the direction of

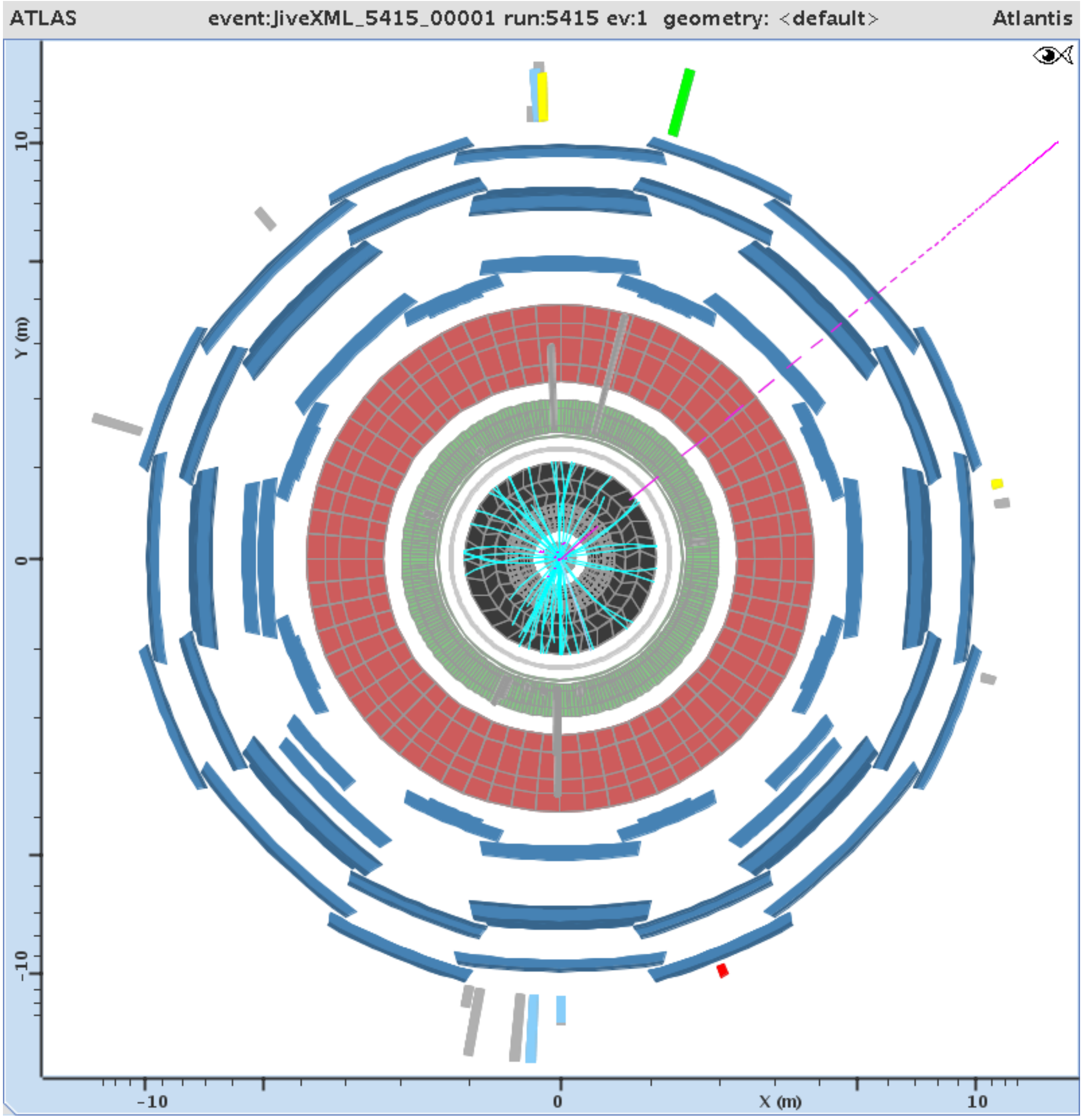

Figure 5.7: Event display of a GMSB6 event. The Inner Detector (black), the calorimeters (green, red) and the muon system (blue) of the ATLAS detector are displayed. In the transverse plane the overlap of a τ candidate (blue) with an electron (yellow) is clearly visible. The purple line indicates the direction of $\not{E}_T$.

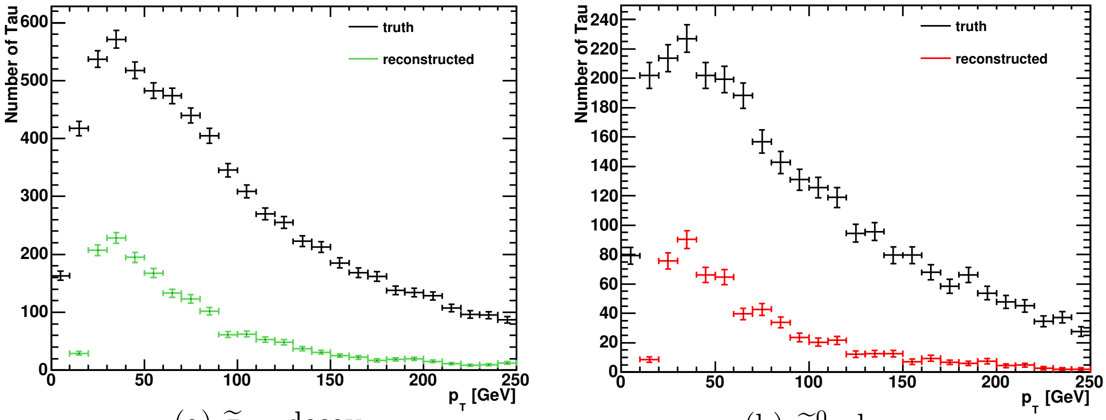

(a) $\widetilde{\tau}_1$ - decay (b) $\widetilde{\chi}_1^0$- decay

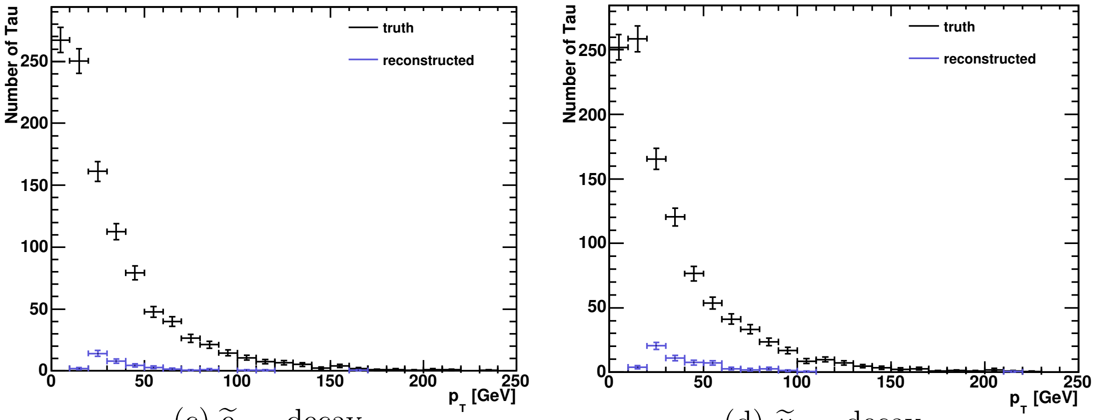

(c) $\widetilde{e}_R$ - decay (d) $\widetilde{\mu}_R$ - decay

Figure 5.8: The p_T spectrum of τ leptons originating from (a) τ decays, (b) neutralino decays, (c) right-handed selectron and (d) smuon decays. The black distributions show the true p_T spectrum whereas the colored lines show the reconstructed.

$\not{E}_T$. In addition, the event offers a photon (green), a muon (red) and several jets (grey).

The low mass difference between $\widetilde{\tau}$ and slepton leads to very different spectra in the p_T (Fig. 5.8). The black distributions show the p_T of the τ leptons on generator level whereas the colored ones illustrate the reconstructed spectra.

The p_T values for τ leptons originating from right-handed slepton decays are in general lower. The ones for τ leptons originating from neutralino and $\widetilde{\tau}$ decays have their peak at higher values and a more distinctive tail to high p_T. The reconstructed p_T spectra follow the shape of the true spectra for τ leptons from $\widetilde{\tau}$ or neutralino decays reaching the peak at 30 GeV. For slepton decays this is not visible. Since the peak of the distribution on generator level is at the lowest p_T the reconstructed spectra decrease before reaching this peak. Therefore one reason for the loss of the τ leptons during the reconstruction is the p_T treshold for the visible decay products of 15 GeV and the low reconstruction efficiency for p_T

Mother of τ	Truth	Candidate	LLH>2	Efficiency
$\widetilde{\tau}$	19900	9488	6125	46.2%
$\widetilde{\chi}_1^0$	7680	3437	2142	41.8%
$\widetilde{\mathrm{e}}_R$	2714	446	161	8.9%
$\widetilde{\mu}_R$	2773	470	220	11.9%

Table 5.2: The number of τ leptons on generator level, τ candidates, and reconstructed τ leptons in the signal sample of 9950 events and the efficiency for hadronically decaying τ leptons.

values barely exceeding this treshold.

Table 5.2 shows the number of τ leptons on generator level, of τ candidates and of reconstructed τ leptons for the different mother particles. Most of the critical τ leptons are not considered a τ candidate. The likelihood cut leads additionally to a disproportionately high loss of τ leptons originating from slepton decays.

Figure 5.9 shows the likelihood distributions of the τ candidates differing in shape depending on the mother particle. For τ candidates originating from $\widetilde{\tau}$ or neutralino decays the distributions are quite smooth. Their shape is very similar to the expected one. The distributions rise for values higher than -10 reaching the maximum above the required value of two leading to a mean likelihood close to two or above. For τ leptons originating from sleptons the maximum lies below a likelihood value of zero yielding the mean to be barely greater than zero and leading to a higher rejection of those τ candidates.

As mentioned in Sect. 5.1.1 the likelihood is built of eight variables. The distributions of these individual variables reveal more detailed the differences between the various decays. Whereas the variables for τ leptons from neutralino or $\widetilde{\tau}$ decays look very similar, the distributions for the right-handed sleptons look very different.

The electron or muon inside the τ cone changes e.g. the number of tracks inside the reconstruction cone. For neutralino decays more than half of the τ candidates have only one track (Fig. 5.10). Less than half of the τ candidates have two or three tracks. For slepton decays the fraction of τ candidates offering one track is reduced and a significant shift towards two tracks can be observed inducing the loss of one of their most significant characteristics inside the detector and therefore lowering the reconstruction efficiency. In the Inner Detector in Fig. 5.7 several tracks pointing in the direction of τ candidate are visible.

One consequence arising from a lepton lying within the τ cone is the miscalculation of the charge. As already mentioned the charge is the sum of the charges of all tracks leading to more τ candidates offering a charge that differs from one. Figure 5.11 shows that the fraction of τ candidates possessing a charge of zero or two is much higher for τ candidates from sleptons whereas the fraction of τ candidates with the charge of one is reduced compared to those from neutralinos.

The shower shape inside the calorimeter is different as well. An extra elec-

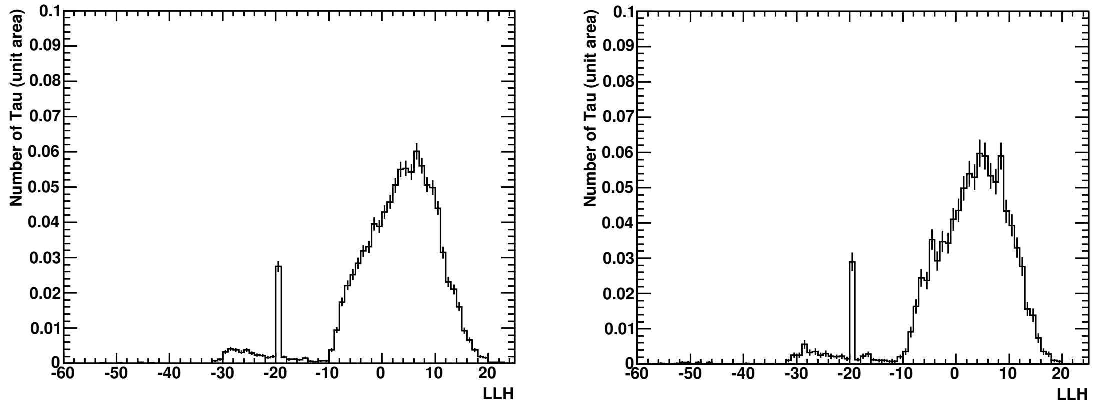

(a) $\widetilde{\tau}_1$ - decay (b) $\widetilde{\chi}_1^0$- decay

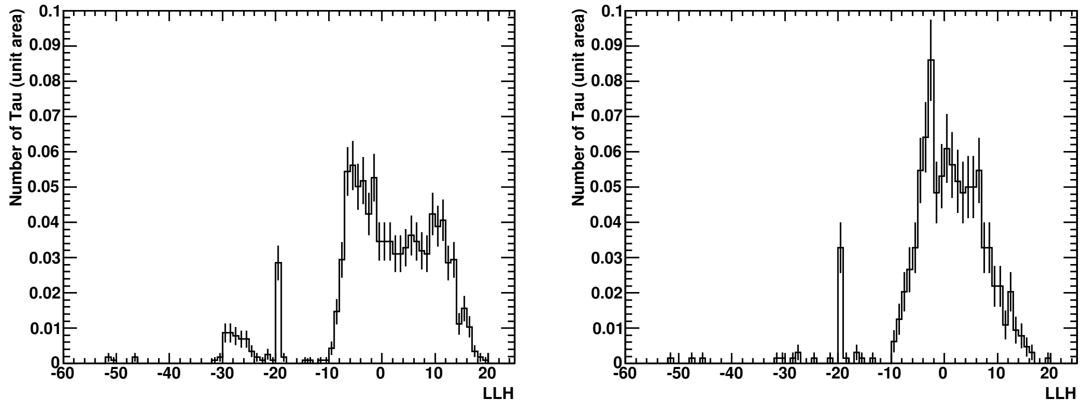

(c) $\widetilde{e}_R$ - decay (d) $\widetilde{\mu}_R$ - decay

Figure 5.9: The likelihood distributions of the different τ candidates.

tron or muon deposits additional energy in the calorimeter broadening the shower as Fig. 5.12 illustrates very plainly. Whereas for τ candidates originating from neutralinos the energy is in large part deposited in a very small cone around the cluster center, for τ candidates originating from selectrons the maximum is not as distinct and the radius in which the energy is deposited is generally larger. For smuon decays the maximum is not at the smallest radii but at $\Delta R \approx 0.1$. The energy is not as concentrated around the center of the reconstruction cone and the distribution decreases linearly instead of ending in a long tail.

All these features yield τ candidates from sleptons that look very different from those from neutralinos. In many cases they do not offer the very distinct τ characteristics such as the track multiplicity and the very narrow shower shape. The different shapes in the distributions of the individual likelihood variables lead to a lower overall likelihood resulting in a very low acceptance of these τ candidates and a reduced efficiency.

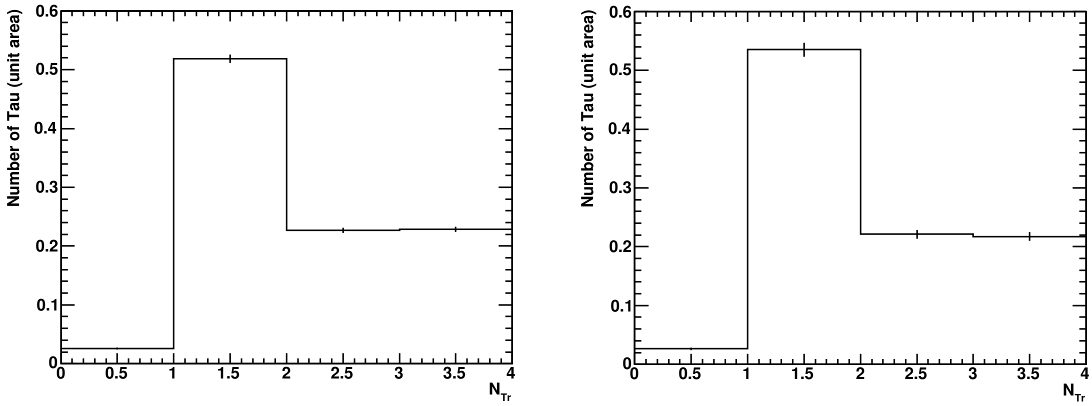

(a) $\tilde{\tau}_1$ - decay

(b) $\tilde{\chi}_1^0$- decay

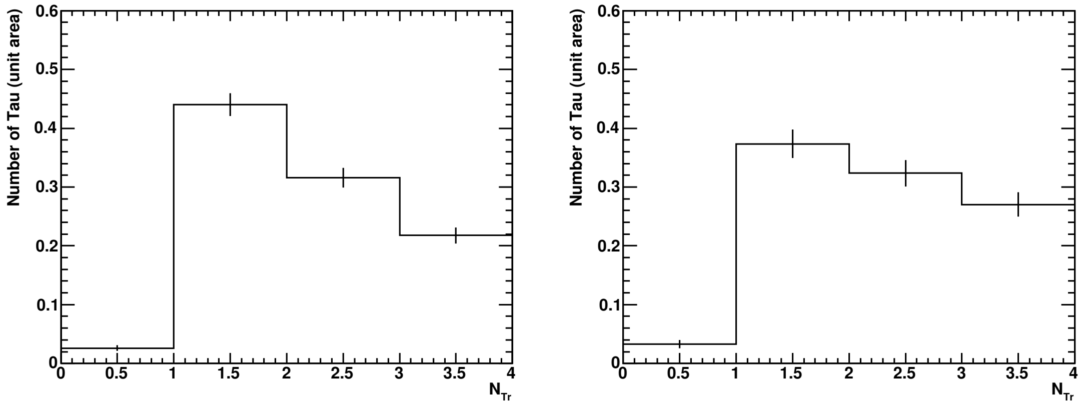

(c) $\tilde{e}_R$ - decay

(d) $\tilde{\mu}_R$ - decay

Figure 5.10: The number of tracks in the different τ candidates.

5.2 Missing Transverse Energy

An accurate determination of $\not{E}_T$ is vital for potential discovery of SUSY and the Higgs boson as well as for the measurement of semileptonically decaying $t\bar{t}$. In the following the algorithm for the $\not{E}_T$ calculation in ATLAS is presented and the expected performance is shortly discussed.

5.2.1 Calculation of Missing Transverse Energy in ATLAS

In ATLAS the $\not{E}_T$ of the final state is calculated as the vector of all calibrated calorimeter cells and reconstructed muon momenta associated with a track in the Inner Detector. The energy measured in the cells is corrected for energy loss in the cryostat (up to 5% of the $\not{E}_T$ per jet). The contribution to $\not{E}_T$ from calorimeter cells is replaced by energy measurements of other objects (e.g. tracks or muons) that can be associated to the cells. Any cell overcoming a certain noise treshold that cannot be assigned to a reconstructed object is then used for the determination

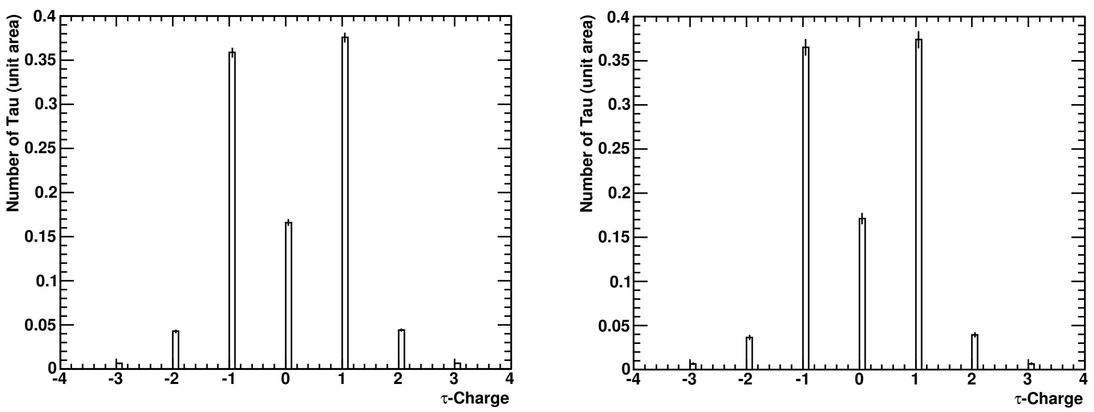

(a) $\widetilde{\tau}_1$ - decay (b) $\widetilde{\chi}_1^0$- decay

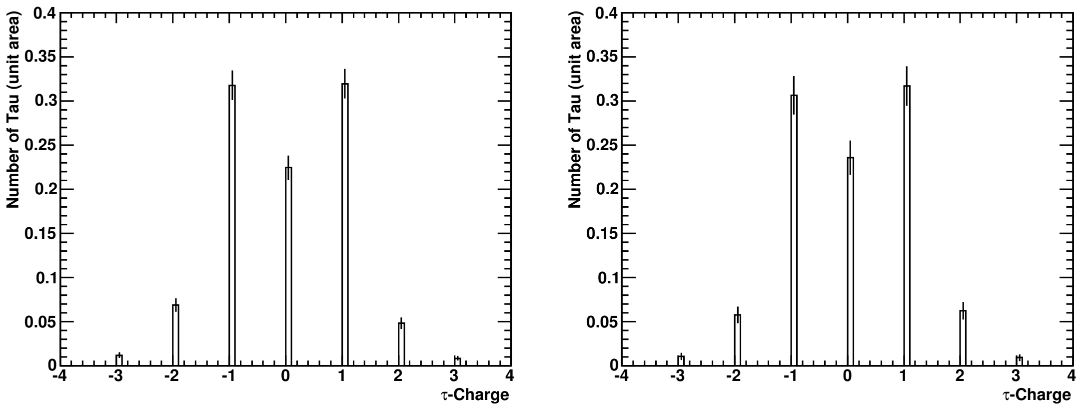

(c) $\widetilde{\mathrm{e}}_R$ - decay (d) $\widetilde{\mu}_R$ - decay

Figure 5.11: The charge of the different τ candidates.

of the $\not{E}_T$.

One of the problems is the accumulation of $\not{E}_T$ due to inaccurate energy measurements in the Inner Detector and the calorimeter making the η coverage of the forward calorimeter crucial. The weak point however are the transition regions from one component to another possibly increasing the measured $\not{E}_T$ and therefore the background from QCD multi-jets events.

5.2.2 Expected Performance

The expected performance of the reconstruction of $\not{E}_T$ is estimated through a comparison of the recontructed $\not{E}_T$ and that on generator level using simulated events. The $\not{E}_T$ reconstructed with calibrated calorimeter cells and good muons can be estimated within an uncertainty of 5% [18].

In Fig. 5.13 the expected performance of the $\not{E}_T$ direction measurement is shown for various SM processes. For W → $\mathrm{e}\nu_{\mathrm{e}}$ events containing one high p_T electron and relatively low hadronic activity a better accuracy is achieved com-

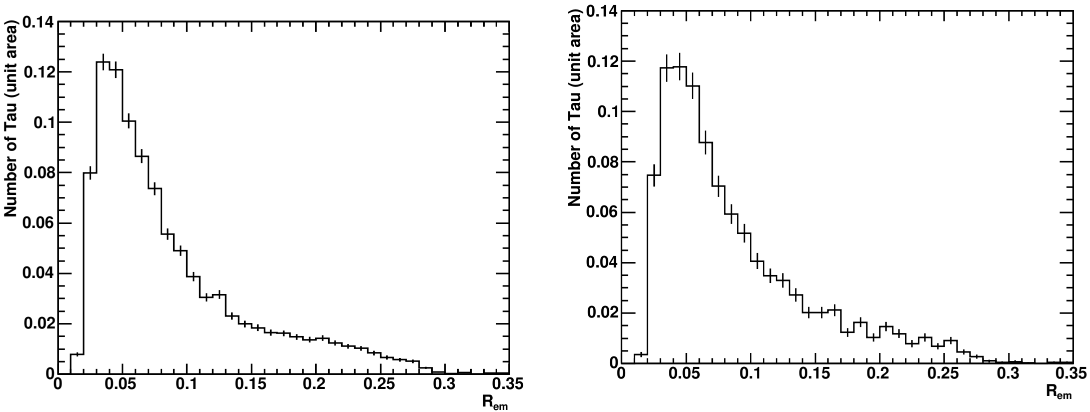

(a) $\widetilde{\tau}_1$ - decay

(b) $\widetilde{\chi}^0_1$- decay

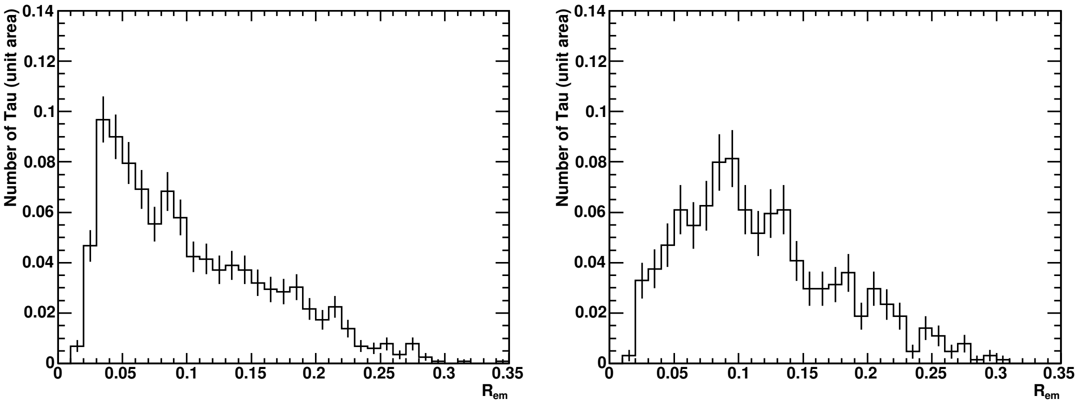

(c) $\widetilde{\mathrm{e}}_R$ - decay

(d) $\widetilde{\mu}_R$ - decay

Figure 5.12: The EM-Radius of the different τ candidates.

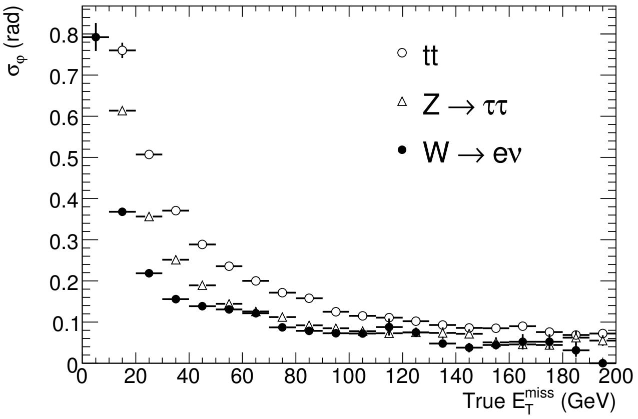

Figure 5.13: Expected uncertainty of the measurement of the polar angle of $\not{E}_T$ as a function of $\not{E}_T$ on generator level [18].

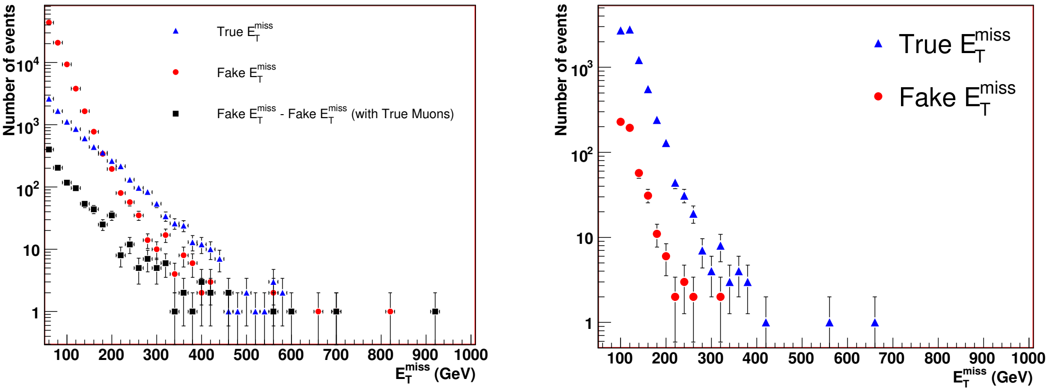

Figure 5.14: The $\not{E}_T$ on generator level and mismeasured $\not{E}_T$ for dijet events containing at least one jet with $560\,\text{GeV} < E_T < 1120\,\text{GeV}$. Either all events are taken into account (left) or only events in which the $\not{E}_T$ is isolated from high p_T jets are considered (right) [18].

pared to $t\bar{t}$ events with their busy environment. The uncertainty of this direction measurement depends highly on the $\not{E}_T$ on generator level. As expected the accuracy decreases with $\not{E}_T$. An improved direction measurement can be reached by requiring the $\not{E}_T$ vector to be isolated from all high p_T jets.

The extent of mismeasured $\not{E}_T$ is defined as the difference between the reconstructed $\not{E}_T$ and that on generator level. It can be caused by damaged calorimeter cells generating noise. Further inaccuracies arise from muons leaving the detector or from energy loss in the mentioned transition regions between the different detector components. Figure 5.14 shows the $\not{E}_T$ on generator level and mismeasured $\not{E}_T$ for dijet events containing at least one jet with $560\,\text{GeV} < E_T < 1120\,\text{GeV}$. If all events are considered the mismeasured $\not{E}_T$ exceeds the $\not{E}_T$ on generator level by far in the low $\not{E}_T$ region (left). However if the reconstructed $\not{E}_T$ is required to be isolated from the high p_T jets the mismeasured $\not{E}_T$ falls well below the $\not{E}_T$ on generator level (right).

5.3 ATLFAST vs. Full Simulation

The analysis presented studies the discovery potential of GMSB by a scan of the parameter space of Λ and $\tan\beta$ requiring a large number of simulated events. Resource limitations prohibit a full simulation of the corresponding event samples and instead events simulated with ATLFAST I are used. An appropriate ATLFAST I performance is therefore crucial for correct results.

In the following a comparison of the performance of ATLFAST I, ATLFAST II and the full simulation is presented for the variables crucial for this analysis, like the number and p_T of τ leptons and $\not{E}_T$. A standard SUSY selection includes cuts

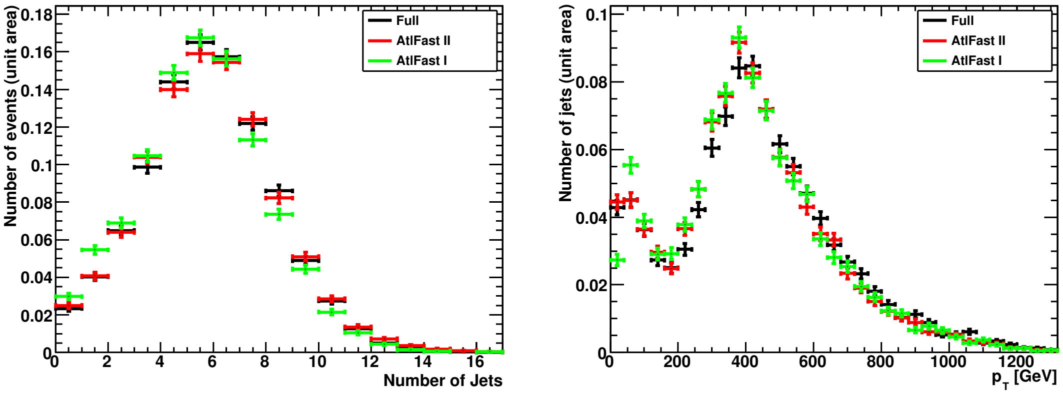

Figure 5.15: The number of jets per event (left) and the p_T of the leading jet (right) for full simulation, ATLFAST I and ATLFAST II.

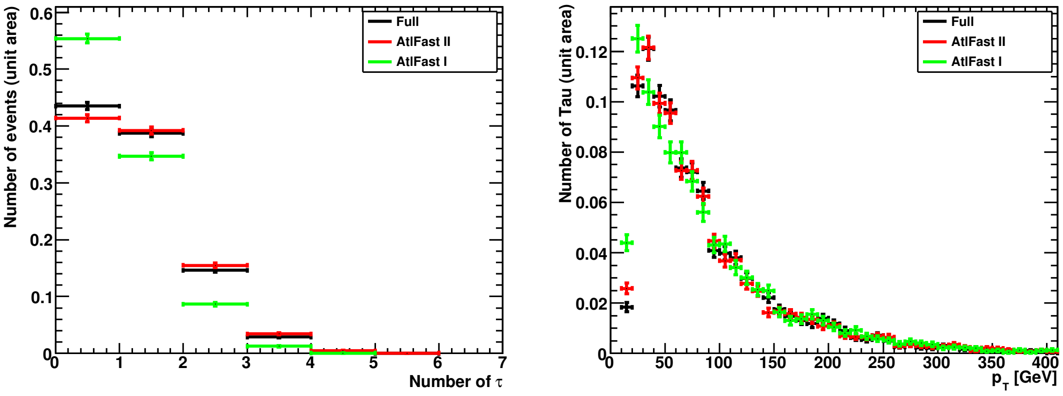

Figure 5.16: The number of τ leptons per event (left) and the p_T of the leading τ (right) for the simulation, ATLFAST I and ATLFAST II.

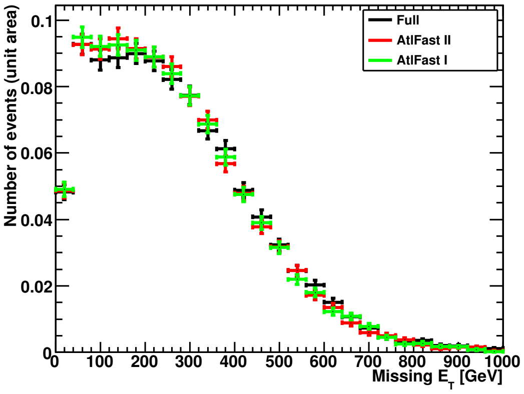

Figure 5.17: The distribution of $\not{E}_T$ for full simulation, ATLFAST I and ATLFAST II.

on the number of jets and their p_T (cf. Sect. 6.2).

Figure 5.15 shows the number of jets (left) and the p_T of the leading jet (right) for full simulation (black), ATLFAST I (green) and ATLFAST II (red). For ATLFAST I a shift towards a smaller number of jets per event resulting from different jet definitions[1] can be observed. For the p_T distribution of the leading jet only small differences can be observed. A slight shift to lower values of p_T is visible for ATLFAST I. For the p_T region up to 400 GeV ATLFAST I produces a small excess. Beyond the value of 400 GeV the full simulation exceeds the fast simulation. From 800 GeV onwards the statistic is too small for a reasonable comparison.

In Fig. 5.16 the number of τ leptons per event (left) and the p_T of the leading τ lepton is shown. Due to the above mentioned losses in the τ reconstruction the full simulation is dominated by events with no or one τ. For ATLFAST I more than half of the events do not contain any τ leptons and ATLFAST I exceeds the full simulation for those events. For at least one τ per event the distribution decreases severely below the full simulation whereas the deviation becomes bigger for a larger number of τ leptons. The reason are missing fake τ leptons in the ATLFAST I simulation. In the full simulation τ leptons can be faked by electrons and low multiplicity jets.

For the shape of the p_T of the leading τ (Fig. 5.16 (right)) an excellent agreement is observed. The total number of entries is of course smaller for ATLFAST I due to the higher number of events containing no τ leptons. Again a slight shift towards lower p_T can be observed up to $p_T = 140\,\text{GeV}$.

The $\not{E}_T$ distributions are shown in Fig. 5.17 and show sufficient agreement.

The agreement between ATLFAST II and the full simulation is expected to be better as for ATLFAST I since ATLFAST II uses in parts the full simulation and the particles are reconstructed by the same algorithms. This can be seen in the distribution of the number of jets. Since the definition of jets is the same for ATLFAST II and full simulation the distributions agree within one sigma. For the p_T of the leading jet the distributions look very similar as well. However a shift to slightly lower jet p_T just as for ATLFAST I can be observed. For the low p_T region up to 200 GeV ATLFAST II and the full simulation agree very well, whereas between 200 GeV and 400 GeV ATLFAST II results in more jets than the full simulation. Beyond the value of 400 GeV the full simulation exceeds ATLFAST II.

As in ATLFAST II the same reconstruction algorithms are used fakes occur and the agreement in the number of τ leptons is much better. Likewise the agreement in the p_T of the leading τ is very good. Until 140 GeV ATLFAST II and the full simulation agree very nicely except for the lowest p_T possible. Above this value the distributions suffer from low statistics.

The comparison of the three different simulations has demonstrated that for

---

[1] In the full simulation other objects, such as electrons or τ leptons, are often also reconstructed as jets. An overlap removal of jets and other objects has to be performed in the course of the analysis.

most of the variables a reasonable agreement can be observed. The number of τ leptons reveals the highest deviations. Since one of the requirements in the course of the study is a certain number of τ leptons more events in the ATLFAST I sample are rejected compared to the other two simulations. The number of events selected as signal and therefore e.g. the discovery potential of GMSB will be conservatively underestimated since no correction on the ATLFAST I τ variables has been performed.

Chapter 6

Study of the Discovery Potential

An analysis of the ATLAS benchmark point GMSB6 is presented in this chapter. Characteristic features, such as many high-energetic jets and a significant amount of $\not{E}_T$, are used for the separation of the signal from the SM background.

One of the goals of this study is the estimation of the discovery potential of GMSB models in the parameter space of Λ and $\tan\beta$. Since this requires simulated data for many different model points a fast simulation approach is essential.

After the performed preselection, a final event selection has to be chosen with the goal to keep as many signal events and reject as many background events as possible. To be more specific, the signal significance, defined as the ratio of the number of signal events to the square root of the number of background events, is maximized as a function of the cut values of several discriminating variables for the maximization of the discovery potential. As an example the benchmark point GMSB6 is used.

6.1 The Signal

The following decay chains are studied (cf. Sect. 2.3.1)

$$\widetilde{\chi}^0_{1,2} \to \widetilde{\tau}_1\,\tau \to \tau\,\tau\,\tilde{G} \tag{6.1}$$

$$\widetilde{\ell}_R \to \ell\,\widetilde{\tau}_1\,\tau \to \ell\,\tau\,\tau\,\tilde{G}. \tag{6.2}$$

At the benchmark point GMSB6, the production of gluinos and squarks has a cross section of 3.9 pb. The produced gluinos decay mostly into a squark-quark pair, preferably into a bottom quark and the lighter sbottom squark. The decay into a top quark and the light stop squark is kinematically forbidden (Table A.1). The branching fractions of the gluinos are:

$$\begin{aligned} \widetilde{\mathrm{g}} &\to \widetilde{q}q && 97.28\% \\ \widetilde{\mathrm{g}} &\to \widetilde{\chi}qq && 2.65\% \\ \widetilde{\mathrm{g}} &\to \widetilde{\chi}^0\mathrm{g} && 0.07\% \quad . \end{aligned}$$

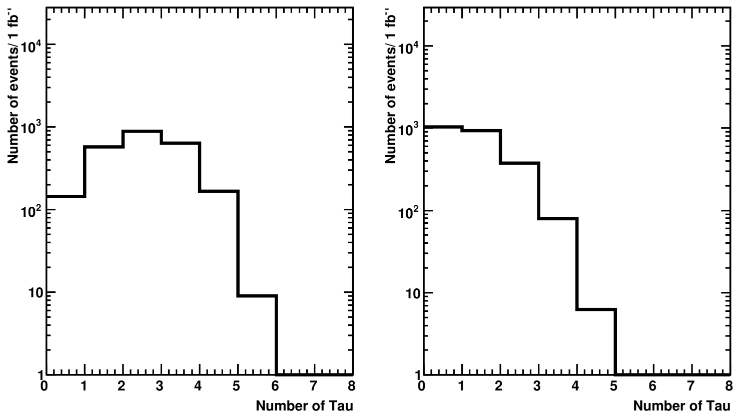

Figure 6.1: Number of τ leptons per event in the GMSB6 signal MC sample. Shown are the number of hadronically decaying τ leptons on generator level (left) and on reconstruction level including fakes (right).

For the first two generations the right-handed squark states are preferred due to their lower mass, as compared to the left-handed states. Right-handed squarks decay always into their SM partner and a neutralino whereas the left-handed states can also decay into a chargino and a quark of different flavor within the same generation

$$\begin{array}{rll} \widetilde{q}_R \rightarrow \widetilde{\chi}^0 q & \quad & 100\% \\ \widetilde{q}_L \rightarrow \widetilde{\chi}^0 q & \quad & 48 - 66\% \\ \widetilde{q}_L \rightarrow \widetilde{\chi}^{\pm} q & \quad & 34 - 52\%. \end{array}$$

The jets inititated by these quarks are very high-energetic due to the large mass difference of about 800 GeV between squarks and quarks (Fig. 2.6). The gauginos decay directly into staus, other sleptons, or into lighter gauginos predominantly via SM gauge bosons. The direct decay into the gravitino is highly suppressed.

Figure 6.1 shows the number of hadronically decaying τ leptons on generator level and the number of reconstructed τ leptons. Most signal events contain two τ leptons on generator level. A large number of events contain either one or three τ leptons. However, due the reduced efficiency of the τ reconstruction algorithm, as discussed in Sect. 5.1.3, the average number of reconstructed τ leptons per event is smaller. Most events contain either no or one reconstructed τ lepton and the number of events with four reconstructed τ leptons is insignificant.

The number of available signal MC events is 9950 corresponding to an integrated luminosity of $2.56\,\mathrm{fb}^{-1}$. In the following, all numbers and figures are normalized to an integrated luminosity of $1\,\mathrm{fb}^{-1}$.

6.2 Standard SUSY preselection

In most of the investigated SUSY scenarios many high-energetic jets are expected and a standard cut-based SUSY selection includes cuts on the number of jets, their p_T, and $\not{E}_T$. The background samples used in this study are especially produced for SUSY analyses. Therefore, during the generation already cuts on the number of jets and their p_T and $\not{E}_T$ are apllied to prevent producing a large number of events being rejected during the selection.

The SM background samples were produced with the MC generator Alpgen. A full list with all samples including the applied generator cuts, their cross section, the number of events available, and their corresponding integrated luminosity can be found in Table A.3. Each generated event has to contain at least four jets whereas the leading jet is required to fulfill $p_T > 80\,\mathrm{GeV}$. The second, third and fourth leading jet need to have $p_T > 40\,\mathrm{GeV}$. In most of the samples, each event is reqired to fulfill $\not{E}_T > 80\,\mathrm{GeV}$. $\mathrm{Z} \to \mathrm{ee}$ and $\mathrm{Z} \to \mu\mu$ events are required to contain a Z boson with a p_T of at least 80 GeV.

The reconstructed τ leptons in the background samples can either originate from true τ leptons in decays of W bosons, Z bosons, or top quarks or arise from jets reconstructed as τ leptons occuring in QCD background. The multijet background also contributes to $\not{E}_T$ through mismeasured high-energetic jets.

Top quarks decay into a bottom quark and a W boson. They are predominantly produced in pairs. In $\mathrm{t\bar{t}}$ events, either both W bosons decay into quarks (hadronic), one decays instead into leptons (semileptonic), or both decay into leptons (leptonic). These types of events constitute relevant background signatures such as multiple jets, true $\not{E}_T$ in (semi)leptonic events from the neutrinos and up to two true τ leptons. The considered samples include $\mathrm{t\bar{t}}$ and zero to three additional jets.

Events with a single W boson might contain one true τ lepton and true $\not{E}_T$. Samples of events with leptonically decaying W bosons with two to five additional jets are studied.

Events containing Z bosons decaying into two τ leptons can also contribute to the background of up to two true τ leptons. If the leptons are misidentified it displays a background with up to two jets. Z bosons decaying into two neutrinos contribute to the background with true $\not{E}_T$. In addition also $\mathrm{Z} \to \mathrm{ee}$ and $\mathrm{Z} \to \mu\mu$ are considered. Samples of Z events with one to five additional jets are taken into account.

Multijet samples include three to six light quark jets. They are the dominant background concerning misidentified τ leptons and mismeasured $\not{E}_T$. Also $\mathrm{b\bar{b}}$ samples with two or three additional jets are considered as a possible background source.

For a discovery the reduction of the SM background with respect to the signal is of highest priority. Figure 6.2 shows the number of jets for all mentioned background samples and for the signal MC events. At this stage τ leptons are counted as jets. The distributions of the variables are shown after the already mentioned

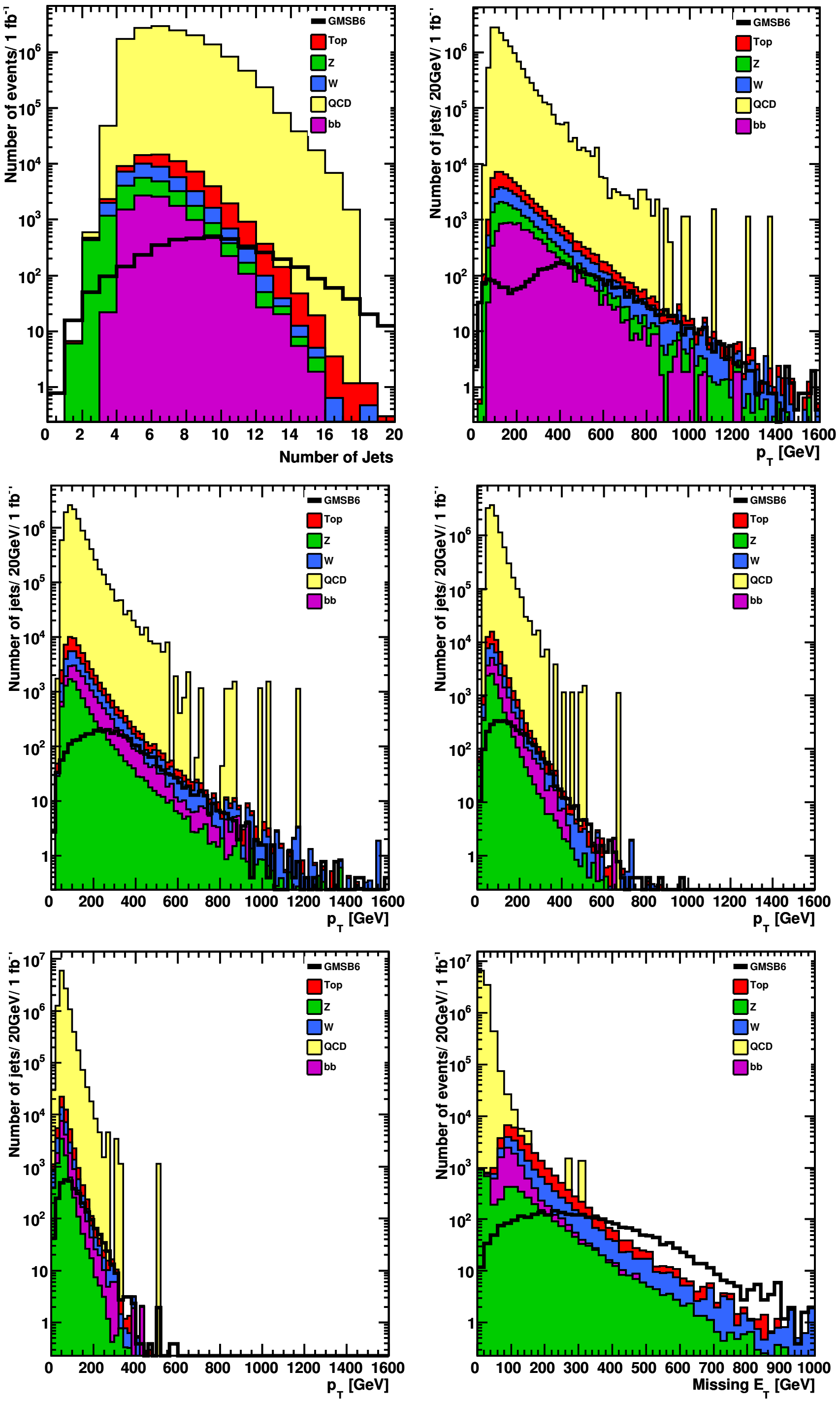

Figure 6.2: Event distribution of variables used in the event preselection. Shown are the number of jets per event before any cuts (top left) and the p_T for the leading jet (top right), the second leading jet (middle left), the third leading jet (middle right), and the fourth leading jet (bottom left) and the $\not{E}_T$ after the cuts on the jets (bottom right).

cut but before the following cuts. The dominance of the QCD samples is clearly visible. The background distribution shows a peak at five or six jets. The signal distribution peaks at nine jets per event. Therefore, the first selection cut is

$$N_{\text{jets}} \geq 4\,. \tag{6.3}$$

The jets within the signal are expected to be very high-energetic. The next requirement is therefore that the p_T of the jets exceed a certain threshold. Figure 6.2 (top right) shows the p_T distribution for the leading jet. Most jets of the background have a p_T of $100-200\,\text{GeV}$. The jet p_T distributions for all considered background are steeply falling at higher p_T. A significant fraction of jets in the signal also have a p_T in this range but the peak of the distribution is shifted towards higher values and is located at about 400 GeV. Thus the leading jet should fulfill

$$p_T > 100\,\text{GeV}\,. \tag{6.4}$$

Figure 6.2 (middle row and bottom left) shows likewise the p_T for the second, third, and fourth leading jet. The slope towards higher values is steeper for every distribution and the truncation of the distribution occurs at lower values. The signal distributions behave in the same manner. The second, third, and fourth leading jet needs to fulfill

$$p_T > 50\,\text{GeV}\,. \tag{6.5}$$

The multijet background is still highly dominant but offers only limited statistics which can be seen since the p_T distributions do not decrease smoothly as the other background samples but are rather interrupted. These detached peaks are due to single events with a large event weight.

The last requirement concerns $\not{E}_T$ shown in Fig. 6.2 (bottom right). The multijet background does not contain a large amount of $\not{E}_T$. The events are very concentrated below a value of 200 GeV because no generator cut was applied on the $\not{E}_T$. Most of the events of all other background samples offer more $\not{E}_T$ and a smooth tail to very high $\not{E}_T$. The signal contains evenly distributed $\not{E}_T$ and exceeds the background for values higher than 400 GeV. Requiring

$$\not{E}_T > 100\,\text{GeV} \tag{6.6}$$

rejects a great amount of the QCD background.

The number of signal and background events are listed in Table 6.2, separately for each individual background and for each individual applied preselection cut. Obviously, the multijet samples are the dominant source of background events. This is expected at a proton-proton-collider because of the high inelastic proton-proton-scattering cross section.

The cuts and their specific values were chosen to accomodate for the generator cuts and in addition to consider resolution effects as well as reconstruction inefficiencies. Therefore, the first requirement of four jets is not very severe for the background as can be seen in Table 6.2 and Fig. 6.3. However, the requirement on

	No Cuts	# Jet ≥ 4	1^{st} Jet p_T $> 100\,\mathrm{GeV}$	2^{nd} Jet p_T $> 50\,\mathrm{GeV}$	3^{rd} Jet p_T $> 50\,\mathrm{GeV}$	4^{th} Jet p_T $> 50\,\mathrm{GeV}$	$\not{E}_T$ $> 100\,\mathrm{GeV}$
Signal	3899	3736	3460	3395	3191	2679	2424
All BG	15.1M	15.0M	11.7M	11.6M	10.5M	7.1M	33126
$\mathrm{t}\,\bar{\mathrm{t}}$	26161	25797	22316	22064	20055	13697	9408
$\mathrm{t\bar{t}} \rightarrow \ell\nu\ell\nu$	4141	3955	3434	3382	2958	1818	1334
$\mathrm{t\bar{t}} \rightarrow \ell\nu qq$	21677	21500	18548	18347	16767	11586	7948
$\mathrm{t\bar{t}} \rightarrow qqqq$	342	341	334	334	329	292	125
Z	12254	10655	9273	9090	7754	4407	1961
$\mathrm{Z} \rightarrow \mathrm{ee}$	6440	4910	4030	3895	3075	1509	3
$\mathrm{Z} \rightarrow \mu\mu$	738	732	666	661	595	361	44
$\mathrm{Z} \rightarrow \tau\tau$	725	705	660	652	587	370	221
$\mathrm{Z} \rightarrow \nu\nu$	4349	4306	3916	3881	3496	2166	1690
W	17610	16795	15368	15182	13396	7996	5523
$\mathrm{W} \rightarrow \mathrm{e}\nu_{\mathrm{e}}$	6950	6320	5738	5637	4768	2578	1724
$\mathrm{W} \rightarrow \mu\nu_{\mu}$	3407	3369	3116	3094	2816	1782	1221
$\mathrm{W} \rightarrow \tau\nu_{\tau}$	7253	7105	6513	6451	5812	3636	2577
Multijets	14996120	14950126	11651780	11526710	10475694	7075388	13246
3 jets	167007	162053	114989	112061	84100	29083	0
4 jets	7447311	7406271	5287391	5194671	4475711	2224914	3039
5 jets	1876875	1876875	1499247	1487986	1381380	993993	1126
6 jets	5504926	5504926	4750151	4731991	4534501	3827396	9080
$\mathrm{b}\,\bar{\mathrm{b}}$	10406	10385	10012	9989	9550	6858	2988
+ 2 jets	6681	6659	6400	6377	6014	3853	1608
+ 3 jets	3725	3725	3612	3612	3535	3004	1380

Table 6.1: Cut flow table for signal and background events for preselection cuts. All numbers are normalized to an integrated luminosity of $1\,\mathrm{fb}^{-1}$.

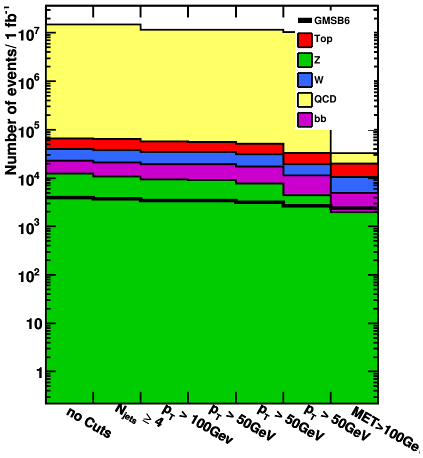

Figure 6.3: The cut flow for the preselection cuts illustrates the power of $\not{E}_T$ for reducing the SM background.

the p_T of the leading jet to be above 100 GeV reduces the background noticeably whereas the signal is only reduced by 10% even though no demands were made during the event generation. After the requirement for the fourth jet the signal and the background are reduced to 2679 and $7.1 \cdot 10^6$ events respectively. For the signal, this corresponds to a selection efficiency of 69 %.

The most important requirement is the $\not{E}_T$ cut significantly reducing the QCD background. The resulting number of events is 2424 for the signal and 33126 for the background. 62 % of the signal events were selected whereas the background could be reduced such that the number of background events is only one order of magnitude larger than the number of signal events. The next step is to find a set of cuts more specific for GMSB models in order to further reduce the SM background.

6.3 Optimized Final Selection

The most obvious variables to use for the distinction of signal from background are $\not{E}_T$, the number of τ leptons, and their p_T. In Fig. 6.4 showing the $\not{E}_T$ and the number of τ leptons after preselection (cf. Sect. 6.2), it can be seen that the signal dominates the background in regions of large $\not{E}_T$ and many τ leptons per event.

Figure 6.5 shows the p_T of the leading and the second leading τ lepton. Although both signal distributions have larger tails towards high p_T, both the signal and the background distributions have their maximum at rather low p_T. Thus, the signal-background separation of these two variables is rather limited.

To optimize cuts in either $\not{E}_T$ or the number of τ leptons the signal significance

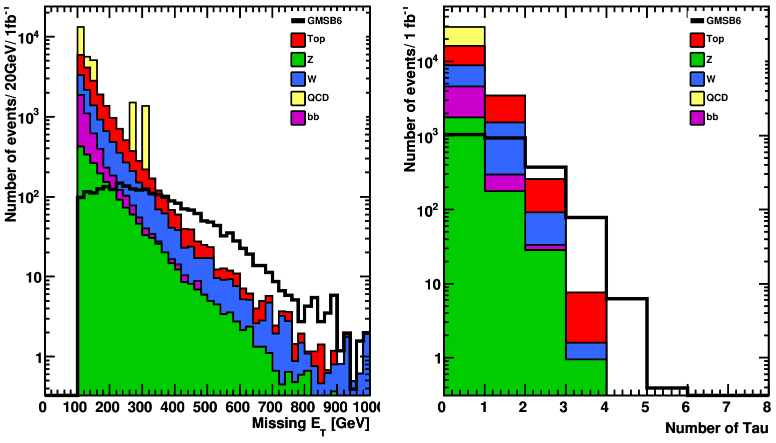

Figure 6.4: Distributions of $\not{E}_T$ (left) and the number of τ leptons per event (right) for signal and background events after preselection.

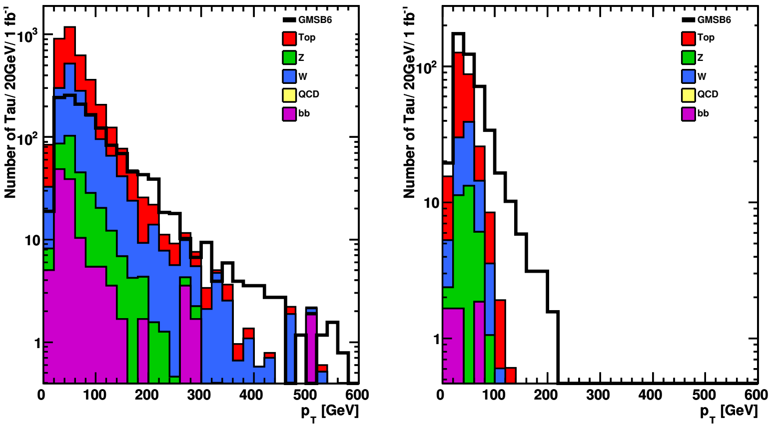

Figure 6.5: The p_T of the leading (left) and the second leading τ lepton (right) in the event.

S, defined as

$$\mathrm{S} = \frac{\#\,\mathrm{Signal\ events}}{\sqrt{\#\,\mathrm{BG\ events}}}, \tag{6.7}$$

is maximized as a function of the cuts on $\not{E}_T$ and the number of τ leptons. Due to the weighting of events, the number of background events can be smaller than one. In this case, always one background event is assumed and the signal significance is equal to the number of events.

Figure 6.6 (left) shows the signal significance as a function of the cut value of $\not{E}_T$ with no requirement set on the number of τ leptons. As expected, the signal significance rises from high cut values of $\not{E}_T$ to smaller values as long as the number of signal events is larger than the number of background events. As soon as this ratio inverts, the signal significance decreases. The highest signal significance is almost 40 so that a discovery is feasible.

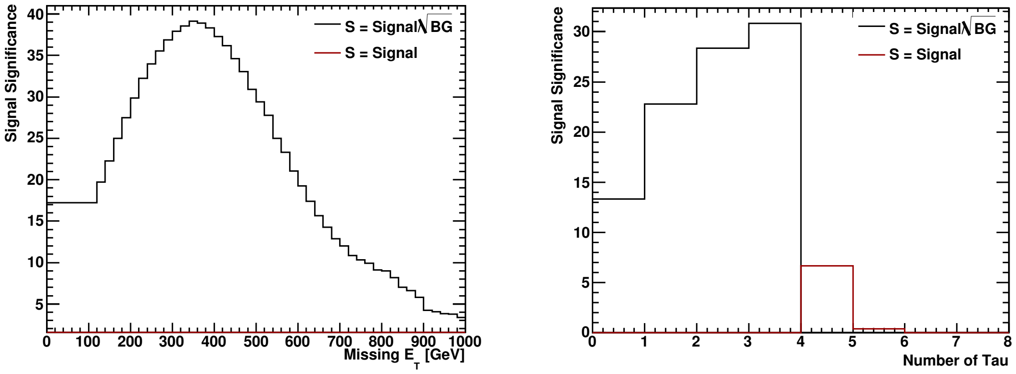

Figure 6.6: Evolution of the signal significance as a function of different cut values of $\not\!\!E_T$ (left) and the number of τ leptons (right).

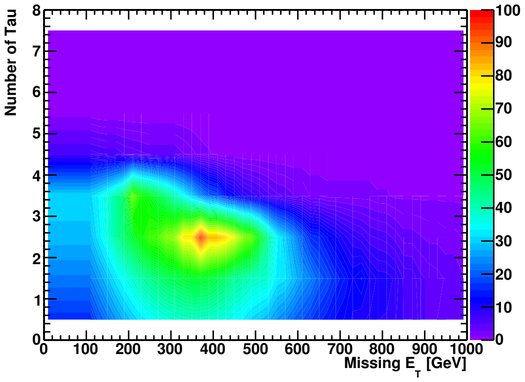

Figure 6.7: The signal significanceas a function of the cut values of $\not\!\!E_T$ and the number of τ leptons.

The signal significance as a function of the cut value of the number of τ leptons with no requirement set on the $\not\!\!E_T$ is shown as well in Fig. 6.6 (right). For three τ leptons the signal significance is highest with a value of about 30, but decreases slightly for events with two τ leptons, even though the number of signal events still exceeds the number of background events. For events with only one or no τ leptons the background contributes much more events than the signal and the significance decreases further.

The signal significance was also studied as a function of the τ p_T. It rises very slowly from higher to lower cut values of the τ p_T and adopts its highest value if no requirement is set on the τ p_T. Therefore no cuts on the p_T of the τ leptons is applied in the following.

Using one of the variables alone, the best discovery potential is given for either $\not\!\!E_T > 360\,\mathrm{GeV}$ or $N_\tau \geq 3$. Combining both variables should either increase the discovery potential or allow to losen the cuts for the same signal significance. The signal significance as a function of the cuts on $\not\!\!E_T$ and the number of τ leptons is shown in Fig. 6.7. The highest signal significance is found for $\not\!\!E_T > 360\,\mathrm{GeV}$ and

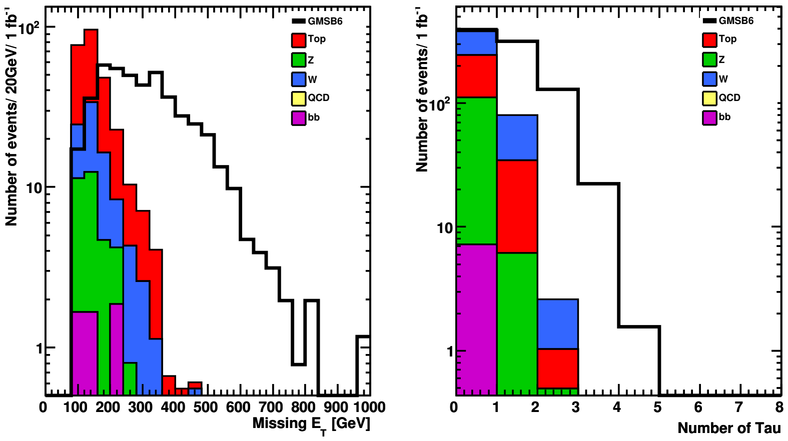

Figure 6.8: Distribution of $\not{E}_T$ after the requirement of two τ leptons (left) and the number of τ leptons after the requirement of $\not{E}_T > 360\,\mathrm{GeV}$.

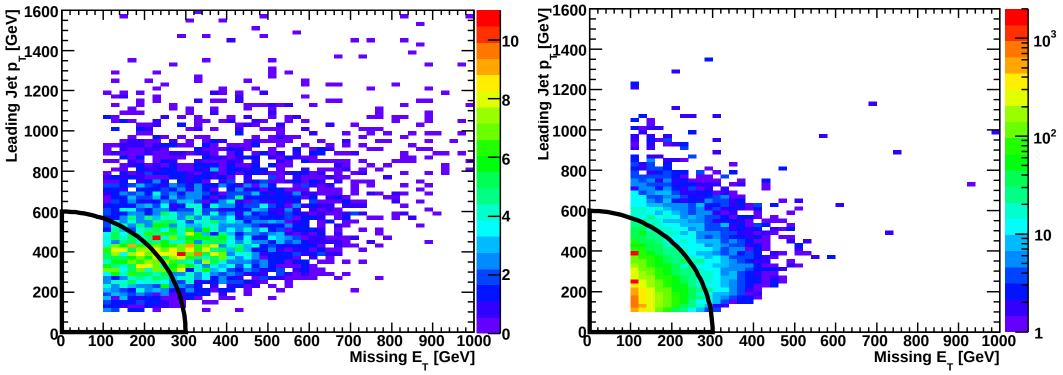

(a) Signal

(b) Background

Figure 6.9: The correlation between $\not{E}_T$ and p_T of the leading jet for (a) the signal and (b) the background. The indicated elliptical cut in this plane rejects most of the background.

two or more τ leptons. For this optimized selection, we find 153 signal events with a background of 2.6 events yielding a significance of about 95 which represents a large improvement compared to the optimization of a single variable (cf. Fig. 6.6).

Figure 6.8 shows the $\not{E}_T$ distribution with the additional requirement of two or more τ leptons. In addition, the number of τ leptons with the applied cut on $\not{E}_T > 360\,\mathrm{GeV}$ is shown. As expected in each case applying the cut on the other variable rejects most of the background events.

In Fig. 6.7 a rather wide region of high significance is visible around the maximum. Therefore slightly losening the rigid cut on $\not{E}_T > 360\,\mathrm{GeV}$ will still yield a high discovery potential. As an alternative the correlation between $\not{E}_T$ and the p_T of the leading jet is exploited since signal events are expected to contain more high p_T jets than background events. Figure 6.9 shows that for the background

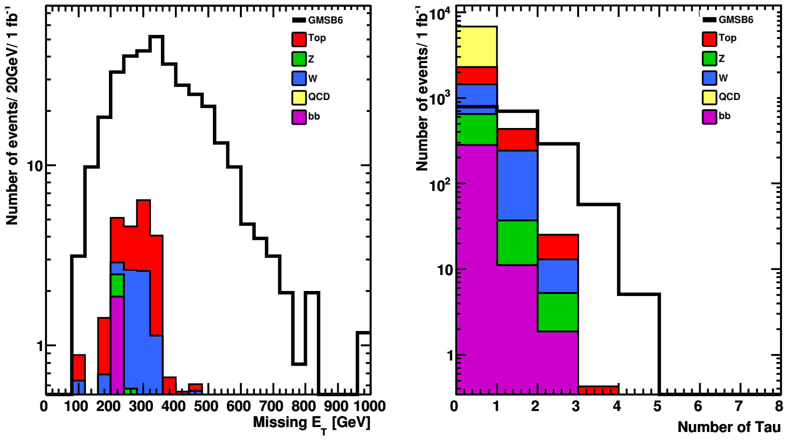

Figure 6.10: Distribution of the $\not\!\!E_T$ requiring two or more τ leptons after the application of the elliptical cut(left). The number of τ leptons after the application of the elliptical cut (right).

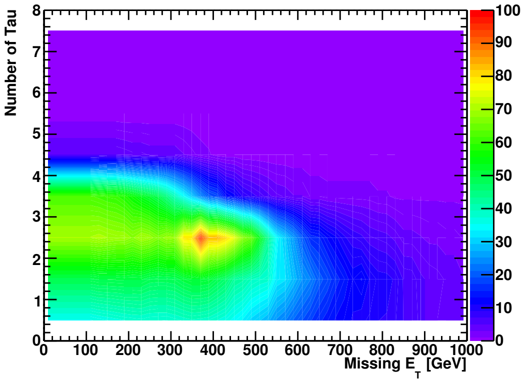

Figure 6.11: The significance in the two-dimensional plane of $\not\!\!E_T$ and the number of τ leptons after the eliptical cut is applied.

the events are concentrated in regions of low $\not\!\!E_T$ and low p_T. The signal events provide higher values in both variables. Applying an elliptical cut in this plane

$$\left(\frac{\not\!\!E_T}{300\,\mathrm{GeV}}\right)^2 + \left(\frac{p_{T,\mathrm{jet1}}}{600\,\mathrm{GeV}}\right)^2 > 1, \tag{6.8}$$

rejects most of the background events and keeps more signal events than simply cutting hard on $\not\!\!E_T$ alone. Figure 6.10 (left) shows the $\not\!\!E_T$ distribution for signal and background events after the application of the elliptical cut and additionally requiring two τ leptons. Most of the background events are rejected whereas the number of signal events is only slightly reduced. In addition the number of τ leptons is shown (right) after the application of the elliptical cut. Requiring two τ leptons rejects a great fraction of the background events. However, an essential premise for such an elliptical cut is a good understanding of the background since

	$\not{E}_T > 100\,\mathrm{GeV}$	$\#Tau \geq 2$	Elliptical Cut	$\not{E}_T > 360\,\mathrm{GeV}$
Signal	2424	463.30	352.76	153.26
All BG	33126	267.21	25.48	2.60
$\mathrm{t\bar{t}}$	9408	173.82	12.46	0.53
$\mathrm{t\bar{t}} \rightarrow \ell\nu\ell\nu$	1334	44.37	4.44	0.53
$\mathrm{t\bar{t}} \rightarrow \ell\nu qq$	7948	128.66	7.96	0.00
$\mathrm{t\bar{t}} \rightarrow qqqq$	125	0.80	0.05	0.00
Z	1961	29.31	3.40	0.50
$\mathrm{Z} \rightarrow \mathrm{ee}$	3	0.36	0.17	0.00
$\mathrm{Z} \rightarrow \mu\mu$	44	0.32	0.12	0.12
$\mathrm{Z} \rightarrow \tau\tau$	221	26.20	2.72	0.23
$\mathrm{Z} \rightarrow \nu\nu$	1690	2.44	0.39	0.15
W	5523	58.88	7.76	1.57
$\mathrm{W} \rightarrow \mathrm{e}\nu_{\mathrm{e}}$	1724	17.71	2.47	0.81
$\mathrm{W} \rightarrow \mu\nu_{\mu}$	1221	0.99	0.00	0.00
$\mathrm{W} \rightarrow \tau\nu_{\tau}$	2577	40.17	5.29	0.77
Multijets	13246	0.00	0.00	0.00
3 Jets	0	0.00	0.00	0.00
4 Jets	3039	0.00	0.00	0.00
5 Jets	1126	0.00	0.00	0.00
6 Jets	9080	0.00	0.00	0.00
$\mathrm{b\bar{b}}$	2988	5.20	1.86	0.00
+ 2 Jets	1608	3.34	0.00	0.00
+ 3 Jets	1380	1.86	1.86	0.00

Table 6.2: Cut flow table for the signal and background for the final selection cuts. All numbers are normalized to an integrated luminosity of $1\,\mathrm{fb}^{-1}$.

less background events than for a hard cut on $\not{E}_T$ are rejected.

Although the elliptical cut rejects most of the background events, the two-dimensional signal significance scan still finds the same combination of cuts for the highest significance, as shown in Fig. 6.11. However, the shape changed and the range in which the significance exceeds values of fifty or higher is larger. If only two τ leptons are required and no further cut on the $\not{E}_T$ is applied the number of signal and background events is 353 and 25 respectively leading to S≈70.

Table 6.2 summarizes the number of signal and all background events after each of the mentioned cuts. After the requirement of two τ leptons the number of signal events exceeds the number of background events. The selection efficiency for signal and background is 19% and 0.81% compared to the preselection. Even though the signal is further reduced to 6.3% of the preselection by $\not{E}_T > 360\,\mathrm{GeV}$ this cut will be used to determine the discovery potential since it yields the highest significance.

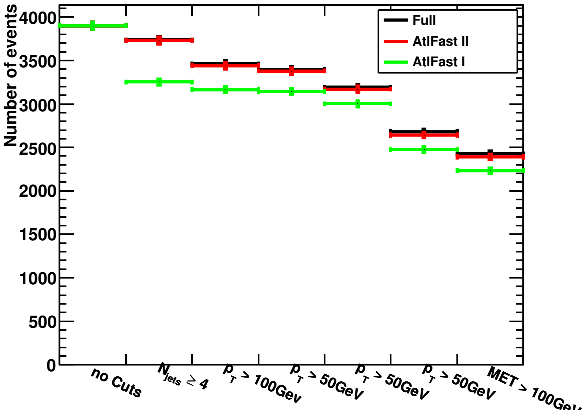

Figure 6.12: The cut flow of the preselection and selection cuts on the full simulation sample of GMSB6 in comparison to fast simulation.

The elliptical cut in the $\not{E}_T$ versus leading jet p_T plane will be used for the study of the invariant mass distribution presented in Ch. 7 because it allows to keep more than twice the signal events with a moderate increase in the number of background events only.

6.4 Selection Cuts on the ATLFAST Samples

The study presented so far was done using a GMSB6 data sample produced with full simulation. As mentioned above for a scan of the parameter space, data for many different model points are necessary. In Sect. 5.3 a comparison of full and fast simulation for variables crucial for this analysis is presented. The main difference is found in the number of τ leptons per event. Since this is one of the cut variables the ATLFAST I data samples are expected to be affected differently by the cuts than the full simluation sample.

Figure 6.12 shows the cut flow for the preselection cuts for full and fast simulation. As expected, ATLFAST II and full simulation provide almost identical results. For ATLFAST I a shift to lower values in the number of jets is observed leading to a larger rejection due to the first peselection cut requiring four jets per event (cf. Sect. 6.2). For the cuts on the p_T of the first, second and the third leading jet less ATLFAST I events are rejected compared to the other two simulations. The p_T cut on the fourth leading jet leads to the highest relative rejection for all three simulation approaches. After the $\not{E}_T$ cut the number of ATLFAST I events is approximately eight percent smaller than for the full simulation whereas the deviation in ATLFAST II is only 1.5%.

Table 6.4 summarizes the number of events for the full simulation in comparison to the two fast simulation approaches for the preselection as well as for the final selection. After the preselection the differences of the three approaches is relatively

Cuts	Full	ATLFAST II	ATLFAST I
No Cuts	3899	3899	3899
# Jet	3736	3730	3251
1^{st} Jet p_T	3460	3440	3164
2^{nd} Jet p_T	3395	3379	3142
3^{rd} Jet p_T	3191	3169	3001
4^{th} Jet p_T	2679	2641	2473
$\not{E}_T > 100\,\mathrm{GeV}$	2424	2390	2233
# Tau	463	494	252
elliptical Cut	353	352	186
$\not{E}_T > 360\,\mathrm{GeV}$	178	165	93

Table 6.3: The cut flow shows that ATLFAST II is much more compatible with the full simulation as Atlfast I.

small. However, requiring at least two τ leptons, leads to a rejection of more ATLFAST I events than full simulation events, as expected from the discussion in Sect. 5.3. The number of events is twice as big in the full simulation and ATLFAST II than in ATLFAST I. The relative rejection due to the other two selection cuts is approximately the same for all three simulations.

The discovery potential will be underestimated in this study since no correction on the number of τ leptons in the ATLFAST I data has been performed. This is maintable as long as only the number of the τ leptons is of interest. As soon as a quantity of the τ leptons, e.g. their p_T, is relevant a correction is essential. For a more precise conclusion ATLFAST II would be a noteworthy alternative since for the elliptical cut ATLFAST II offers almost the same number of events and for the cut on $\not{E}_T > 360\,\mathrm{GeV}$ the deviation is less than eight percent. Due to time reasons in this thesis only ATLFAST I could be used for the estimation of the discovery potential.

6.5 Scan of the Parameter Space

For the determination of the discovery potential, ATLFAST I data samples were produced in the parameter space of Λ from 10 TeV to 100 TeV in steps of 5 TeV and $\tan\beta$ from 2 to 34 in steps of 1. In addition to the preselection (cf. Sect. 6.2) the following cuts

$$\mathrm{N}_\tau \geq 2 \qquad \text{and} \qquad \not{E}_\mathrm{T} \geq 360\,\mathrm{GeV}$$

are applied. Since the number of background events is independent from SUSY parameters the signal significance as a function of Λ and $\tan\beta$ can be determined using the number of background events from full simulation $N_{\mathrm{BG}} = 2.6$. Figure 6.13 shows the signal significance for an integrated luminosity of $100\,\mathrm{pb}^{-1}$, $1\,\mathrm{fb}^{-1}$, $10\,\mathrm{fb}^{-1}$ and $100\,\mathrm{fb}^{-1}$. It can bee seen that even with a small amount of

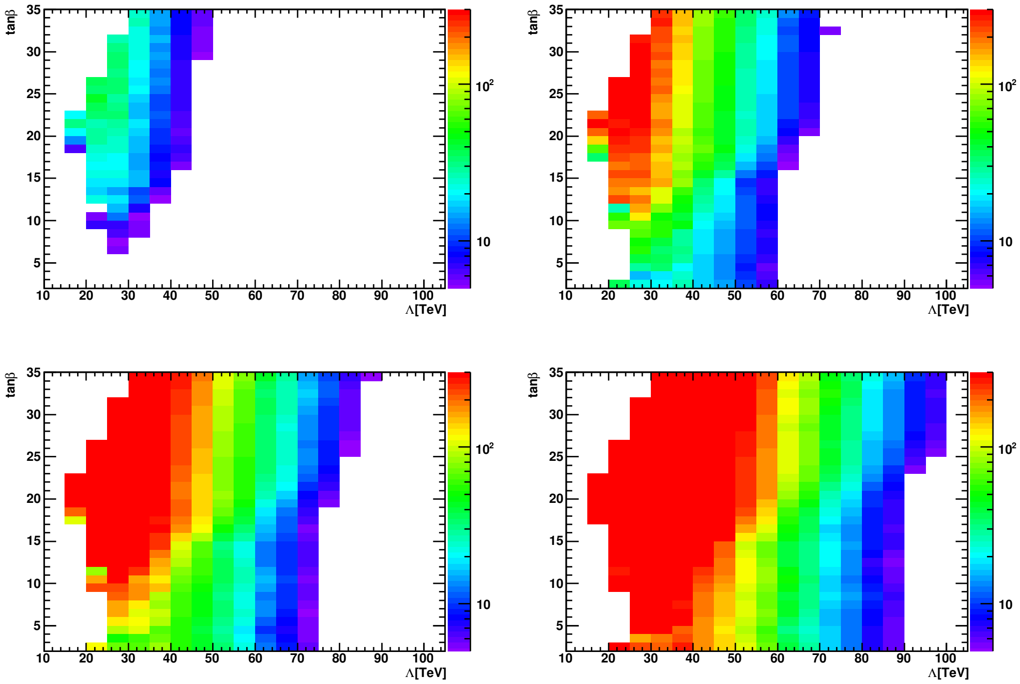

Figure 6.13: The signal significance in the GMSB parameter space for an integrated luminosity of 100 pb^{-1} (upper left), 1 fb^{-1} (upper right), 10 fb^{-1} (bottom left) and 100 fb^{-1} (bottom right).

data the cuts are able to isolate the signal effectively. Thus a discovery is feasible in a wide range of the parameter space. With 1 fb^{-1} it is possible to cover the parameter space up to $\Lambda \approx 60$ TeV independent from $\tan\beta$[1]. The signal significance decreases as a function of Λ due to the linear dependence of the SUSY masses on Λ. As result the cross section decreases with rising Λ which can be clearly seen in Fig. 6.14. The dependence of the cross section on $\tan\beta$ is negligible. The region of small Λ and large $\tan\beta$ is theoretically inaccessible.

In addition, the signal significance increases with $\tan\beta$ values since in this region the $\widetilde{\tau}$ is the sole NLSP (cf. Fig. 2.7). For lower values of $\tan\beta$ however, the $\widetilde{\tau}$ does not occur in every decay chain because the NLSP is the marginally lighter right-handed selectron or smuon. Therefore the occurence of two τ leptons is less likely and more events will be rejected leading to a decrease of the significance. For small Λ the NLSP is the lightest neutralino. In this region the sensitivity is zero.

Figure 6.15 shows the lines of integrated luminosity that are necessary for a 5σ discovery of the different GMSB model points. In this plot the same features can be seen as in Fig. 6.13.

---

[1] The lower integrated luminosity can be achieved relatively fast during the startup phase of the LHC whereas collecting 1 fb^{-1} will take several months of continuous data taking.

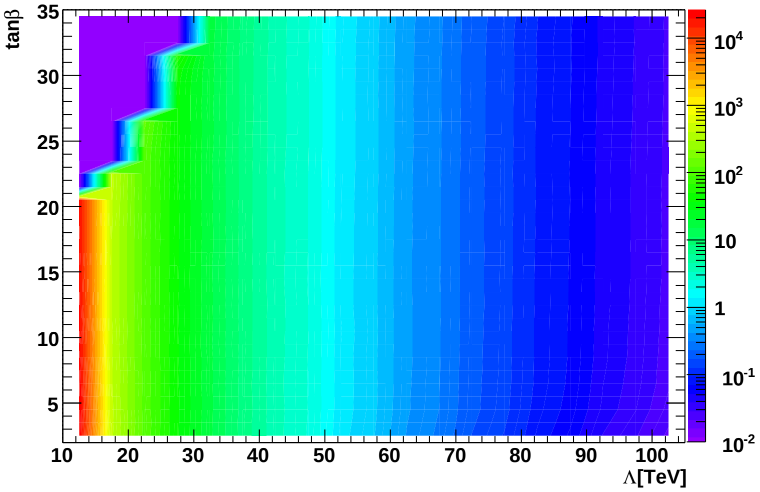

Figure 6.14: The signal cross section (in pb) as a function of Λ and $\tan\beta$.

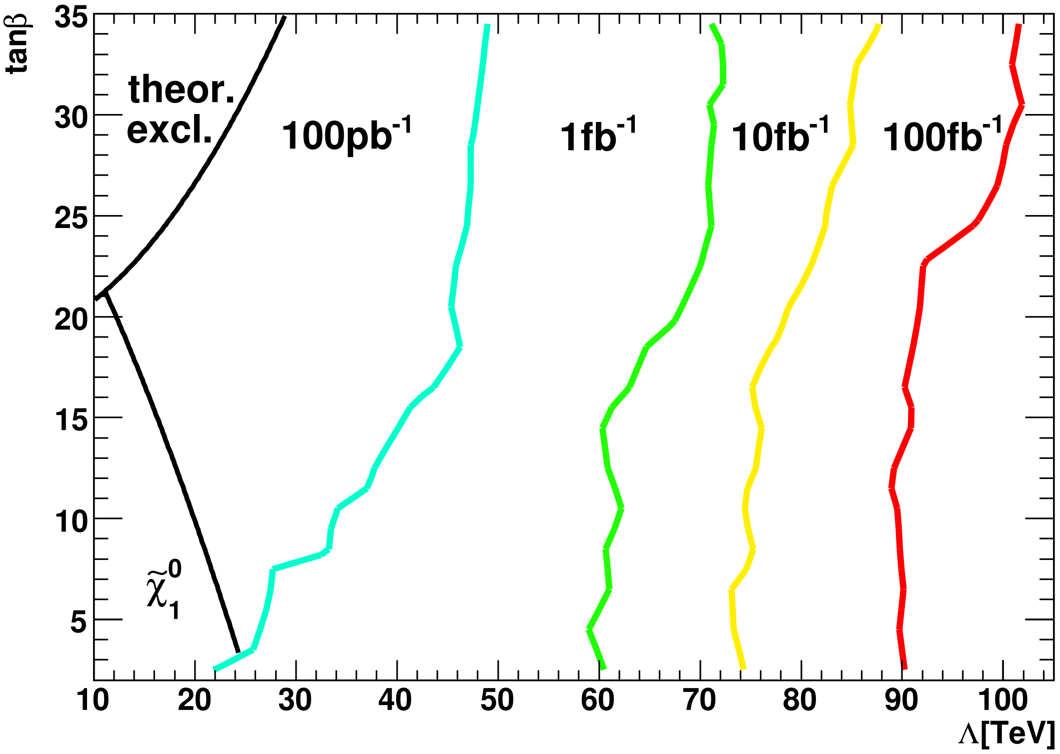

Figure 6.15: The integrated luminosity needed for a 5σ discovery in the Λ-$\tan\beta$ plane.

Chapter 7

Mass Determination of Supersymmetric Particles

Once SUSY is discoverd the identification of the underlying model is the next most important step. The determination of the masses of the supersymmetric particles is vital for this identification since from the mass spectrum conclusions about the breaking mechanism can be drawn. For this purpose SUSY masses can be determined e.g. from the invariant mass distribution of two τ leptons. In this chapter, first the relation between the theoretical endpoint of the invariant mass distribution and the masses of the involved supersymmetric particles is derived. This information is then used to extract the masses from the measured invariant mass distribution of two τ leptons.

7.1 The Invariant Mass Distribution

In a wide range of the GMSB parameter space many decay chains lead to multiple τ lepton final states. The presented study is performed on the benchmark point GMSB6 where the NLSP is the $\widetilde{\tau}_1$. As mentioned above the dominant decay chains are

$$\begin{aligned} \widetilde{\chi}^0{}_{1,2} \quad &\rightarrow \tau_1 \, \widetilde{\tau} \quad &&\rightarrow \tau_1 \, \tau_2 \, \tilde{G} \\ \widetilde{\ell}_R \quad &\rightarrow \ell \, \tau_1 \, \widetilde{\tau} \quad &&\rightarrow \ell \, \tau_1 \, \tau_2 \, \tilde{G}. \end{aligned}$$

The invariant mass distribution of the two τ leptons allows to estimate the masses of the involved supersymmetric particles. Unlike the invariant mass distribution of two τ leptons originating from a Z^0 decay this invariant mass distribution does not offer a resonance at one of the SUSY masses due to the unmeasured gravitino. However, it possesses a typical triangular shape and a defined endpoint determined by the gravitino mass, the $\widetilde{\tau}$ mass and one of the neutralino masses or the slepton mass depending on the decay chain.

For the distribution of τ leptons from the neutralino decay this endpoint can be calculated as follows. Taking into account that in the restframe of the $\widetilde{\tau}$

$$m_{\widetilde{\tau}} = E_{\widetilde{\chi}_1^0} - E_{\tau_1} \qquad \text{and} \qquad \vec{p}_{\widetilde{\chi}_1^0} = \vec{p}_{\tau_1} \tag{7.1}$$

the momentum of $\widetilde{\chi}_1^0$ is given by

$$\begin{aligned} p^2_{\widetilde{\chi}_1^0} &= E^2_{\widetilde{\chi}_1^0} - m^2_{\widetilde{\chi}_1^0} \\ &= (m_{\widetilde{\tau}} + E_{\tau_1})^2 - m^2_{\widetilde{\chi}_1^0} \\ &= (m_{\widetilde{\tau}} + |\vec{p}_{\tau_1}|)^2 - m^2_{\widetilde{\chi}_1^0} \\ &= m^2_{\widetilde{\tau}} + |\vec{p}_{\tau_1}|^2 + 2m_{\widetilde{\tau}}|\vec{p}_{\tau_1}| - m^2_{\widetilde{\chi}_1^0}, \end{aligned} \tag{7.2}$$

while the τ mass is neglected, since it is small compared to all masses involved. The momentum of τ_1 results in

$$\begin{aligned} 2m_{\widetilde{\tau}}|\vec{p}_{\tau_1}| &= m^2_{\widetilde{\chi}_1^0} - m^2_{\widetilde{\tau}} \\ |\vec{p}_{\tau_1}| &= \frac{m^2_{\widetilde{\chi}_1^0} - m^2_{\widetilde{\tau}}}{2m_{\widetilde{\tau}}}. \end{aligned} \tag{7.3}$$

This calculation can be done analogously for the $\widetilde{\tau}$ decay. Considering

$$m_{\widetilde{\tau}} = E_{\tau_2} + E_{\tilde{G}} \qquad \text{and} \qquad \vec{p}_{\tau_2} = -\vec{p}_{\tilde{G}} \tag{7.4}$$

in the restframe of the $\widetilde{\tau}$, the momentum of the gravitino reads by

$$\begin{aligned} p^2_{\tilde{G}} &= E^2_{\tilde{G}} - m^2_{\tilde{G}} \\ &= m^2_{\widetilde{\tau}} + |\vec{p}_{\tau_2}|^2 - 2m_{\widetilde{\tau}}|\vec{p}_{\tau_2}| - m^2_{\tilde{G}}, \end{aligned} \tag{7.5}$$

resulting in the momentum for τ_2

$$|\vec{p}_{\tau_2}| = \frac{m^2_{\widetilde{\tau}} - m^2_{\tilde{G}}}{2m_{\widetilde{\tau}}}. \tag{7.6}$$

These momenta are used for the calculation of the invariant mass

$$\begin{aligned} M^2_{\tau\tau} &= (E_{\tau_1} + E_{\tau_2})^2 - (\vec{p}_{\tau_1} + \vec{p}_{\tau_2})^2 \\ &= 2|\vec{p}_{\tau_1}||\vec{p}_{\tau_2}| - 2\vec{p}_{\tau_1}\vec{p}_{\tau_2} \\ &= 2|\vec{p}_{\tau_1}||\vec{p}_{\tau_2}|(1 - \cos\theta) \end{aligned} \tag{7.7}$$

of the two τ leptons, where θ is the angle between the two τ leptons. The invariant mass distribution is at maximum when $\theta = \pi$

$$M^2_{\tau\tau,\max} = \frac{(m^2_{\widetilde{\chi}_1^0} - m^2_{\widetilde{\tau}})(m^2_{\widetilde{\tau}} - m^2_{\tilde{G}})}{m^2_{\widetilde{\tau}}}. \tag{7.8}$$

Neglecting the gravitino mass $m_{\tilde{G}} = 2.4\,\text{eV}$ the endpoint simplifies to

$$M_{\tau\tau,\max} = \sqrt{m^2_{\widetilde{\chi}_1^0} - m^2_{\widetilde{\tau}}}. \tag{7.9}$$

and gives a value for GMSB6 of 121.6 GeV considering the theoretical values for the neutralino mass $m_{\widetilde{\chi}_1^0} = 158.3\,\text{GeV}$ and the $\widetilde{\tau}$ mass $m_{\widetilde{\tau}} = 101.4\,\text{GeV}$ (cf. Table A.1).

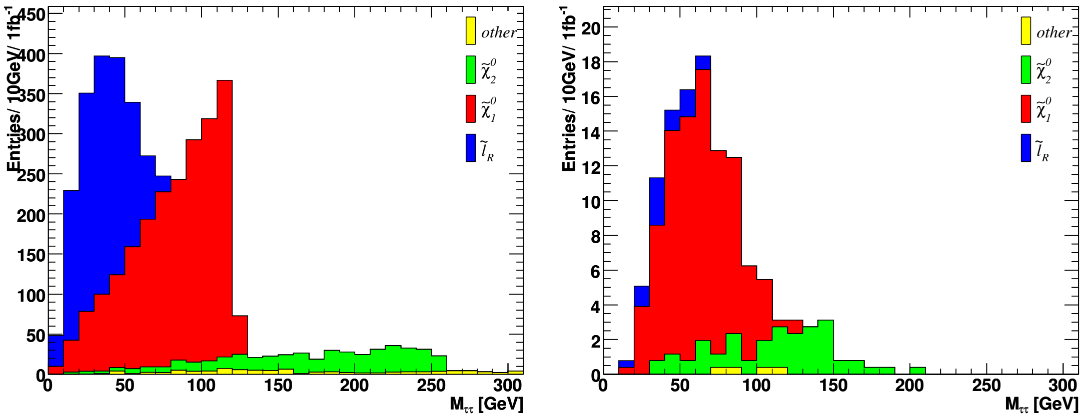

Figure 7.1: The invariant mass distribution of two τ leptons in the same chain based on Monte Carlo information (left) and for reconstructed τ leptons in the selected events (right).

7.2 Fit of the invariant mass distribution

The invariant mass distribution is shown in Fig. 7.1 (left) for τ leptons on generator level and for reconstructed τ leptons (right) in the selected signal events. The selection includes all preselection cuts (Sect. 6.2) and the following requirements (Sect. 6.3)

$$N_\tau \geq 2 \qquad \text{and} \qquad \left(\frac{\not{E}_T}{300\,\text{GeV}}\right)^2 + \left(\frac{p_{T,\text{jet1}}}{600\,\text{GeV}}\right)^2 > 1. \tag{7.10}$$

The invariant mass distribution consists of three contributions: decays of the two lightest neutralinos and decays of either right-handed selectrons or sleptons. The distribution of the τ leptons from the lightest neutralino decays features the typical triangular shape including the edge at the calculated endpoint. The distribution from the second lightest neutralino shows in principal the same shape but the overall portion is smaller since these decays occur only in approximately 10% of all decay chains. The endpoint is at 257.8 GeV due to the higher mass difference and is therefore much more difficult to measure. The distribution from the slepton decays does not feature this triangular shape because the additional lepton is not taken into account smearing out the distribution but still offering the theoretical endpoint of 80.7 GeV.

In the invariant mass distribution of the reconstructed τ leptons shown in Fig. 7.1 (right) the triangular shapes are lost due to the unmeasured neutrinos. Due to the reconstruction inefficiencies explained in Sect. 5.1.3 almost no τ leptons from the slepton decays are reconstructed.

For the determination of the invariant mass endpoint and therefore the estimation of the mass difference of the lightest neutralino and the $\tilde{\tau}$ the invariant mass distribution is fitted with a function, a parameter of which needs to be related to

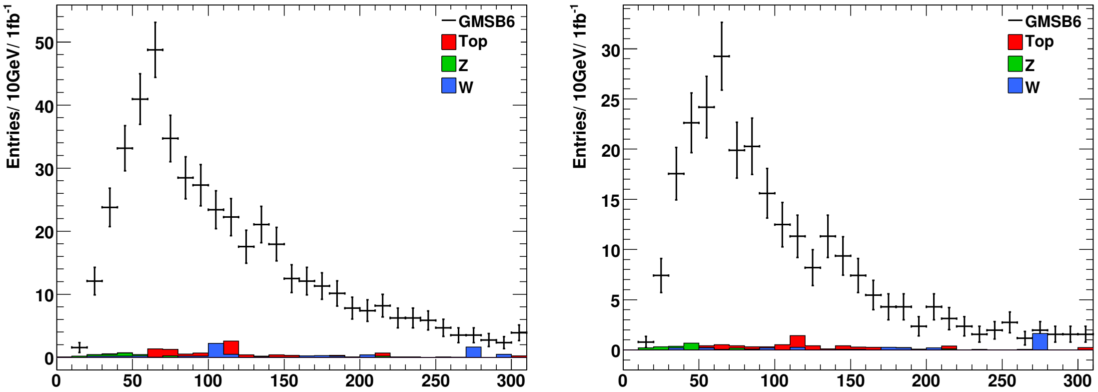

(a) All τ combinations (b) OS

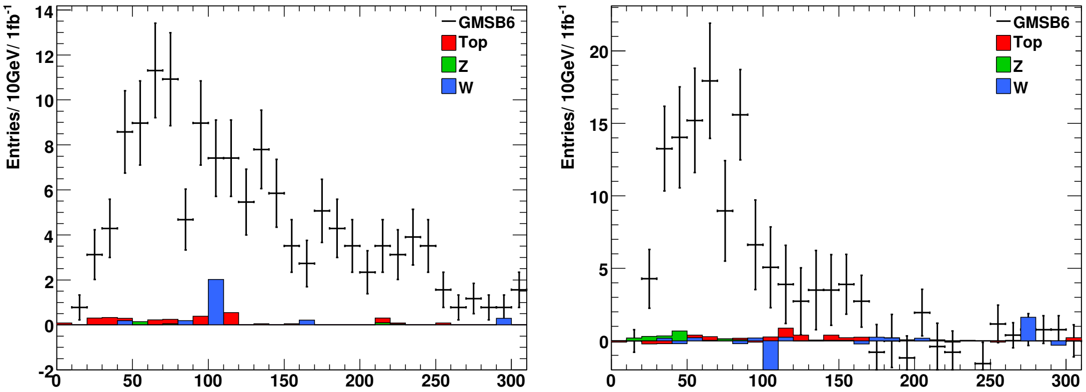

(c) SS (d) OS - SS

Figure 7.2: The invariant mass distribution of (a) any two τ leptons for the signal and the background after the selection, (b) only opposite sign combinations, (c) only same sign combinations and (d) the same sign distribution substracted from the opposite sign distribution.

the endpoint via a calibration using simulated data. Since the tail is the important characteristic of the invariant distribution the inflection point of the fit function is chosen as parameter. Additionally, it offers a strong relation to the true invariant mass. For the fit of the invariant mass distribution a lognormal function

$$f = \frac{p_0}{x} \exp\left(-\frac{1}{2p_2^2}(\log x - p_1)^2\right) \tag{7.11}$$

with three free parameters is used [33] since a simple, linear approach depends strongly on the number of bins and on the fit range. For the determination of the inflection point x_{ip} the second derivative is calculated

$$\frac{d^2 f}{dx^2} = 0 \Rightarrow x_{\text{ip}} = \exp\left(\frac{1}{2}\left(2p_1 - 3p_2^2 + p_2\sqrt{4 + p_2^2}\right)\right) . \tag{7.12}$$

The error of the inflection point is given by

$$\sigma^2_{x_{\mathrm{ip}}} = \sigma^2_{p_1}\left(\frac{\partial x_{\mathrm{ip}}}{\partial p_1}\right)^2 + \sigma^2_{p_2}\left(\frac{\partial x_{\mathrm{ip}}}{\partial p_2}\right)^2 + 2cov(p_1,p_2)\left(\frac{\partial x_{\mathrm{ip}}}{\partial p_1}\right)\left(\frac{\partial x_{\mathrm{ip}}}{\partial p_2}\right), \tag{7.13}$$

$$\frac{\partial x_{\mathrm{ip}}}{\partial p_1} = x_{\mathrm{ip}}, \quad \frac{\partial x_{\mathrm{ip}}}{\partial p_2} = x_{\mathrm{ip}}\left(\frac{2+p_2^2}{\sqrt{4+p_2^2}} - 3p_2\right). \tag{7.14}$$

Since two τ leptons in one event do not necessarily originate from the same decay chain the combination of any two τ leptons can yield wrong combinations. The invariant mass of such two τ leptons has no physical meaning. Since the electric charge of τ leptons from different decay chains is uncorrelated and combinations of two τ leptons having the same charge or the opposite charge occurs with the same frequency, the suppression of wrong combinations is achieved by subtracting the invariant mass distribution of τ leptons having the same charge (same sign - SS) from the distribution of τ leptons having the opposite charge (OS) leaving the τ leptons originating from the same chain.

Figure 7.2 shows the invariant mass of any two τ leptons (upper left) for the signal and the background and the invariant mass of the oppositely charged τ leptons (upper right), of the equally charged leptons (bottom left) and the distribution of OS - SS (bottom right). The first distribution of all combinations offers a long tail containing many wrongly combined τ leptons whereas the OS-SS distribution shows the high peak from the lightest neutralino decays at 60 GeV and a small peak from the second lightest neutralino decays at 150 GeV.

For the determination of the inflection point a fitrange from 0 GeV to 120 GeV is used because for higher values the dominant contribution is due to the second lightest neutralino decay distorting the endpoint of the distribution from the lightest neutralino decay. The fit yielded an inflection point for GMSB6 of $x_{\mathrm{ip}} = 76.1 \pm 4.1$ GeV.

7.3 Determination of the invariant mass endpoint

For the determination of the invariant mass endpoint from the measured inflection point a calibration curve is necessary requiring different signal samples offering different neutralino and $\widetilde{\tau}$ masses. Since such a gauging should be model-independent the calibration from [33] is taken. For the calibration the ATLAS benchmark point SU3 in the mSUGRA parameter space was used. In this scenario the lightest neutralino is the LSP and the $\widetilde{\tau}_1$ is the NLSP as in GMSB6. The studied decay of the second lightest neutralino in SU3

$$\widetilde{\chi}^0_2 \to \widetilde{\tau}_1\tau \ \to \widetilde{\chi}^0_1\tau \ \tau \tag{7.15}$$

is comparable to the decay of the lightest neutralino in GMSB6. ATLFAST I was used for the production of different data samples keeping all the paramaters fixed

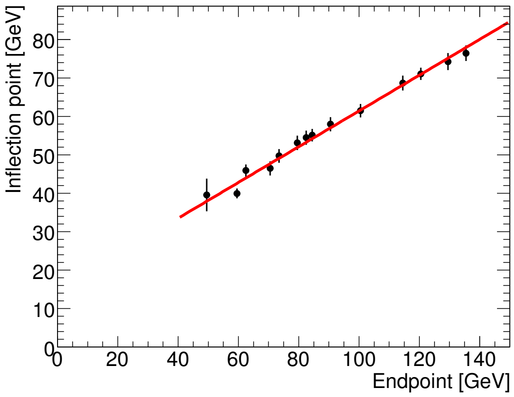

Figure 7.3: The calibration curve for the determinatin of the endpoint [33].

	$10\,\mathrm{fb}^{-1}$	$1\,\mathrm{fb}^{-1}$	$0.5\,\mathrm{fb}^{-1}$	$0.1\,\mathrm{fb}^{-1}$
$\sigma_{x_{\mathrm{ip}}}$ [GeV]	1.3	4.1	5.8	13.0

Table 7.1: The error of the inflection point for different luminosities.

and only varying the mass of one supersymmetric particle. The produced mass differences lead therefore to different measured inflection points and to different corresponding theoretical endpoints. The obtained calibration curve (see Fig. 7.3) corresponds to

$$x_{\mathrm{ip}} = (0.47 \pm 0.02) M_{\tau\tau,\mathrm{max}} + (15 \pm 2)\mathrm{GeV}, \tag{7.16}$$

where the covariance between the slope a and the intercept b of the gauge function is $cov(a, b) = -0.0342$ corresponding to a correlation of $corr(a, b) = -0.855$. For GMSB6 the determined inflection point $x_{\mathrm{ip}} = 76.1 \pm 4.1$ GeV results in an invariant mass endpoint of

$$M_{\tau\tau,\mathrm{max}} = 130.0 \pm 8.7^{\mathrm{stat}}\,{}^{+12.1\mathrm{syst}}_{-12.6}\,\mathrm{GeV}\,. \tag{7.17}$$

The statistical error of the endpoint measurement is determined by the error of the inflection point depending on the amount of data used for the estimation. The presented study was performed on data corresponding to an integrated luminosity of $1\,\mathrm{fb}^{-1}$. Increasing the integrated luminosity to $10\,\mathrm{fb}^{-1}$ reduces the error of the inflection point and therefore the statistical error of the endpoint by a factor of $\sqrt{10}$. For lower integrated luminosities, the error increases accordingly (cf. Table 7.1).

The measurement is influenced by several systematic uncertainties. For instance, the determination of the invariant mass endpoint depends on the calibration procedure. Taking into account the correlation between the slope and the intercept of the gauge function of -0.855 results in $\sigma_{\mathrm{gauging}} = \pm 2.7$ GeV. Increasing the integrated luminosity of the data used for the gauging reduces this error.

In Fig. 7.4 the invariant mass distribution for the signal and all background fitted with the function in Eq. (7.11) for different fit ranges is shown. The different

Fitrange [GeV]	p_1	p_2	infl. point [GeV]	χ^2/ndf
0 - 300	4.242 ± 0.045	0.499 ± 0.033	80.0 ± 3.7	33.5/ 27
0 - 150	4.226 ± 0.055	0.482 ± 0.043	79.3 ± 4.0	9.5/ 12
0 - 135	4.197 ± 0.053	0.461 ± 0.042	77.6 ± 3.8	7.6/ 11
0 - 120	4.173 ± 0.059	0.444 ± 0.045	76.1 ± 4.1	6.7/ 9
0 - 100	4.194 ± 0.090	0.454 ± 0.059	77.5 ± 6.0	5.0/ 7

Table 7.2: The fitted paramters p_1, p_2 including their errors and the corresponding inflection point.

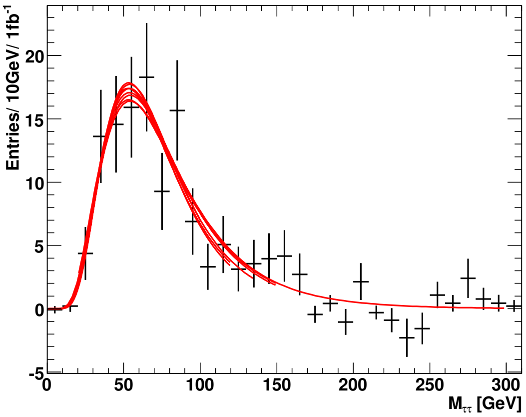

Figure 7.4: The fit of the invariant mass (OS-SS) for different fit ranges.

fit ranges yield different values for the free parameters and therefore different inflection points resulting in different endpoints. The fundamental difference is due to the small peak caused by the second lightest neutralino. Including this range in the fit yields higher inflection points as shown in Table 7.2. Using the various fit ranges yields a contribution to the systematic error of $\sigma_{\text{fitrange}} = \pm 6.8\,\text{GeV}$. Effects due to different binnings cannot be taken into account because reducing as well as increasing the number of bins leads to a loss of the shape and therefore a non-converging fit or intolerable high errors.

The reason for this strong dependence on the fit range are the different contributions to the invariant mass. The selection was optimized for the reduction of the SM background. Including the range containing mostly τ leptons originating from the decay of the second lightest neutralino misaligns the calculated inflection point. To estimate the effect, the fit is also performed on reconstructed τ leptons not including those from the second lightest neutralino (slepton) decays and also doubling their contribution. The resulting differences in the endpoints yield $\sigma_{\tilde{\chi}_2^0} =^{+7.9}_{-8.7}$ GeV and $\sigma_{\tilde{\ell}_\text{R}} = \pm 5.3\,\text{GeV}$ respectively. A sophisticated selection also suppressing τ leptons originating from decays other than the lightest neutralino would reduce this dominant contribution to the systematic error.

To estimate the effect caused by the amount of background the fit was performed with different background scalings. The determined values of the inflection

	no BG	BG	2 BG
x_{ip} [GeV]	76.9 ± 4.3	76.1 ± 4.1	75.4 ± 3.9

Table 7.3: The inflection points for different background scaling.

$M_{\tau\tau,\max}$	σ^{stat}	σ_{gauging}	σ_{fitrange}	$\sigma_{\tilde{\chi}^0_2}$	$\sigma_{\tilde{\ell}_{\text{R}}}$	σ_{BG}
130.0 GeV	±8.7 GeV	±2.7 GeV	±6.8 GeV	$^{+7.9}_{-8.7}$ GeV	±5.3 GeV	$^{+1.7}_{-1.5}$ GeV

Table 7.4: The invariant mass endpoint and its statistical and different systematic errors for the calculated invariant mass endpoint.

point are shown in Table 7.3. No background increases the inflection point whereas the doubled amount of background data reduces the endpoint since two τ leptons of the background yield in general a rather small invariant mass (Fig. 7.2). The resulting error on the endpoint from the background uncertainty is estimated by the difference and yields $\sigma_{\text{BG}} =^{+1.7}_{-1.5}$ GeV.

Table 7.4 lists the invariant mass endpoint, the statistical error, and the systematics resulting in a systematic error for the endpoint of $\sigma^{\text{syst}} =^{+12.1}_{-12.6}$ GeV. The calculated endpoint is compatible with the theoretical value of 121.57 GeV reagarding the uncertainty of approximately 11.8%.

The study has shown the separation of the signal from the background can be done very successfully. The estimation of the invariant mass endpoint can be done with reasonable precision whereas using more data and an explicit selection would be able to determine the edpoint more precisely.

Chapter 8

Conclusion

The LHC is the key machine of searches for physics beyond the SM reaching a new energy frontier far exceeding everything existing today. Supersymmetry is one of the most favored extensions whereas GMSB describes a very important breaking mechanism. In this thesis an estimation of the discovery potential of GMSB models with the ATLAS detector and an investigation of the invariant mass distribution of two τ leptons in the GMSB6 scenario has been presented. The investigation of the τ reconstruction efficiency revealed difficulties in the collaboration wide reconstruction of τ leptons originating from sleptons which cannot be recovered. Despite these problems, the performed selection suppressed the SM background almost completely yielding a large signal significance for the GMSB6 scenario which corresponds to a needed integrated luminosity of about $50\,\mathrm{pb}^{-1}$ for a 5σ discovery.

In a scan of the GMSB parameter space using multi τ final states performed for the first time in this analysis, it has been demonstrated that using the ATLAS detector a 5σ discovery is possible using small data sets for a large part of GMSB scenarios. For a discovery in regions of a large SUSY breaking scale an increased integrated luminosity is needed.

For the invariant mass distribution of two τ leptons slightly different selection cuts were used, to provide a higher signal statistics. Using a calibration obtained through different mSUGRA samples the endpoint of the invariant mass distribution was calculated to $130.0 \pm 8.7^{\mathrm{stat}}\,{}^{+12.1\mathrm{syst}}_{-12.6}$ GeV compatible with the theoretical value of $121.6\,\mathrm{GeV}$.

Appendix A

Additional Tables

A.1 GMSB

	Λ	$\mathrm{M_m}$	$\mathrm{N_5}$	$\tan\beta$	sgnμ	$\mathrm{C_{grav}}$	NLSP
GMSB1	90 TeV	500 TeV	1	5	+1	1.0	$\widetilde{\chi}^0_1$
GMSB2	90 TeV	500 TeV	1	5	+1	30.0	$\widetilde{\chi}^0_1$
GMSB3	90 TeV	500 TeV	1	5	+1	55.0	$\widetilde{\chi}^0_1$
GMSB4	30 TeV	250 TeV	3	5	+1	1.0	$\widetilde{\ell}_R$
GMSB5	30 TeV	250 TeV	3	5	+1	$5 \cdot 10^3$	$\widetilde{\ell}_R$
GMSB6	40 TeV	250 TeV	3	30	+1	1.0	$\widetilde{\tau}_1$
GMSB7	90 TeV	500 TeV	1	5	+1	10^3	$\widetilde{\chi}^0_1$

Table A.1: The ATLAS GMSB benchmark points.

gauginos	$\widetilde{\chi}^0_1$	$\widetilde{\chi}^0_2$	$\widetilde{\chi}^0{}_3$	$\widetilde{\chi}^0{}_4$	$\widetilde{\chi}^\pm{}_1$	$\widetilde{\chi}^\pm{}_2$	$\widetilde{\mathrm{g}}$	$\widetilde{\mathrm{G}}$
mass [GeV]	158.33	277.0	344.6	390.8	277.6	389.8	915.5	$2.4 \cdot 10^{-9}$

squarks	$\widetilde{\mathrm{u}}_\mathrm{L}$	$\widetilde{\mathrm{u}}_\mathrm{R}$	$\widetilde{\mathrm{d}}_\mathrm{L}$	$\widetilde{\mathrm{d}}_\mathrm{R}$	$\widetilde{\mathrm{b}}_1$	$\widetilde{\mathrm{b}}_2$	$\widetilde{\mathrm{t}}_1$	$\widetilde{\mathrm{t}}_2$
mass [GeV]	891.5	860.9	895.4	859.2	833.1	864.3	786.1	877.6

sleptons	$\widetilde{\mathrm{e}}_\mathrm{L}$	$\widetilde{\mathrm{e}}_\mathrm{R}$	$\widetilde{\nu}_e$		$\widetilde{\tau}_1$	$\widetilde{\tau}_2$	$\widetilde{\nu}_\tau$	
mass [GeV]	129.6	266.8	252.3		101.4	272.4	247.4	

Table A.2: The mass spectrum of the ATLAS benchmark point GMSB6.

A.2 Background Samples

Sample	Number	σ[pb]	σ_{eff}[pb]	Events	$\int \mathscr{L}\mathrm{dt}[\mathrm{pb}^{-1}]$
Generator Cuts: $p_{T,jet1} > 80\,\mathrm{GeV}, p_{T,4jets} > 40\,\mathrm{GeV}$					
Multijets					
3 jets	005061	21188	167	4450	26.65
4 jets	005062	53283	7461	4900	0.66
5 jets	005063	9904	1876	5000	2.67
6 jets	005064	6437	5510	4850	0.88
Generator Cuts: $p_{T,jet1} > 80\,\mathrm{GeV}, p_{T,4jets} > 40\,\mathrm{GeV}, \not{E}_T > 80\,\mathrm{GeV}$					
$\mathrm{t\bar{t}} \to \ell\nu\ell\nu$					
+ 0 jets	005535	49.4	0.185	4000	21622
+ 1 jet	005536	32.0	1.162	22650	19492
+ 2 jets	005537	13.1	1.454	28500	19601
+ 3 jets	005538	4.2	1.34	16250	12127
$\mathrm{t\bar{t}} \to \ell\nu qq$					
+ 0 jets	005530	197.5	3.753	17600	4890
+ 1 jet	005531	128.0	8.346	37958	4548
+ 2 jets	005532	52.4	5.659	23000	4064
+ 3 jets	005533	16.9	3.921	13050	3328
$\mathrm{t\bar{t}} \to qqqq$					
+ 1 jet	005541	128	0.157	4000	25403
+ 2 jets	005542	52.4	0.107	2400	22328
+ 3 jets	005543	16.9	0.077	1500	19410
$\mathrm{b\bar{b}}$					
+ 2 jets	008082	9490	6.681	4000	599
+ 3 jets	008083	1940	3.726	2000	537
$\mathrm{W} \to \mathrm{e}\nu_{\mathrm{e}}$					
+ 2 jets	005223	504	0.67	750	1119
+ 3 jets	005224	122	3.39	15750	4646
+ 4 jets	005225	28.4	2.02	9900	4901
+ 5 jets	005226	6.1	0.87	2950	3391
$\mathrm{W} \to \mu\nu_{\mu}$					
+ 3 jets	008203	122	0.695	2000	2878
+ 4 jets	008204	28.4	1.852	1000	540
+ 5 jets	008205	6.1	0.860	4000	4651
$\mathrm{W} \to \tau\nu_{\tau}$					
+ 2 jets	008208	504	0.534	2750	5150
+ 3 jets	008209	122	2.843	1750	616
+ 4 jets	008210	28.4	2.675	14000	5234
+ 5 jets	008211	6.1	1.201	4700	3913
$\mathrm{Z} \to \nu\nu$					

Sample	Number	σ[pb]	σ_{eff}[pb]	Events	$\int \mathscr{L}\mathrm{dt}[\mathrm{pb}^{-1}]$
+ 3 jets	005124	79.8	0.88	11500	13068
+ 4 jets	005125	18.5	2.4	44000	18333
+ 5 jets	005126	3.96	1.07	11500	10748
Z → $\tau\tau$					
+ 2 jets	008114	56.4	0.169	3750	22189
+ 3 jets	008115	14.1	0.324	7000	21605
+ 4 jets	008116	3.26	0.163	4000	24540
+ 5 jets	008117	0.70	0.070	1000	14286
Generator Cuts: $p_{T,jet1} > 80\,\mathrm{GeV}, p_{T,4jets} > 40\,\mathrm{GeV}, p_{T,Z} > 80\,\mathrm{GeV}$					
Z → ee					
+ 1 jet	005161	179.8	0.316	1500	4750
+ 2 jets	005162	56.4	3.266	6000	1837
+ 3 jets	005163	14.1	2.172	21850	10058
+ 4 jets	005164	3.26	0.547	6000	10972
+ 5 jets	005165	0.7	0.139	2000	14430
Z → $\mu\mu$					
+ 3 jets	008109	14.1	0.189	2000	10564
+ 4 jets	008110	3.26	0.415	3420	8309
+ 5 jets	008111	0.7	0.133	1750	13090

Table A.3: The table lists all background samples used for the analysis. The cross section and the effective cross section which takes into account the generator cuts are also listed as well as the number of available events and the corresponding integrated luminosity.

Bibliography

[1] S.L. Glashow. Nucl. Phys. **22** (1961) 579, S. Weinberg, Phys. Rev. Lett. **19** (1967) 1264, A. Salam, in Elementary Particle Theory, ed. N. Svartholm, Stockholm, “Almquist and Wiksell” (1968), 367.

[2] H. Fritzsch, M. Gell-Mann, and H. Leutwyler. *Phys. Lett.*, B47:365–368, 1973.

[3] N. Cabibbo. *Phys. Rev. Lett.*, 10:531, 1963.

[4] M. Kobayashi and T. Maskawa. *Prog. Theor. Phys.*, 49:652, 1973.

[5] S. Weinberg. *Phys. Rev. Lett.*, 19, 1967.

[6] Z. Maki, M. Nakagawa, and S. Sakata. *Prog. Theor. Phys.*, 28:870, 1962.

[7] B. M. Pontecorvo. *Zh. Eksp. Teor. Fiz.*, 53:1717, 1967 [Sov. Phys. JETP, 26 (1968), 984].

[8] P. W. Higgs. *Phys. Lett.*, 12:132, 1964.

[9] The LEP Electroweak Working Group. The LEP Electroweak Working Group (LEP EWWG) combines the measurements of the four LEP Experiments ALEPH, DELPHI, L3 and OPAL. *http://lepewwg.web.cern.ch/LEPEWWG/*, 13.10.2008.

[10] R. Barate et al. *Phys. Lett.*, B565:61, 2003.

[11] E. W. Kolb and M. S. Turner. The early universe. *Westview Press*, 1990.

[12] http://nobelprize.org/nobelprizes/physics/laureates/2004/public.html, 06.10.2008.

[13] S. P. Martin. A Supersymmetry Primer. *hep-ph/9709356*, 2006.

[14] M. Dine, W. Fischler, and M. Srednicki. Nucl. Phys. B189, 575 (1981); S. Dimopoulos and S. Raby, Nucl. Phys. B192, 353 (1981); C. Nappi and B. Ovrut, Phys. Lett.113B, 175 (1982); L. Alvarez-Gaumé, M. Claudson and M. Wise, Nucl. Phys. B207, 96 (1982); M. Dine and A. Nelson, Phys. Rev. D48, 1227 (1993); M. Dine, A. Nelson and Y. Shirman, Phys. Rev. D51, 1362 (1995); M. Dine and others, Phys. Rev. D53, 2658 (1996).

[15] G.F. Giudice and R. Rattazzi. CERN-TH-97-380, hep-ph/9801271 (1998); C Kolda, Nucl. Phys. P. Suppl. 62, 266 (1998).

[16] O. S. Brüning et al. *LHC Design Report V1.* CERN, Geneva, 2004.

[17] M. Benedikt et al. *LHC Design Report V3.* CERN, Geneva, 2004.

[18] The ATLAS Collaboration, G. Aad, et al. The ATLAS Experiment at the CERN Large Hadron Collider. *JINST 3 S08003*, 2008.

[19] The CMS Collaboration, S. Chatrchyan, et al. The CMS Experiment at the CERN Large Hadron Collider. *JINST 3 S08004*, 2008.

[20] http://atlas.ch/photos/full-detector.html, 28.02.2008.

[21] ATLAS Inner Detector Community. ATLAS Inner Detector, Technical Design Report, Volume I. *ATLAS TDR 4, CERN/LHCC 97-16*, 1997.

[22] ATLAS Collaboration. ATLAS Calorimeter Performance, Technical Design Report. *CERN/LHCC 97-40*, 1997.

[23] ATLAS Level-1 Trigger Group. Level-1 Trigger, Technical Design Report. *ATLAS TDR 12*, 1998.

[24] ATLAS HLT/DAQ/DCS Group. ATLAS High-Level Triggers, DAQ and DCS, Technical Proposal. *CERN/LHCC 2000-17*, 2000.

[25] C. Arnault et al. *The ATLAS Computing Workbook*, 2007.

[26] H. Baer, F. E. Paige, S. D. Protopopescu, and X. Tata. *ISAJET 7.71, A Monte Carlo Event Generator for pp, $p\bar{p}$ and e^+e^- Reactions.*

[27] G. Corcella, I. G. Knowles, G. Marchesini, S. Moretti, P. Richardson, M. H. Seymour, and B. R. Webber. HERWIG 6.5: an event generator for Hadron Emission Reactions With Interfering Gluons (including supersymmetric particles). *arXiv:hep-ph/0011363v3*, 2002.

[28] M. L. Mangano, M. Moretti, F. Piccinini, R. Pittau, and A. D. Polosa. ALPGEN, a generator for hard multiparton processes in hadronic collisions. *arXiv:hep-ph/0206293v2*, 2003.

[29] S. Agostinelli et al. GEANT4 - a simulation toolkit. *Nuclear Instruments and Methods in Physics Research Section A: Accelerators, Spectrometers, Detectors and Associated Equipment*, 2003.

[30] The ATLAS Validation Task Force. Performance of the ATLAS Fast Simulation ATLFAST. *ATL-PHYS-INT-2007-005*, 2007.

[31] C. Amsler et al. (Particle Data Group). *Physics Letters B667, 1*, 2008.

[32] P. Bechtle et al. Identification of hadronic tau decays with the atlas detector. *ATL-COM-PHYS-2007-066, revised version*, 2008.

[33] K. Desch, T. Nattermann, P. Wienemann, and C. Zendler. Measuring the endpoint of the di-tau mass spectrum in Neutralino decays with the ATLAS detector at the LHC. *ATL-PHYS-INT-2008-08, ATL-COM-PHYS-2008-038*, 2008.

Selbstständigkeitserklärung

Hiermit versichere ich, Dörthe Ludwig (Studentin der Universität Hamburg, Matrikelnummer 5621155), dass ich die vorliegende Diplomarbeit selbstständig verfasst und außer den angegebenen keiner weiteren Hilfsmittel verwendet habe. Die Arbeit wurde bisher weder in dieser noch in ähnlicher Form einer Prüfungskomission vorgelegt. Einer Veröffentlichung der Arbeit stimme ich zu.

....
Hamburg, den Dörthe Ludwig

Danksagung

Ich möchte die Gelegenheit nutzen und an dieser Stellen allen danken, die mir bei der Entstehung dieser Arbeit geholfen haben, die mich unterstützt, konstruktiv kritisiert und motiviert haben. Danken möchte ich besonders

Prof. Dr. Johannes Haller für die Konzeption und Betreuung meiner Diplomarbeit. Ich möchten mich für seine konstruktiven und unermüdlichen Verbesserungsvorschläge bedanken und für den Anspruch, sich nur mit dem Besten zufrieden zu geben.

Prof. Dr. Peter Schleper für seine Bereitschaft, meine Diplomarbeit als Zweitgutachter zu beurteilen.

Dr. Wolfgang Ehrenfeld für seine Zeit, seine technische Hilfe und für die zahlreichen Denkanstöße und Ideen, um meine Studie voranzutreiben.

Dr. Philip Bechtle wegen der vielen Möglichkeiten, die er mir geboten hat, meine Arbeit zu präsentieren.

Mark Terwort, Karsten Köneke und Martin Goebel für die Unterstützung, bei der Beantwortung vieler physikalischer und technischer Fragen.

Sylvie Brunet: Je voudrais me remercier pour l'aide concernant le "TAUDPD-Maker".

Meine Eltern, weil sie immer an mich geglaubt haben, mich in jeder erdenklichen Weise unterstützt haben und dafür, dass sie mir häufig mehr zugetraut haben als ich mir selbst.

Michael, der immer Geduld für uns beide zusammen haben musste. Ich möchte ihm danken für seine Unterstützung, Loyalität und seinen Humor. Ich schätze ihn als Arbeitskollegen, Freund und Partner.

Allen, die ich vergessen habe.

Vielen Dank!